

MATERIALS CHEMISTRY

Lehrstuhl für Werkstoffchemie
Rheinisch-Westfälische Technische Hochschule Aachen

Prof. Jochen M. Schneider, Ph. D.

Pascal Bliem

Synthesis and Characterization of Re-B Thin Films

Supervisors:

Prof. Jochen M. Schneider, Ph. D.
Dr. Stanislav Mráz

Abstract

In this work, Re-B and Al/Ti-alloyed Re-B thin films are deposited by hybrid RF-DC magnetron sputtering. The phase formation, chemical composition and state, and mechanical properties of the films are characterized by XRD and SEM, EDX and XPS, and nanoindentation, respectively. Phase-pure ReB_2 films are synthesized between 500 and 900°C over a wide composition range of about 55 to 75 at.% B. Al and Ti can be alloyed into ReB_2 films without formation of other phases up to concentrations of 13.6 at.% Al and 3.9 at.% Ti, respectively, which agrees excellently with predictions from the energies of formation obtained by DFT calculations. Unalloyed ReB_2 films exhibit an elastic modulus of about 500 GPa and a hardness of about 30 GPa. These comparably low values (cf. $E_{\text{DFT}}=667$ GPa) can be rationalized by the rough, inhomogeneous, and apparently porous microstructure of the films. Upon Al-alloying, the films become rougher, more porous, and less stiff and hard. However, one exceptionally smooth and dense Al-alloyed film (3.5 at.% Al) exhibits high stiffness and superhardness ($E=562$ GPa, $H=40$ GPa). Upon Ti-alloying, the films show much lower surface roughness and no indication of porosity, which yields high stiffness and superhardness with E and H up to 519 and 40 GPa (12.7 at.% Ti), respectively. Unalloyed ReB_2 films form perrhenic acid (HReO_4) in air, indicating coating corrosion. Ti-alloyed films form TiO_2 which slows down the corrosive reaction, but does not seem to result in full passivation. Al-alloying, on the contrary, results in the formation of a passivating Al_2O_3 layer which prevents a corrosive reaction already at an Al concentration of 3.7 at.%. Thus, it is shown that superhard and chemically stable $(\text{Re},\text{Al})\text{B}_2$ coatings can be synthesized by magnetron sputtering.

Zusammenfassung

In dieser Studie werden Re-B und Al/Ti-legierte Re-B Dünnschichten mittels Hybrid-RF-DC-Magnetronkathodenzerstäubung abgeschieden. Phasenbildung, chemische Zusammensetzung und chemischer Zustand, und mechanische Eigenschaften werden entsprechend durch XRD und REM, EDX und XPS, sowie Nanoindentation charakterisiert. Phasenreine ReB_2 Schichten werden zwischen 500 und 900°C über eine weite Zusammensetzungsspanne von 55 bis 75 at.% B synthetisiert. Al und Ti können bis zu Konzentrationen von jeweils 13.6 at.% Al und 3.9 at.% Ti in ReB_2 Schichten legiert werden, ohne dass sich andere Phasen bilden, was hervorragend mit Vorhersagen durch DFT-berechnete Bildungsenergien übereinstimmt. Unlegierte ReB_2 Schichten weisen einen E-Modul von ca. 500 GPa und eine Härte von ca. 30 GPa auf. Diese verhältnismäßig geringen Werte (vgl. $E_{\text{DFT}}=667$ GPa) können durch die rau, inhomogene und anscheinend poröse Mikrostruktur der Schichten erklärt werden. Durch Al-legieren werden die Schichten rauer, poröser und weniger steif und hart. Allerdings weist eine außergewöhnlich ebene und dichte Schicht eine hohe Steifigkeit und Härte auf ($E=562$ GPa, $H=40$ GPa). Durch Ti-legieren zeigen die Schichten eine wesentlich geringere Oberflächenrauheit und keine Anzeichen von Porosität, was in hoher Steifigkeit und Superhärte mit E und H bis zu jeweils 519 und 40 GPa (12.7 at.% Ti) resultiert. Unlegierte ReB_2 Schichten bilden an Luft Perrheniumsäure (HReO_4), was ein Anzeichen für Korrosion der Schicht ist. Ti-legierte Schichten bilden TiO_2 wodurch die Korrosionsreaktion verlangsamt, aber nicht endgültig gestoppt wird. Al-legierte Schichten hingegen bilden bereits bei einer Al Konzentration von 3.7 at.% eine passivierende Al_2O_3 Schicht, die die Korrosionsreaktion verhindert. Dadurch wird gezeigt, dass superharte und chemisch stabile $(\text{Re},\text{Al})\text{B}_2$ Beschichtungen durch Magnetronkathodenzerstäubung hergestellt werden können.

“The story so far: In the beginning the Universe was created. This has made a lot of people very angry and been widely regarded as a bad move.”

— Douglas Adams, The Restaurant at the End of the Universe

Contents

Abstract	i
Zusammenfassung	ii
1 Introduction and review	1
1.1 The Re-B material system	1
1.2 Re-B thin film synthesis	6
2 Methodology	10
2.1 Computational details	10
2.2 Experimental details	11
3 Results and discussion	14
3.1 Energy of formation of Re-B and Re-B-C/Al/Ti systems	14
3.2 Phase formation of Re-B and Al/Ti-alloyed Re-B films	16
3.3 Mechanical properties and microstructure	22
3.4 Chemical stability of Re-B and Al/Ti-alloyed Re-B films	30
4 Conclusions	36
5 Outlook	37
6 Acknowledgments	38
7 Declaration of originality	39
8 References	40
A Appendix	44
A.1 DFT computational cells	44
A.2 Phase formation raw data	47
A.3 XRD stress measurement raw data	56

1. Introduction and review

The demand for new hardcoating material systems with precisely tailored properties increases continuously as the range of highly specialized industrial machining applications is broadened. ReB_2 was suggested as a potential candidate for wear-resistant coatings about a decade ago [1], owing to its supposed superhardness ($H \geq 40 \text{ GPa}$), for applications in which conventional superhard materials cannot be used due to their chemical reactivity (e.g. carbide formation during machining of ferrous alloys with diamond-like coatings) or lack of electrical conductivity (e.g. c-BN, c- BC_2N , B_6O). In the following, the Re-B material system and previous attempts to synthesize ReB_2 coatings will be reviewed.

1.1 The Re-B material system

The Re-B material system exhibits three thermodynamically stable phases, ReB_2 , Re_7B_3 , and Re_3B , all with peritectic melting temperatures of at least 2000°C [2] (Figure 1.1). A metastable Re_4B_4 phase has been reported as well [3]. The unit cells of all phases are depicted in Figure 1.2. While Re_7B_3 and Re_3B are primarily known for their superconducting behavior [4], ReB_2 sparked large

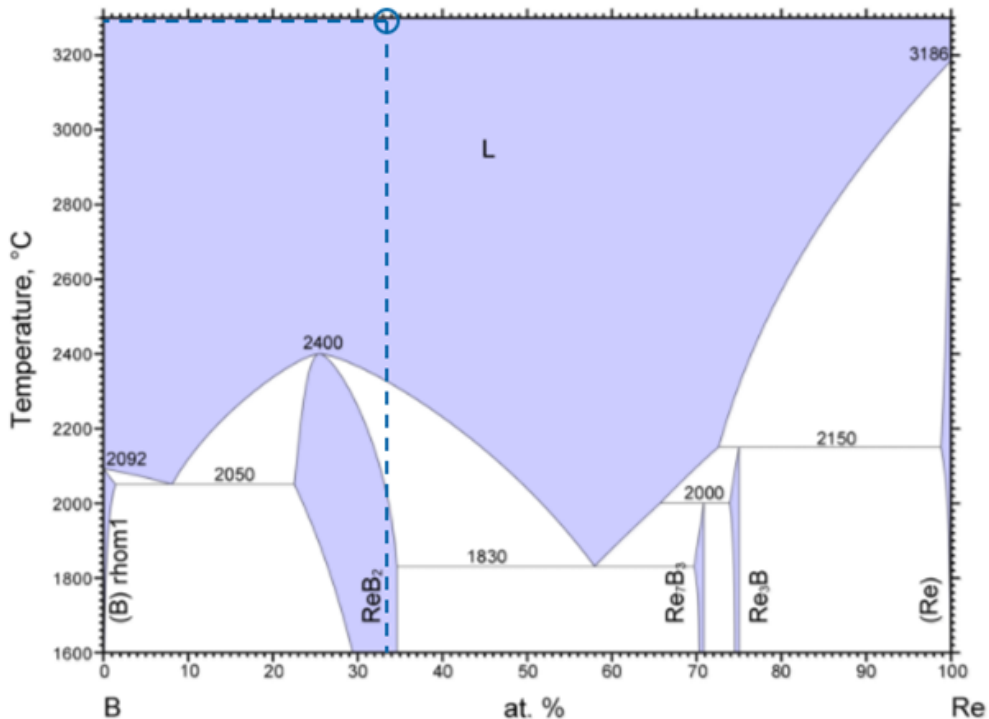


Figure 1.1: Phase diagram of the Re-B material system after data from Portnoi et al. [2].

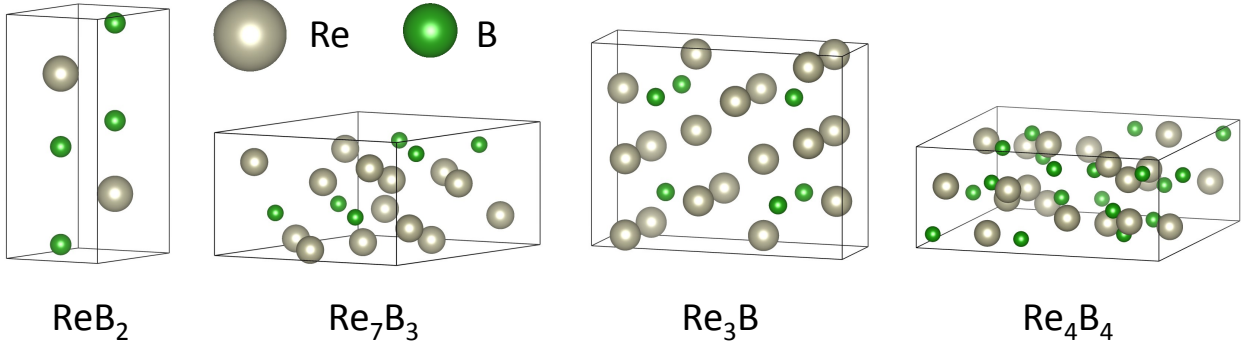


Figure 1.2: Unit cells of ReB_2 , Re_7B_3 , Re_3B , and Re_4B_4 , the phases of the Re-B material system.

interest as a potentially superhard (hardness over 40 GPa), ultra-incompressible ($-6.97 \times 10^{-4} \text{ GPa}^{-1}$ [1]), and yet electrically conductive ($\sigma=24.57 \text{ S/cm}$ [5]) material. ReB_2 was first synthesized in 1962 by La Placa et al. [6], who reported ReB_2 crystallized in a hexagonal lattice ($a=2.900 \text{ \AA}$, $c=7.478 \text{ \AA}$) with alternating Re and B layers, similar to the AlB_2 structure, except that the B layers in ReB_2 are puckered and not flat. Furthermore, short B-B bonds (1.82 Å) and Re-B bonds (2.23 and 2.26 Å) were reported. Since then, many experimental and computational studies investigated the structure of ReB_2 . Average values of the lattice parameters and several other properties are given in Table 1.1. Electronic structure calculations of the ReB_2 phase by density functional theory (DFT) [19–27, 29, 34, 35] reveal not only short, but also highly directional covalent, hence strong, B-B and Re-B bonds. Re-Re bonds, on the contrary, are predominantly metallic. Corresponding to Re-B bonds, the density of states (DOS) exhibits a strong hybridization of the Re-d and B-p orbitals [16, 17, 21, 29] with a pseudo-gap around the Fermi level. The pseudo-gap suggests that mostly bonding states of the hybridization complex are occupied while higher lying anti-bonding states stay unoccupied, which further contributes to bond strength [17, 21, 29].

Electronic structure calculations consistently predict extraordinarily high elastic constants (Table 1.1), with $C_{33}=1076(28) \text{ GPa}$ (notation: average value (standard deviation on the last significant digits)) of ReB_2 even exceeding $C_{11}=950 \text{ GPa}$ of diamond [36]. Resulting macroscopic elastic quantities (Table 1.1), such as bulk, elastic, and shear moduli are correspondingly high as well. Especially, a high shear modulus ($G=295(7) \text{ GPa}$, computed for ReB_2) is often seen as an indicator for high hardness [15, 26, 29, 35]. Some studies attempted to assess theoretical hardness computationally, e.g. by bond energy density methods ($H=46.0 \text{ GPa}$ [16], 43.6 GPa [34]), an

Property	Experimental average	Computational average	Ref. Exp.	Ref. Comp.
a (Å)	2.900(2)	2.89(2)	[5–14]	[15–27]
c (Å)	7.478(7)	7.44(4)	[5–14]	[15–27]
C_{11} (GPa)	599(89)	673(23)	[28]	[15–19, 21, 22, 26, 29]
C_{33} (GPa)	1023	1076(28)	[28]	[15–19, 21, 22, 26, 29]
C_{44} (GPa)	239(40)	276(10)	[28]	[15–19, 21, 22, 26, 29]
C_{12} (GPa)	140(37)	157(14)	[28]	[15–19, 21, 22, 26]
C_{13} (GPa)	185	134(12)	[28]	[15–19, 21, 22, 26]
B (GPa)	316(63)	355(9)	[1, 10, 12, 13, 28, 30, 31]	[15–23, 25, 26]
B'	4	4.2(1)	[8, 12, 13]	[17, 19, 20, 22, 23]
E (GPa)	561(102)	698(13)	[5, 10, 14, 28, 30]	[15, 17, 21, 22, 26]
G (GPa)	231(43)	295(7)	[10, 28, 30, 32]	[15, 17, 19, 21, 22, 25, 26, 29]
ν	0.16(4)	0.178(6)	[10, 28, 30]	[15, 17, 21, 22, 26]
H_{max} (GPa) *	38(11)	44(4)	[1, 5, 9, 14, 28, 30, 33]	[16, 21, 26, 29, 34, 35]
ρ (g/cm ³)	11.7(7)	12.96(9)	[6, 28, 30, 32]	[15, 21, 23]
Θ_D (K)	736(2)	806(56)	[10, 28]	[15, 20, 21]
α_L (x10 ⁻⁶ K ⁻¹) **	6(1)	2.8(5)	[8, 13, 31]	[16, 20]
c_p (J/(molK))	–	56.26	[20]	
σ (S/cm)	24.57	–	[5]	

Table 1.1: An overview of experimental and computational average values of various physical properties of ReB₂. Rows show lattice parameters, a and c , elastic constants, C_{11} , C_{33} , C_{44} , C_{12} , C_{13} , bulk modulus and its pressure derivative, B and B' , elastic modulus, E , shear modulus, G , Poission's ratio, ν , maximum hardness, H_{max} , density, ρ , Debye temperature, Θ_D , linear thermal expansion coefficient, α_L , isobaric heat capacity, c_p , and electrical conductivity, σ .

*Here, only the max. hardness values were considered; load-dependence is discussed in the text.

**Only isotropic expansion at approximately room temperature is considered.

empirical correlation of shear modulus and hardness ($H=47.5$ GPa [29], 40.4 GPa [26]), a correlation of Debye temperature and hardenss ($H=35.9$ GPa [21]), or minimum critical stress for brittle cleavage ($H=43.8$ GPa [35]). The majority of these studies suggests that ReB_2 is superhard when hardness is determined by bond breaking.

Experimental studies show larger scattering in the reported elastic properties and hardness. Chung et al. [1] first characterized mechanical properties of ReB_2 and reported a bulk modulus of 360 GPa, incompressibility along the c -axis that rivals diamond, and even the ability to scratch diamond [37]. The authors also reported superhardness ($H=48.0$ GPa) via micro-Vickers-indentation at a load of 0.5 N, decreasing to $H=30.1$ GPa at a load of 5 N. Dubrovinskaia et al. [38] commented that such an indentation size effect (decreasing H with increasing indentation load) is common for hard materials and the asymptotic hardness, 30.1 GPa, should be reported; therefore, ReB_2 could not be considered as superhard ($H \geq 40$ GPa). Qin et al. [30] reported comparably low values for elastic quantities ($B=173$ GPa, $E=382$ GPa, $G=169$ GPa) and micro-Vickers hardness (from $H=18.8$ GPa at 2.9 N to $H=16.9$ GPa at 49 N). Tkachev et al. [32] argued that these low values might stem not only from 5% porosity in Qin et al.'s samples, but also from 10 vol.% amorphous excess B introduced by the non-stoichiometric Re:B 1:2.5 composition of powders which were used for sintering by Qin et al. Tkachev et al. [32] synthesized not fully dense ReB_2 compacts with Re_7B_3 impurities by spark plasma sintering and measured a higher shear modulus of 223 GPa. Koehler et al. [10], who also synthesized samples starting from a powder composition of Re:B 1:2.5, measured higher values of the elastic properties ($B=317$ GPa, $E=642$ GPa, $G=276$ GPa) than Qin et al. [30]. They argued that the excess B evaporated during arc melting and the final composition of their samples is Re:B 1:2, based on the samples' density. Levine et al. [28] compared underdense spark plasma sintered samples with 10 at.% excess B to dense and stoichiometric samples grown in a tri-arc crystal grow furnace. The latter ones' mechanical properties ($H=39.5$ GPa at 0.46 N, $B=383$ GPa, $E=661$ GPa, $G=273$ GPa) were clearly superior to those of the former ones ($H=27.0$ GPa at 0.36 N, $B=230$ GPa, $E=434$ GPa, $G=183$ GPa). In another study, Levine et al. [5] grew single-crystals of ReB_2 by an aluminum flux method and characterized them with micro-Vickers-indentation (from $H=40.5$ GPa at 0.49 N to $H=28.3$ GPa at 4.89 N on (001) plane,

from $H=38.1$ GPa at 0.49 N to $H=27.9$ GPa at 4.89 N on (hk0) plane) and by nanoindentation ($H=36.4$ GPa and $E=675$ GPa at 392 mN on (001) plane, $H=34.0$ GPa and $E=510$ GPa at 424 mN on (hk0) plane). The authors suggested that B vacancies in their samples may degrade the mechanical properties. Otani et al. [33] also produced ReB_2 single-crystals by a floating zone method and reported micro-Vickers hardness from 30.8 GPa at 0.98 N to 29.8 GPa at 1.96 N on the (001) plane and 35.8 GPa at 1.96 N on the (100) plane.

The differences in mechanical properties reported in experimental literature seem to be correlated to sample features such as density, chemical composition, phase impurities, and poly- or single-crystallinity and crystallographic orientation. Pan et al. [26] showed in a computational study that B vacancies reduce elastic properties and theoretical hardness and it can be assumed that Re vacancies would have a similar effect. Re_7B_3 phase impurities were often reported in ReB_2 samples [13, 28, 32, 39, 40]. Levine et al. [28] described that the formation of Re_7B_3 can be prevented by adding excess B to the initial powder composition. This is probably part of the reason why B was also added in other studies [8–10, 12–14, 30, 32, 40], potentially resulting in an amorphous B impurity phase. The reduction of hardness with increasing load, also known as indentation size effect, is often attributed to strain gradient plasticity [1, 41] or effects other than plastic deformation such as brittle cracking or deformation of the indenter tip [38]. As an additional explanation, Zhang et al. [27] proposed in a computational study that a shear-induced transformation into a less mechanically strong meta-stable structure limits the hardness of ReB_2 .

Besides mechanical properties possibly not achieving theoretical values, chemical stability might be a handicap in utilization of ReB_2 . Otani et al. [33] and Orlovskaia et al. [42] both reported formation of a liquid on their samples. Based on thermodynamical data, Orlovskaia et al. hypothesized that Re_2O_7 and B_2O_3 oxides react with water from air to form perrhenic acid (HReO_4) and boric acid (H_3BO_3), respectively. These hygroscopic acids might adsorb more water from air and, thereby, further degrade the bulk material. Alloying is a method which may be utilized to overcome this obstacle; if one was able to alloy ReB_2 with small amounts of an element which forms a passivating oxide layer, without heavily downgrading the supreme mechanical properties. These desired properties, as reviewed above, are derived from the strong B-B and

metal-B bonds inherent to the ReB_2 structure; therefore, alloying elements which can substitute Re in a solid solution is desirable. Al and Ti are known for their oxygen affinity, stable oxides, and they also form hexagonal (though not isostructural to ReB_2) diborides and may, hence, be interesting candidates as alloying elements.

1.2 Re-B thin film synthesis

While computational studies based on electronic structure calculations mostly predict highly promising (ground state) properties for hard materials applications, experimental results are not fully conclusive and suggest that chemical and microstructural features of a specimen or workpiece have a large influence on its suitability for potential applications. Despite several of the works reviewed above suggesting ReB_2 may be promising as a protective or wear resistant coating, e.g. on cutting tools, little work has been carried out in this field. Ivanov et al. [43] deposited nanostructured ReB_2 coatings by resonant infrared decomposition of molecular precursors on various substrates such as Kevlar, Teflon or ultralene polymer films. ReB_2 thin films were only synthesized by pulsed laser deposition (PLD) by Latini et al. [9] and Chrzanowska et al. [14], so far. Both studies reported very high values of hardness ($H=52$ GPa and up to 60 GPa, respectively); however, the accuracy of these results is questionable. Latini et al. indented a 300 nm thick film and the underlying fused silica substrate, which adhered poorly to each other, with a micro-Vickers indenter at loads up to 2000 mN. The authors then attempted to deconvolute the film and substrate contributions by an indentation area law-of-mixtures approach. Chrzanowska et al. used more suitable nanoindentation, but chose an inapplicable indentation depth of ca. 70 nm on a 170 nm thick film (far more than 10% of the film thickness), which most probably contains a substrate contribution [44].

In previous work within this group, Hunold (unpublished) employed pulsed (100 kHz) direct current (DC) magnetron sputtering for depositions of combinatorial Re-B thin films on sapphire (0001) substrates at 900°C. The setup consisted of one Re target and two B targets. Even though some areas on the combinatorial samples exhibited close to the Re:B 1:2 composition, according to standard-less energy dispersive x-ray spectroscopy (EDX), the ReB_2 phase could not be identified

unambiguously by X-ray diffraction (XRD) in the as-deposited state. A diffractogram of an area

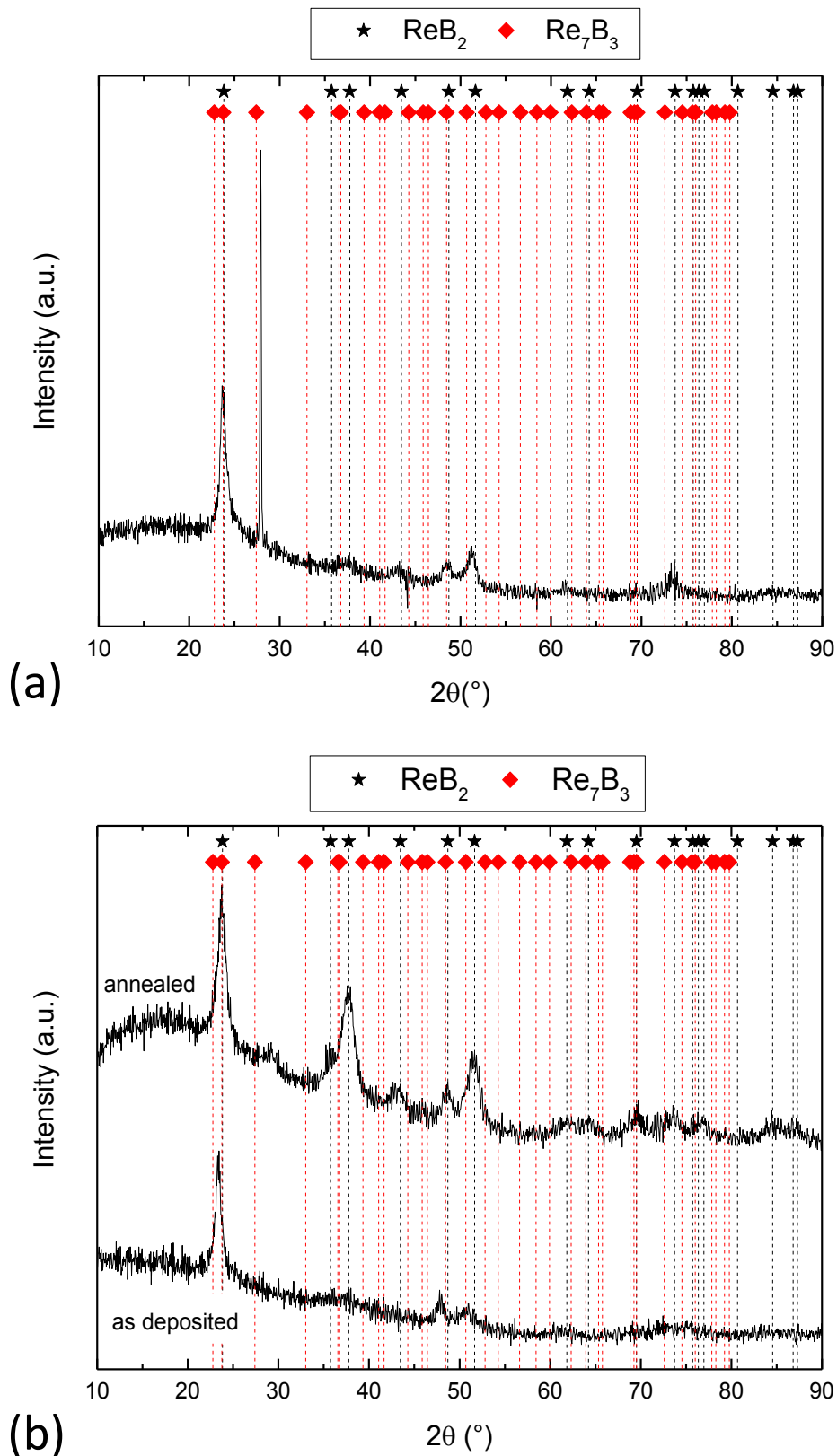


Figure 1.3: Diffractograms of areas on combinatorial samples deposited by pulsed DC magnetron sputtering with B concentrations of a) 66.6 at.% (Re 20 W, 2x B 100 W) and b) 67.8 at.% (Re 20 W, 2x B 120 W).

with 66.6 at.% B (taking into account only B and Re, no impurities) on a film grown with 20 W on the Re target and 100 W on each B target is shown in Figure 1.3 (a). The peaks at 2 Θ angles of 23.7°, 48.5°, 51.3°, and 73.5° cannot be clearly assigned to either the ReB₂ or Re₇B₃ phase considering that stresses in the films may slightly shift the peak position relative to the reference powder pattern, JCPDS cards 00-11-5081 and 00-13-0364, respectively. The high intensity narrow peak at 27.9°, however, does certainly not belong to ReB₂. The lower diffractogram in Figure 1.3 (b) is taken from an area with 67.8 at.% B on a sample grown with 20 W on the Re target and 120 W on each B target. The increase of the power applied to the B targets caused an increase of energy delivered to the growing film by the increased deposition flux. It is apparent that the structure changed, compared to the previous film (Figure 1.3 (a)), since the peak at 27.9° is not observed. Similarly, the peaks at 23.7°, 48.5°, and 51.3° cannot be clearly assigned to one of the contemplable phases. The upper diffractogram in Figure 1.3 (b) is taken from the same area after annealing the sample in a high vacuum furnace at 1000°C for one hour. After this treatment, stresses in the films appear slightly relaxed and the peak positions of the afore mentioned peaks show a better match with the ReB₂ powder reference. Furthermore, new peaks emerged at 35.7° and 37.8° which can be clearly attributed to ReB₂ but not to Re₇B₃. Hence, it seems that in the annealed state, the crystalline part of the film entirely consists of ReB₂. It can be inferred that the sample contains small crystallites, potentially embedded in an amorphous matrix, based on the large peak widths and the low peak-to-background ratio in the diffractogram of the annealed film (Figure 1.3 (b)). The halo or "hump" at lower angles can be an indication for the presence of an amorphous phase. A low hardness of 15.0(9) GPa measured by nanoindentation at 4 mN load supports this argument.

C impurities have been suggested before to prevent crystallization of complex B-rich BAM-type phases [45]. A large amount of C impurities (5 to 10 at.%) in Hunold's films detected by EDX may be an influence preventing the formation of ReB₂. If the energy of formation of ReB₂ increases substantially more than the energy of formation of Re₇B₃ upon C incorporation, formation of Re₇B₃ can become energetically more favorable, even if the local chemical composition is not ideal. The phase formation in Re-B films may also be understood in considering energetics in the sputtering process. The energy input through annealing suggests that enough

energy needs to be supplied to the growing film in the deposition process to form the equilibrium phase. This observation is consistent with the attempts obtaining Re_7B_3 phase impurities in bulk synthesis processes that can be considered to operate in thermal equilibrium [13, 28, 32, 39, 40], reviewed in the previous section. It is well known that film growth during sputtering does often not take place in thermodynamic equilibrium [46]. Energy can be supplied to the growing film by higher deposition temperature, suppression of thermalization of the sputtered film-forming species by reduction of the pressure-distance product, and/or energetic ion bombardment achieved by utilization of a substrate bias potential or higher plasma density. Substrate ion bombardment, primarily by working gas Ar^+ ions accelerated over the substrate sheath potential, can enhance adatom mobility on the substrate surface and may, thereby, enable the formation of the thermodynamically stable ReB_2 phase. Radio frequency (RF) magnetron sputtering can be utilized to increase the plasma density. It has been shown that phase-pure thermodynamically stable TiO_2 rutile phase can be synthesized by RF magnetron sputtering at otherwise same conditions leading towards synthesis of a mixture of anatase and rutile phases [47]. Similarly, the utilization of RF magnetron sputtering may enable formation of the thermodynamically stable ReB_2 phase. Based on these findings, future efforts to synthesize phase pure (in the as-deposited state) ReB_2 films by magnetron sputtering will have to investigate the effects of impurities and adatom mobility in the sputtering process.

One decade after ReB_2 has first been proposed by Chung et al. [1] as a superhard material that, in spite of the high cost of Re, may stand out as a protective coating, much more knowledge has been compiled in the studies reviewed above. The remarkable electronic structure of ReB_2 , accommodating both strongly directional covalent as well as metallic bonding has been investigated intensively by DFT [19–27, 29, 34, 35]. Numerous experimental studies highlight the importance of the synthesis procedure affecting the material's properties. Towards application, it has yet to be shown that phase-pure and chemically stable ReB_2 coatings with outstanding properties can be synthesized by physical vapor deposition methods that are widely established in industry, such as

magnetron sputtering.

Considering the reviewed aspects, the aim of this work is to study the phase formation in Re-B and Al/Ti-alloyed Re-B films and to contribute towards understanding the effect of alloying on microstructural evolution, mechanical properties, and chemical stability. To fulfill this goal, the effect of C impurities on phase formation and solubility of Al and Ti in ReB_2 will be assessed by density functional theory calculations of energies of formation. The DFT calculations will be followed by a hybrid radio frequency (RF)-DC magnetron sputtering synthesis of ReB_2 and Al/Ti-alloyed ReB_2 films. Hardness and elastic modulus will be measured by nanoindentation and related to the films' microstructure. The coatings' reactivity in air will be probed by X-ray photo-electron spectroscopy (XPS). Finally, an outlook on possible future research and applicability of ReB_2 -based coating systems will be given.

2. Methodology

2.1 Computational details

Electronic structure calculations were used to calculate energies of formation and elastic properties of pure ReB_2 , Re_7B_3 , and Re_4B_4 , as well as of these phases with a C impurity concentration of 8 at.%. B substitution by C was assumed in other atomically laminated materials [48]; therefore, B is randomly substituted by C. Supercells containing 162, 160, and 256 atoms were used for ReB_2 , Re_7B_3 , and Re_4B_4 , respectively. The meta-stable Re_4B_4 is also considered since its B:Re ratio lies between the other two phases. Energies of formation and elastic properties were also calculated for ReB_2 in which Re is randomly substituted by varying concentrations of Al and Ti (162 atoms per supercell) and for the opposite scenarios, substituting Re into the AlB_2 and TiB_2 structures (192 atoms per supercell).

The calculations were performed within the framework of density functional theory (DFT) employing the Vienna Ab initio Simulation Package (VASP) [49]. Projector-augmented wave potentials within PBE-GGA [50] were used, for which the projector functions were evaluated in real space for system containing more than 20 atoms. Tetrahedron method smearing with Blöchl

corrections [51] was used with an electronic convergence criterion of 10^{-4} eV. Amorphous systems were created by a liquid-quench method [52]. All systems were structurally relaxed, applying a conjugate-gradient algorithm with a force convergence criterion of 10^{-2} eV/Å. The equilibrium volume was found by a Birch-Murnaghan equation of state [53, 54] fit and for hexagonal and tetragonal systems, the c/a-ratio was optimized by a third order polynomial fit. Cutoff energies of basis sets were equal to the recommended value for the respective potential during dynamic relaxation and were further increased by 25% for static calculations. Integration in the Brillouin zone was performed on Γ -point-centered Monkhorst-Pack [55] k-point grids, converged to ≤ 1 meV per atom. Energy of formation for different compounds was calculated, relative to the elements, according to $E_f = E_{tot} - \sum_i n_i E_i$, where E_{tot} is the total calculated energy of the compound, n_i is the number of atoms of the i -th elemental species in the compound and E_i is the total energy per atom of the i -th elemental species in its ground state. Elastic constants were calculated by applying deformations to the cell geometry and fitting the change in total energy quadratically. Details were presented for cubic (here amorphous systems in cubic cells) and hexagonal systems by Music et al. [56] and Fast et al. [57], respectively. Macroscopic elastic quantities were calculated from elastic constants using the Hill (Reuss-Voigt average) method [58].

2.2 Experimental details

For this study, depositions of Re-B as well as Al/Ti-alloyed Re-B films were conducted. Magnetron sputter depositions were performed in a vacuum system with four 50 mm diameter magnetrons tilted 20° to the substrate normal at a target-substrate-distance of 12.4 cm. The focal point of each magnetron is 14.5 mm away from the center of the substrate holder. The average base pressure was below 6.67×10^{-5} Pa (5×10^{-7} Torr). Ar was used as sputtering gas and the working pressure was kept constant at 0.67 Pa (5×10^{-3} Torr). Re, Al, and Ti targets were powered by direct current (DC) supplies, whereas targets of B were powered by radio frequency (RF) supplies. The powers applied to the targets and the deposition time varied, depending on the desired composition and thickness of the films, respectively. Power on the metal targets was varied between 5 and 30

W, whereas power on B targets was varied between 140 and 200 W. Deposition time for thinner films (ca. 300 to 500 nm) varied between 45 and 60 minutes, while it varied between 120 and 150 minutes for thicker films (above 1 μm) intended for nanoindentation. Polished 50 mm diameter sapphire (0001) wafers were used as substrates for combinatorial thin film depositions, while thicker (combinatorial and homogenous) films, intended for mechanical characterization, were deposited onto polished 10x10x0.5 mm³ MgO (001) plates, on which no crack network formation is observed. MgO substrates were chosen for films to be characterized by nanoindentation since some of the films deposited on 50 mm sapphire (0001) wafers form crack networks with crack separations of around 10 μm . Depositions were performed at substrate temperatures of 300, 500, 700, and 900°C for Re-B films and at 900°C for Al/Ti-alloyed Re-B films. All substrates were coated with Mo on the backside for a better intake of radiative heat from the heater and were baked out for 20 minutes at deposition temperature, prior to deposition.

The phase composition was probed by X-ray diffraction (XRD) employing Cu K α radiation at a constant incident angle $\omega=10^\circ$ and a 2θ range from 10° to 100° in a Bruker AXS D8 Discover General Area Detection Diffraction System (GADDS). Stresses in some samples were evaluated by measuring at different ψ angles. The (103) peak was employed due to its location at a relatively high angle (51.7°) and sufficiently intensity at all ψ angles. Due to the non-Bragg-Brentano geometry, geometrical corrections were applied to the conventional [59] $\sin^2 \psi$ method. A modified $\psi^* = \frac{\psi}{|\psi|} \arccos(\cos \psi \cos \psi_0^*)$ with $\psi_0^* = \theta - \omega$ [60] is used and lattice plane spacings, d , are plotted as a function of $\cos^2(\theta - \omega) \sin^2 \psi^*$ with a stress free (sf) $\cos^2(\theta - \omega) \sin^2 \psi_{sf}^* = \frac{2\nu}{1+\nu} - \sin^2(\theta - \omega)$ [61]. To calculate stress from this plot, Poisson's ratios calculated by DFT and elastic moduli measured by nanoindentation were used. Due to the influence of crystalline mechanical anisotropy, crystallographic texture, and the presence of secondary phases in some samples, the residual stress values given here cannot be considered accurate and serve only as a crude comparison between samples. SEM images, also used for film thickness determination, were taken in a FEI Helios 660 system. Root mean square surface roughness of 2500 μm^2 areas was quantified by confocal laser scanning microscopy in a Keyence VK-9700 system with a resolution limit of ca. 20 nm.

Hardness and elastic modulus were investigated in a depth-sensing nanoindenter (Hysitron

TribolIndenterTM) with 100 nm radius Berkovich diamond tip at varying loads. 100 indentations were performed for each sample for better statistics. The tip area function was calibrated on a fused silica standard measured before and after the deposited films. Load vs. displacement curves showing pop-in events (not more than 22) were not considered for analysis (exceptions will be discussed). The Oliver-Pharr method [62] was applied to obtain the reduced elastic modulus. An elastic modulus of 1220 GPa and Poisson's ratio of 0.2 were assumed for the diamond tip and the Poisson's ratios calculated by DFT were assumed for the samples to calculate the samples' elastic moduli.

The chemical composition of the samples was analyzed by standard-less energy dispersive X-ray spectroscopy (EDX) with an EDAX Genesis 2000 analyzer at an electron beam acceleration voltage of 5 kV (10kV for Ti containing samples) in a JEOL JSM-6480 scanning electron microscope (SEM). Because of the expected reactivity [33, 42] of ReB₂, the chemical composition of a compound standard sample close to the surface can be expected to change over time upon repetitive air exposure and, thereby, falsify EDX measurements in which it is used as a standard. Hence, the chemical composition of the deposited films was measured by EDX directly after the deposition and samples were stored in a high vacuum vessel between all measurements. Selected samples were also analyzed by time-of-flight elastic recoil detection analysis (TOF-ERDA) at the tandem accelerator laboratory at Uppsala University. More details about the system can be found in [63]. The TOF-ERDA and EDX data will be compared. If not stated otherwise, chemical compositions reported were measured by EDX.

Surface chemical states were analyzed by X-ray photo-electron spectroscopy (XPS) in a JEOL JAMP-9500F system with an AlK_α X-ray source (1486.5 eV) and a hemispherical electron energy analyzer in fixed analyzer transmission mode with a pass energy of 20 eV and an electron take-off angle perpendicular to the analyzer. The energy resolution is assumed to be 0.15 eV. Energy calibration was carried out against the (Ar⁺ cleaned) Cu 2p 3/2 and 3p 3/2 lines. Charging of the sample was corrected against the C 1s peak of adventitious carbon set to 284.8 eV. Shirley backgrounds and Voigt functions were used for fitting the data.

3. Results and discussion

3.1 Energy of formation of Re-B and Re-B-C/Al/Ti systems

ReB_2 exhibits a lower energy of formation (-437 meV/atom.) than Re_7B_3 (-236 meV/atom.) or Re_4B_4 (+7 meV/atom.) (Figure 3.1 (a)). Accordingly, there is no energetic reason for the formation of Re_7B_3 in chemically pure Re-B films with a 1:2 composition.

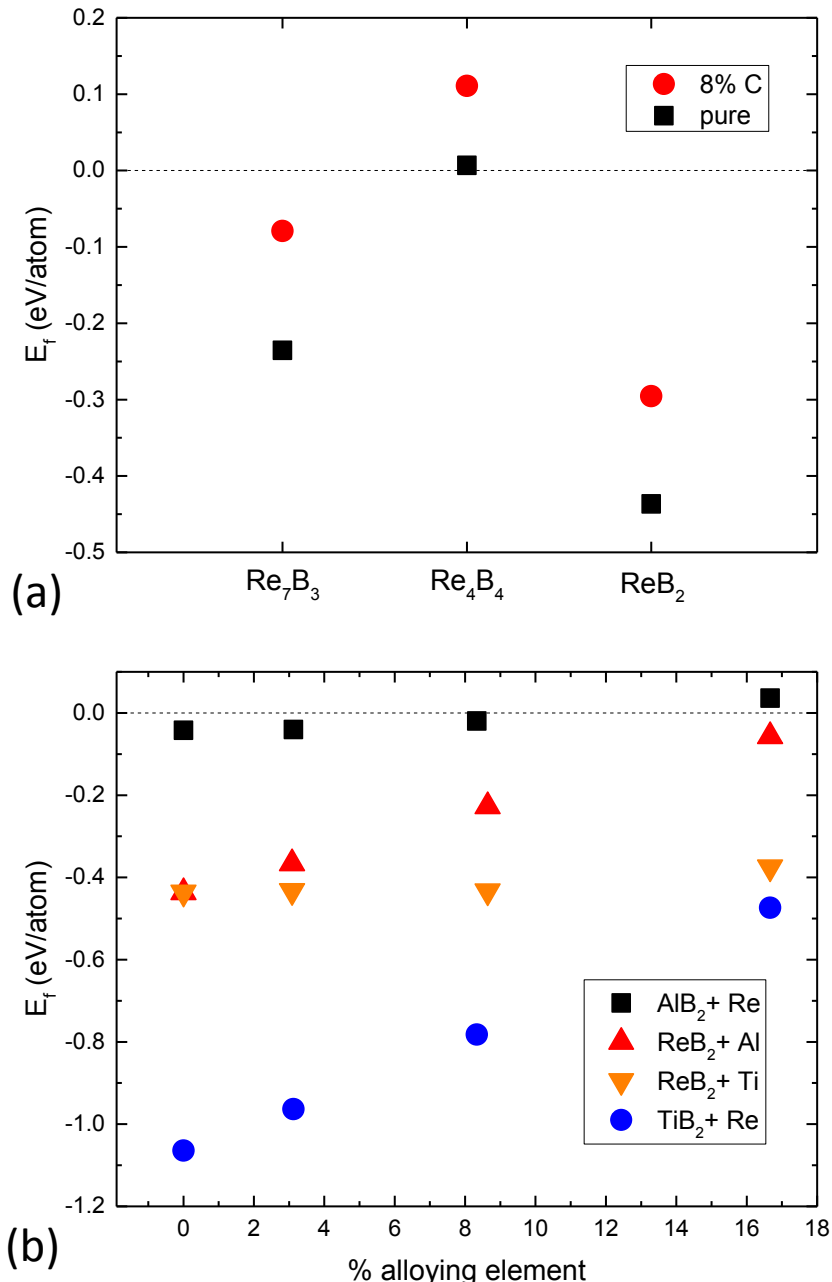


Figure 3.1: Energies of formation calculated by DFT for (a) phases in the Re-B system, ReB_2 , Re_7B_3 , and Re_4B_4 , pure and with carbon incorporation, and for (b) alloyed diborides as a function of alloying element concentration.

Effect of C incorporation

C impurities may be the cause of the impaired phase formation of ReB_2 , as reviewed in Section 1.2. C incorporation increases the energy of formation for all phases similarly, between 104 and 157 meV/at. (Figure 3.1 (a)). The energy of formation of C-doped ReB_2 with 8 at.% of C is lower than C-doped or even pure competing Re-B phases. Furthermore, a visual inspection of the relaxed ReB_2 supercell reveals that the substitution of B with C only very little distorts the crystal structure. These results suggest that the presence of C impurities in Re-B films cannot explain the preferred formation of Re_7B_3 in previous experiments (Section 1.2).

Effect of Al/Ti-alloying

In the following, the random substitution of Re with Al and Ti is investigated computationally by calculating energies of formation to assess if a solid solution could be formed. The opposite scenarios, substituting Re into the AlB_2 and TiB_2 structures, are considered (only computationally) as well. The energy of formation as a function of alloying element concentration for the afore mentioned systems is displayed in Figure 3.1 (b). The highest concentration of 16.7 at.% corresponds to substitution of half of the metal atoms. For all combinations, except Re-alloyed AlB_2 , the energy of formation remains negative even upon replacement of half of the metal atoms. It linearly increases for Al-alloyed ReB_2 with increasing Al concentration, almost up to 0 eV/at. This trend has to be compared to the possible competing phases, AlB_2 and AlB_{12} , to assess solubility. The energy of formation of pure AlB_2 (-42 meV/at.) is higher than that of any of the Al-alloyed ReB_2 systems (Figure 3.1 (b)). The energy of formation for $\alpha\text{-AlB}_{12}$ is -114 meV/at. [64], which is equivalent to Al-alloyed ReB_2 with about 14 at.% Al. Based on these considerations, a $(\text{Re},\text{Al})\text{B}_2$ solid solution with Al concentrations of up to 14 at.% is likely without formation of Al-boride phases.

The energy of formation only shows a minor increase for Ti-alloyed ReB_2 with increasing Ti concentration. TiB_2 , contrary to AlB_2 , has a much lower energy of formation (-1064 meV/at., see Figure 3.1 (b)). Energies of formation of other Ti-borides, Ti_3B_4 (-932 meV/at.), Ti_2ReB_2 (-833 meV/at.) [65], are also lower than that of any of the Ti-alloyed ReB_2 systems. Hence, the formation of these Ti-boride phases is likely upon alloying Ti into ReB_2 . However, the calculations

were performed at 0 K, so a possible entropic stabilization of a solid solution at higher temperatures is not considered. Furthermore, a small amount of Ti-boride impurities may be tolerable in applications, considering the promising elastic properties of the Ti-boride phases (e.g. TiB_2 , calculated $G=253 \text{ GPa}$, only 11% smaller than that of ReB_2).

The calculations of energies of formation discussed above show that C impurities are rather unlikely to be the major reason for previously observed Re_7B_3 phase impurities in Re-B thin films. Moreover, it is suggested that alloying Al and Ti to ReB_2 may result in solid solutions or phase mixtures, respectively.

3.2 Phase formation of Re-B and Al/Ti-alloyed Re-B films

Re-B films

The composition of the deposited films was measured by EDX. To assess the error in the standard-less EDX measurements, five films (two Re-B, two Al-alloyed Re-B, one Ti-alloyed Re-B, all stored in a high vacuum vessel between measurements) are also analyzed by TOF-ERDA. The average deviation from the EDX results are +1(1)%, -1(2)%, +5%, and -1(3)% for Re, Al, Ti, and B, respectively. The limited amount of data is insufficient to construct a correction scheme for the EDX results. Nevertheless, the deviations (except for Ti) are low; hence, a correction is considered unnecessary. The concentrations reported in the following do only consider the intentionally introduced elements (Re, Al, Ti, B) and no impurities. However, the TOF-ERDA data reveals that the samples contain on average around 2.5(5)% Fe and 4.4(8)% C impurities which are possibly stemming from the RF sputtered chamber walls and B targets, respectively.

The combinatorial films exhibit a Re chemical gradient, as can be deduced from the depiction of the target positions, the wafer, and the measurement grid on the right side of Figure 3.2. The Re gradient is not perfectly symmetric with respect to the positions of the B targets, likely caused by the not perfect chamber geometry and the RF matching-networks inducing a different target self-bias on the two B targets (e.g. due to different target thickness and race track depth), which in

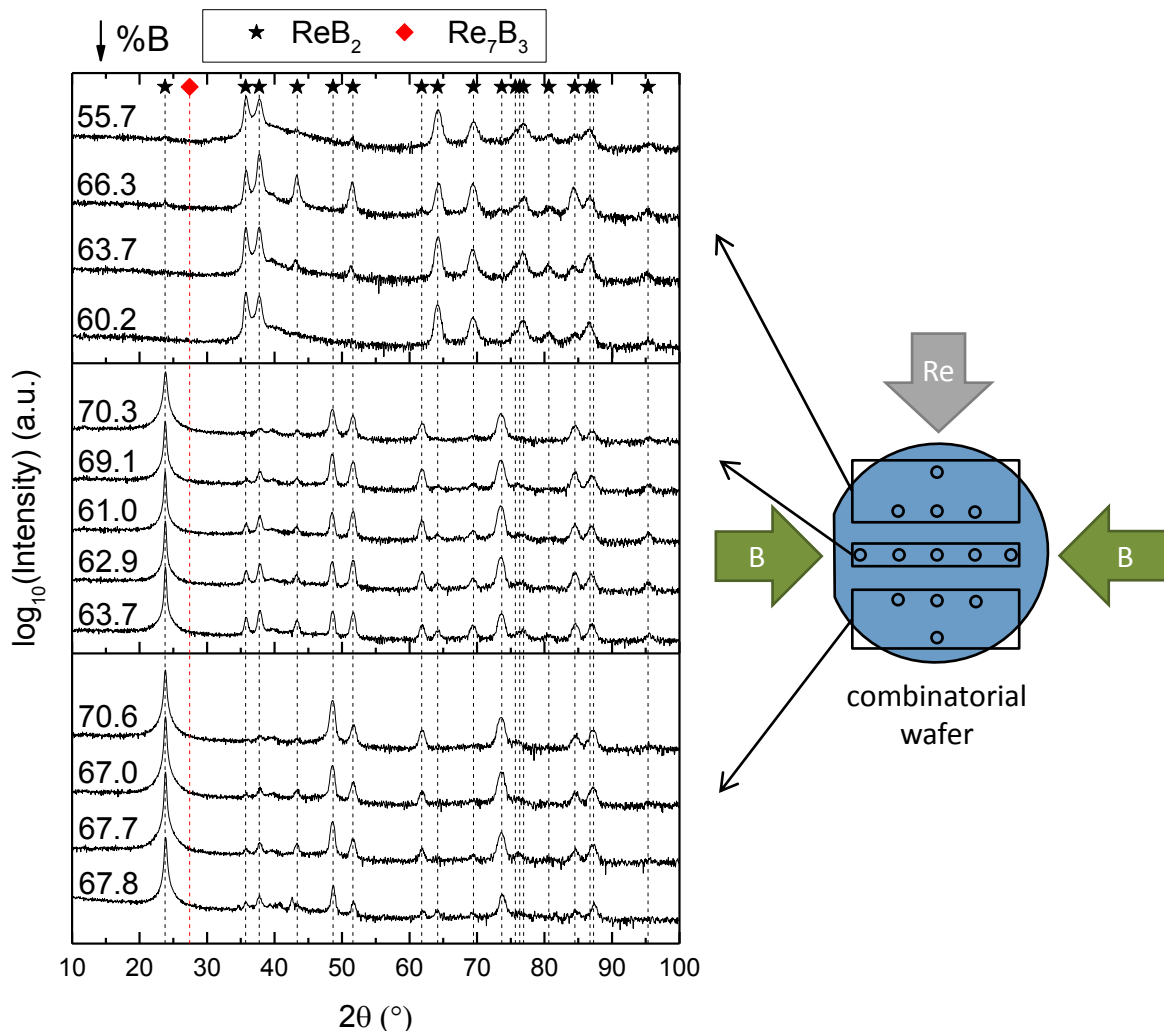


Figure 3.2: Diffractograms (left) of different areas on a combinatorial film (right) deposited on sapphire (0001) at 900°C (Re 20 W, 2x B 149 W). The B concentration is given on the left of the diffractograms and ReB₂ peak positions are indicated by drop-lines.

turn results in different sputter yields and ion currents. Diffractograms of different spots on a Re-B combinatorial film, deposited at 900°C, are shown in Figure 3.2. On the left of every diffractogram, the EDX-measured B content is stated. All peaks of the ReB₂ structure (JCPDS card 00-11-0581) are observable, as indicated by the dashed drop-lines. The peaks visible at 35.7°, 37.8°, 43.3°, 51.6°, 73.7°, 84.5°, 86.8°, 87.3°, and 95.3° can be clearly attributed to ReB₂ but not to Re₇B₃ (JCPDS card 00-13-0364). Furthermore, the large and narrow peak at 27.9° that was an indicator for the presence of Re₇B₃ in previous experiments (cf. Figure 1.3 (a)) is not visible in any of the diffractograms in Figure 3.2. Accordingly, all measured areas consist of X-ray phase pure ReB₂, which is successfully synthesized by magnetron sputtering in the as-deposited state. The measured points further away

from the Re target show a strong (0002) (23.7°) texture (Figure 3.2, note logarithmic intensity). It is reasonable to assume that the puckered Al hexagons in the sapphire (0001) plane provide a template effect for the Re hexagons in the ReB_2 (0001) plane which leads to texture formation as the linear lattice mismatch is only -4.3%. The areas closer to the Re target, however, do not exhibit such texture. Energetic Ar atoms ($m_{\text{Ar}}=39.95$ amu), back-scattered from the heavier atoms in the Re target ($m_{\text{Re}}=186.21$ amu), may explain the absence of this particular texture. Such energetic particle bombardment can introduce defects resulting in grain re-nucleation, thereby, eliminating the substrate influence.

With decreasing deposition temperature from 900 to 300°C, the peak widths increase and the peak-to-background ratios decrease until no peaks are visible. This indicates a reduction of the crystallite size with reduced deposition temperature until X-ray amorphous films are formed below 500°C. Phase formation with the B content as a function of deposition temperature is shown in Figure 3.3. Crystalline ReB_2 can be synthesized down to 500°C in this mixed RF-DC magnetron sputtering process. Interestingly, the composition range for crystalline ReB_2 growth of about 55 to

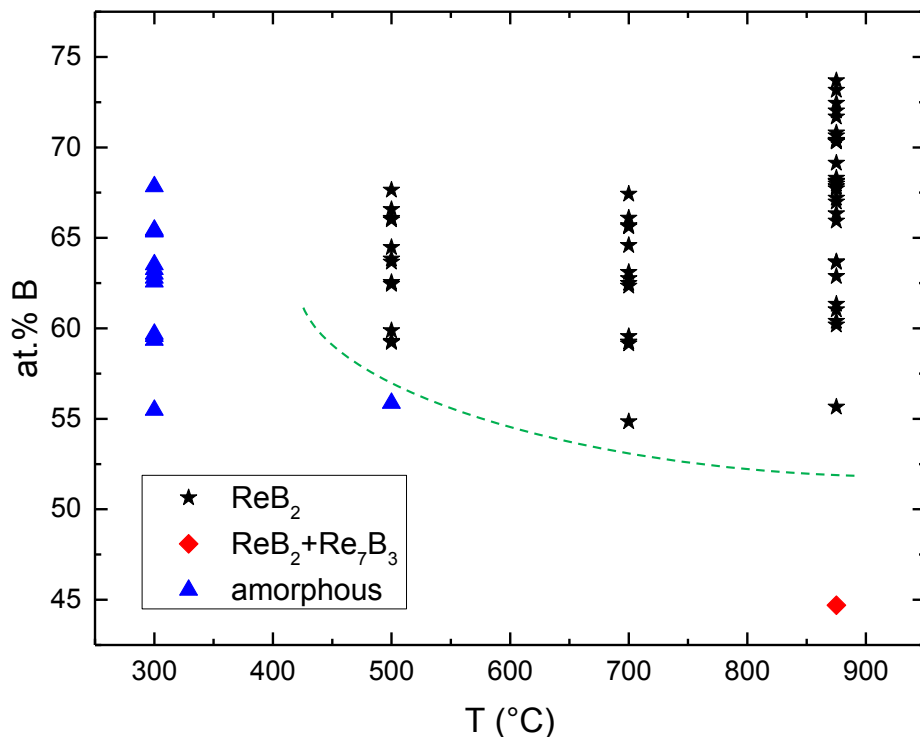


Figure 3.3: Phase formation map showing the phases identified by XRD as a function of deposition temperature, T , and B concentration. The dashed line indicates the boundary up to which crystalline ReB_2 can be synthesized.

75 at.% B is relatively large compared to the homogeneity range of about 65 to 71 at.% B reported by Portnoi et al. [2] at 1600°C (Figure 1.1). This can indicate that the synthesized films meta-stably support more Re or B lattice vacancies than in thermodynamic equilibrium and/or that the excess atomic species form amorphous residua or X-ray-undetectable tissue phases between the grains.

Al-alloyed Re-B films

Three representative diffractograms taken from Al-alloyed Re-B samples with different Al content are shown in Figure 3.4 (a). Al and B concentrations are given right and left hand side of the graphs, respectively. The ReB_2 structure is completely preserved at a low Al concentration of 2.6 at.% (Figure 3.4 (a) bottom diffractogram). An incipient formation of AlB_{12} can be observed at 13.9 at.% Al (Figure 3.4 (a) center diffractogram), whereas it is present in much larger quantities at 29.0 at.% Al (Figure 3.4 (a) top diffractogram). More data from Al-alloyed Re-B samples is summarized in a ternary phase diagram in Figure 3.4 (b). Up to an Al concentration of 13.6 at.%, the films grow (X-ray) purely in the ReB_2 structure. This observation is in excellent agreement with the theoretical solubility predictions of approximately 14 at.% Al, discussed previously (Section 3.1).

Ti-alloyed Re-B films

Three representative diffractograms taken from Ti-alloyed Re-B samples with different Ti content are shown in Figure 3.5 (a). The ReB_2 structure is preserved at a low Ti concentration of 2.6 at.%, as for the Al-alloyed sample. However, the broader peak widths indicate smaller or more defect-rich crystallites. In contrast to the Al-alloyed samples, Ti-boride impurity phases are clearly present at much lower alloying element concentrations of 5.5 at.% Ti and 12.7 at.% Ti, which can be observed in the center and top diffractograms, respectively. Identification of the Ti-boride phases, TiB_2 , Ti_3B_4 , and Ti_2ReB_2 , is limited due to too narrow differences between reference peak positions and mechanical stress in the films that might shift peak positions relative to powder references. More data from Ti-alloyed Re-B samples is summarized in a ternary phase diagram in Figure 3.5 (b) (note that the axis are scaled differently than in Figure 3.4 (b)). Ti can be alloyed into the film only up to 3.9 at.% before other phases than ReB_2 become detectable by XRD. This

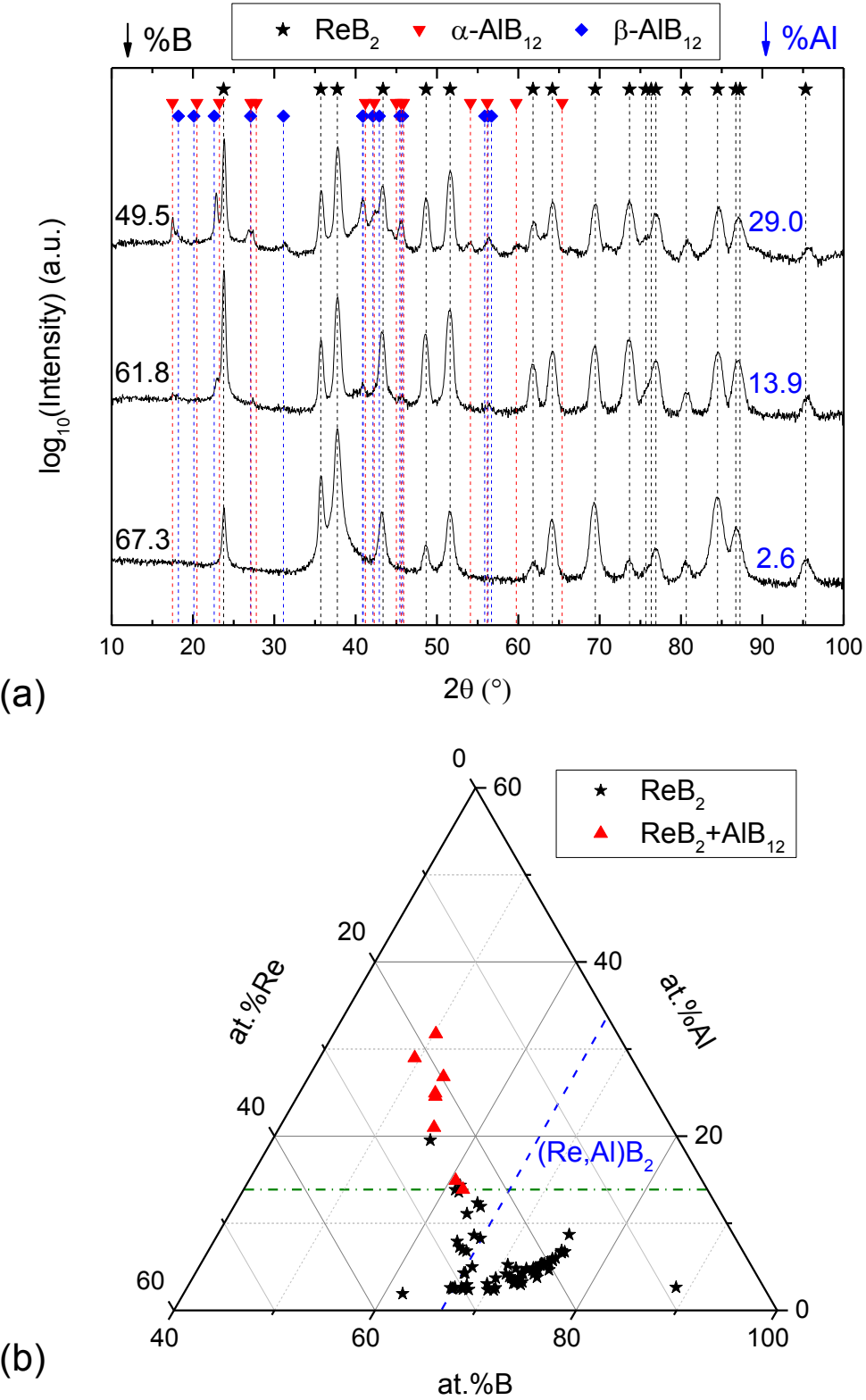


Figure 3.4: (a): Diffractograms of selected samples with varying Al concentration. The Al and B concentrations are given on the right and left of the diffractograms, respectively, and peak positions of the identified phases are indicated by drop-lines. (b): Ternary phase diagram shows the phases identified by XRD as a function of chemical composition. The dashed blue line indicates an ideal $(\text{Re}, \text{Al})\text{B}_2$ solid solution and the dash-dotted green line indicates the Al concentration up to which only the ReB_2 structure can be detected by XRD.

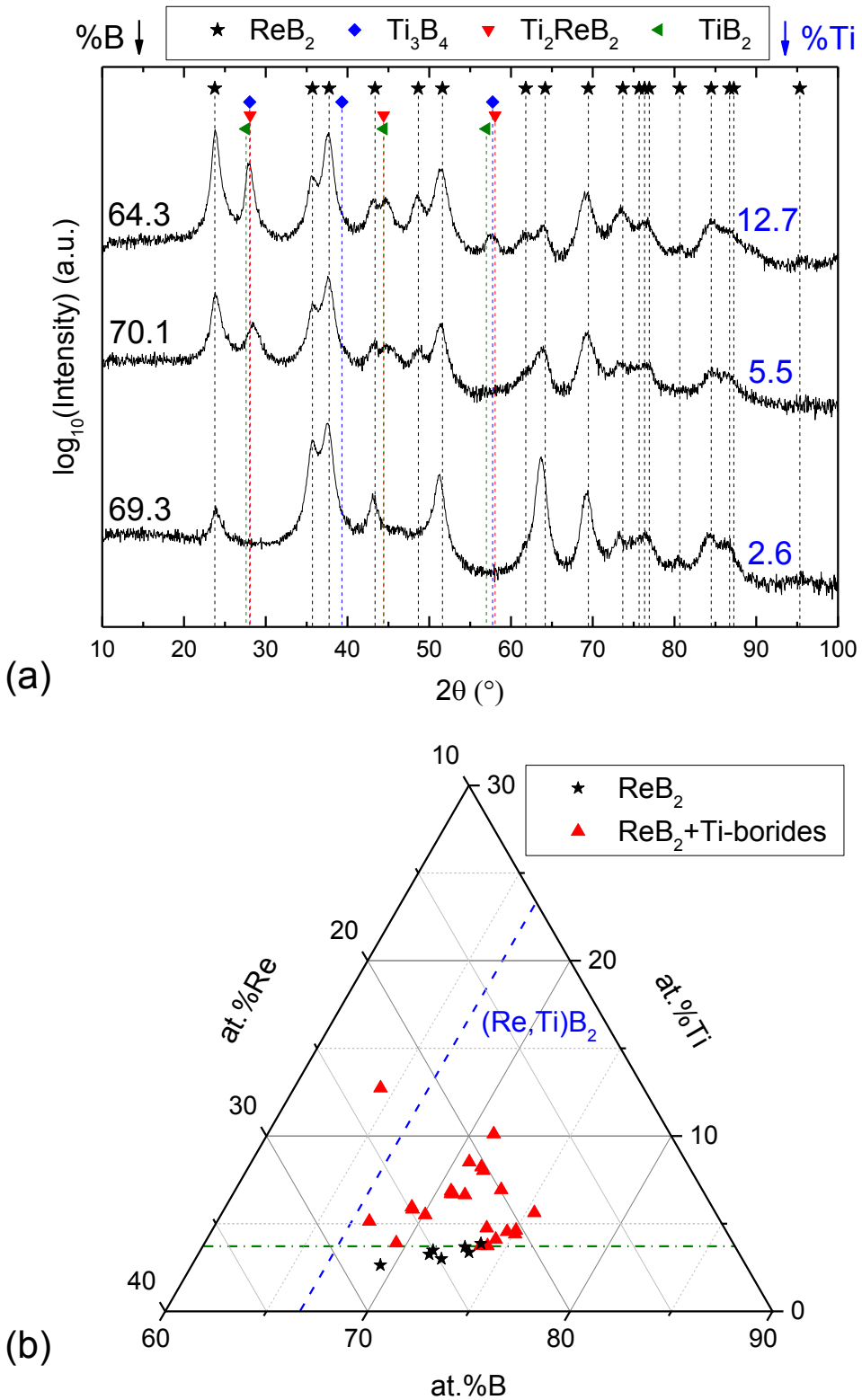


Figure 3.5: (a): Diffractograms of selected samples with varying Ti concentration. The Ti and B concentrations are given on the right and left of the diffractograms, respectively, and peak positions of the identified phases are indicated by drop-lines. (b): Ternary phase diagram shows the phases identified by XRD as a function of chemical composition. The dashed blue line indicates an ideal $(\text{Re}, \text{Ti})\text{B}_2$ solid solution and the dash-dotted green line indicates the Ti concentration up to which only the ReB_2 structure can be detected by XRD.

relatively low concentration, compared to the Al-alloyed samples, is also consistent with theoretical predictions, considering that Ti-borides have lower energies of formation than the Ti-alloyed ReB_2 systems (Section 3.1).

The structural and chemical analysis discussed above shows that it is possible to grow (X-ray) phase-pure ReB_2 films by hybrid RF-DC magnetron sputtering in the as-deposited state over a wide composition range of about 55 to 75 at.% B. Furthermore, Al can be alloyed into ReB_2 films without formation of other phases up to an Al concentration of 13.6 at.%, whereas alloying of Ti causes formation of Ti-borides above a Ti concentration of 3.9 at.%. Based on these results, it seems likely to obtain a potentially superhard and yet metallic coating without or with only small amounts of secondary phases.

3.3 Mechanical properties and microstructure

Re-B films

Hardness and elastic modulus are measured by nanoindentation. The samples discussed in this Section 3.3 are labeled alphabetically (A to C for Re-B, D to I for Al-alloyed Re-B, and J to N for Ti-alloyed Re-B films). Three ReB_2 samples with similar chemical composition (A (66.2 at.% B) and B (68.3 at.% B): symmetry equivalent positions in the same combinatorial deposition; C (62.3 at.% B): central position in a homogenous deposition) will be considered. The measured elastic modulus, E , and hardness, H , of these ReB_2 samples (A, B, C) as a function of indentation load is shown in Figure 3.6 (a) and (b), respectively. The calculated values for E of pure ReB_2 , ReB_2 with 8 at.% C incorporation, and amorphous ReB_2 are plotted as reference lines (Figure 3.6 (a)). E does not significantly vary with load or among the samples; however, E is almost 25% lower than the theoretically predicted value. Contrary to the indentation size effect reported in literature [1], H appears to increase with increasing load (within error bars) and saturates approximately at 30 GPa at maximum load of 10 mN, which is well within the range of values reported in literature, though, does not reach the superhardness benchmark of 40 GPa as in

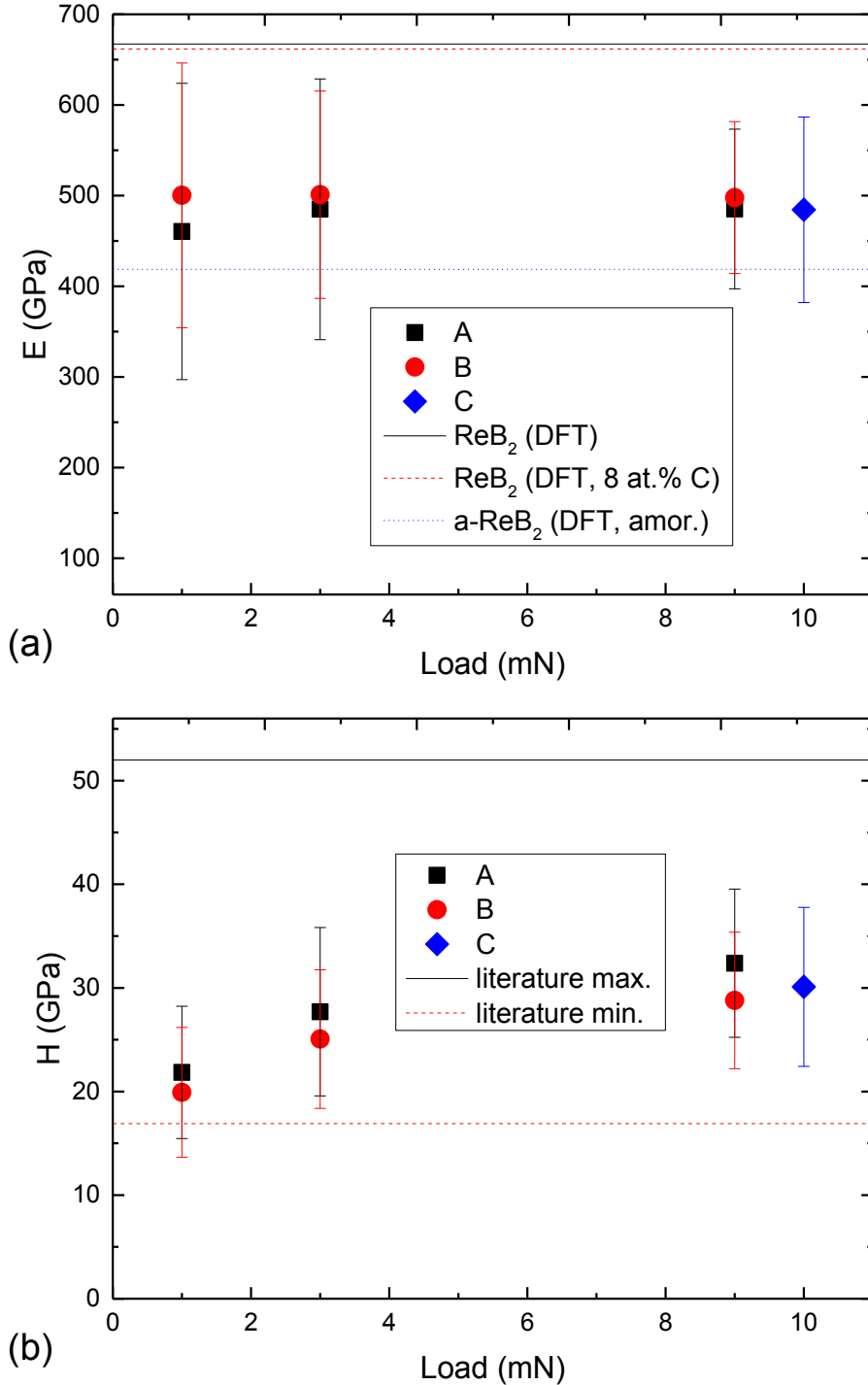


Figure 3.6: (a) Elastic modulus, E , (E calculated by DFT are inserted as reference lines) and (b) hardness, H , (literature min. [30] and max. [9] H are inserted as reference lines) of three ReB_2 films with a similar chemical composition (62.3 to 68.3 at% B) deposited on MgO (001) at 900°C as a function of indentation load.

some other studies (cf. Section 1.1). Furthermore, both E and H values exhibit a very large standard deviation, whereas that of E decreases with increasing load. These effects can be reasoned by supplemental data given in Table 3.1. The indentation depth did not exceed the

Sam.	P (mN)	H (GPa)	E (GPa)	h (nm)	D (μm)	R_q (nm)	σ_{\parallel} (GPa)	R^2	%B
A	1	22(6)	460(163)	23(6)	1.07(5)	43(10)	n.a.	n.a.	66.2*
	3	28(8)	485(144)	46(10)					
	9	32(7)	485(88)	84(12)					
B	1	20(6)	500(146)	26(8)	1.13(4)	28(3)	-4.3(8)	0.98	68.3
	3	25(7)	501(114)	48(9)					
	9	29(7)	498(84)	90(12)					
C	10	30(8)	484(102)	91(17)	1.53(6)	39(4)	-5(1)	0.99	62.3

Table 3.1: Supplemental data for the ReB_2 films deposited on MgO (001) at 900°C used in Figure 3.6. The columns show maximum load during nanoindentation, P , hardness, H , elastic modulus, E , indentation depth, h , film thickness, D , root mean square surface roughness, R_q , in-plane residual stress measured by XRD, σ_{\parallel} , coefficient of determination of the linear strain-fit, R^2 , and the B concentration in at.%. *

*Measured by TOF-ERDA.

conventional 10% of the film thickness; hence, it is unlikely that the increasing hardness with increasing load is influenced by the substrate. It seems more likely that the high surface roughness ($R_q=28$ to 43 nm measured by confocal laser microscopy, compared to a 100 nm radius indenter tip) and porosity are responsible for relatively low measured stiffness and hardness, the high standard deviations, and the apparent increase of H with increasing indentation depth. A better impression of the films' microstructure can be gained from the top and cross-section SEM images of sample C in Figure 3.7 (a) and (b), respectively. The surface exhibits features several hundred nanometers in size as well as dark areas which are considered to be pores. The cross-section image shows darker regions that are likely to indicate pores throughout the entire film. Porosity would certainly lower stiffness and hardness, relative to values predicted for the fully dense material.

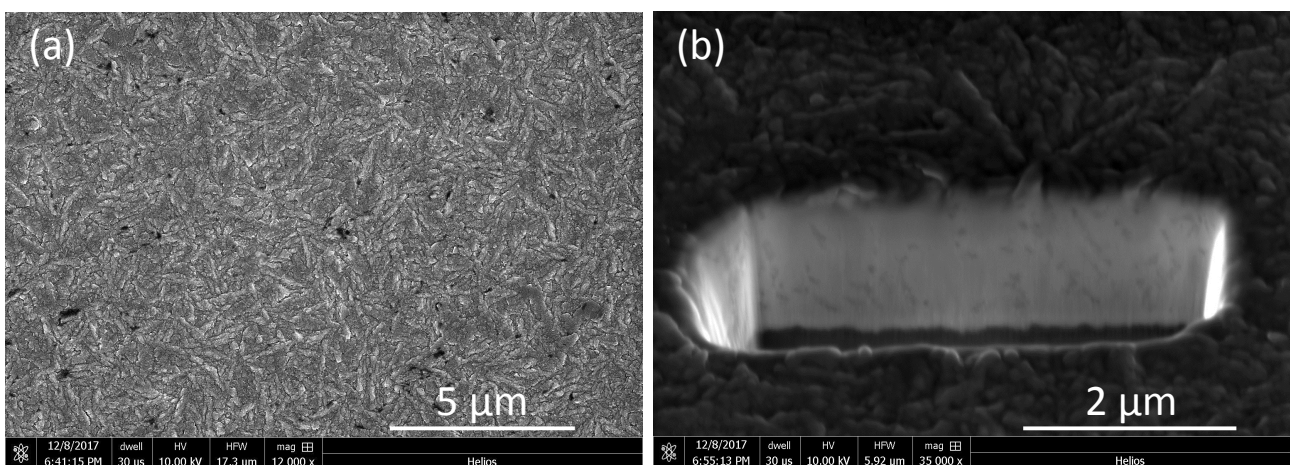


Figure 3.7: SEM images of (a) the surface and (b) cross-section of sample C (central position in a homogenous Re-B deposition on MgO (001) at 900°C , cf. Table 3.1).

When indenting into a smaller surface asperity, there is no material on the sides which would oppose plastic deformation; hence, H is relatively low at low loads. With increasing indentation depth, more material has to be deformed and the influence of surface asperities is reduced; consequently, H increases. The high compressive residual stresses (Table 3.1) in the main body of the film may also contribute to increasing measured hardness, as they can give rise to higher real contact areas, which can lead to overestimated elastic modulus and hardness when the Oliver–Pharr method is employed [66, 67]. If smoother and denser films with a more homogenous microstructure could be grown, it seems reasonable to assume that superhardness can be achieved.

Al-alloyed Re-B films

In the following, mechanical properties and microstructure of Al-alloyed Re-B films (2.4 to 21.0 at.% Al) will be presented and discussed. Measured and calculated elastic modulus as well as measured hardness as a function of Al concentration are shown in Figure 3.8 (a) and (b), respectively. Supplementary data of the films, such as nanoindentation results, film thickness, roughness, stress, and B content, is given in Table 3.2 (D to I). The measured E falls monotonously with increasing Al concentration, as predicted by calculated values, however, with a steeper slope than calculated values and is about 30 to 60% lower than the calculated values (excluding sample F). The measured H also decreases with increasing Al content (note that the last two data points

Sam.	H (GPa)	E (GPa)	h (nm)	D (μm)	Rq (nm)	$\sigma_{ }$ (GPa)	R^2	%B
D	26(6)	471(81)	96(14)	1.44(4)	26(8)	-4.3(7)	1.00	67.6***
E	19(6)	396(81)	117(22)	1.31(4)	39.3(5)	-3.2(7)	0.98	67.3
F	40(5)	562(56)	72(8)	1.83(9)	18(2)**	-3.2(5)	0.92	72.4
G	17(4)	407(71)	123(16)	1.42(7)	45(1)	-2.5(5)	0.89	70.6
H	4(2)	209(78)	344(111)*	1.5(1)	221(5)	-1.5(6)	0.98	67.7***
I	1(1)	120(48)	608(155)*	2.0(3)	398(9)	-0.6(2)	0.86	55.4

Table 3.2: Supplemental data for the Al-alloyed ReB_2 (D to I) films deposited on MgO (001) at 900°C used in Figure 3.8. The columns show hardness, H , elastic modulus, E , indentation depth, h , film thickness, D , root mean square surface roughness, R_q , in-plane residual stress measured by XRD, $\sigma_{||}$, coefficient of determination of the linear strain-fit, R^2 , and the B concentration in at.%.

*Indentation depth is more than 10% of the film thickness.

**Resolution of the microscope is assumed to be 20 nm so these values might not be accurate.

***Measured by TOF-ERDA.

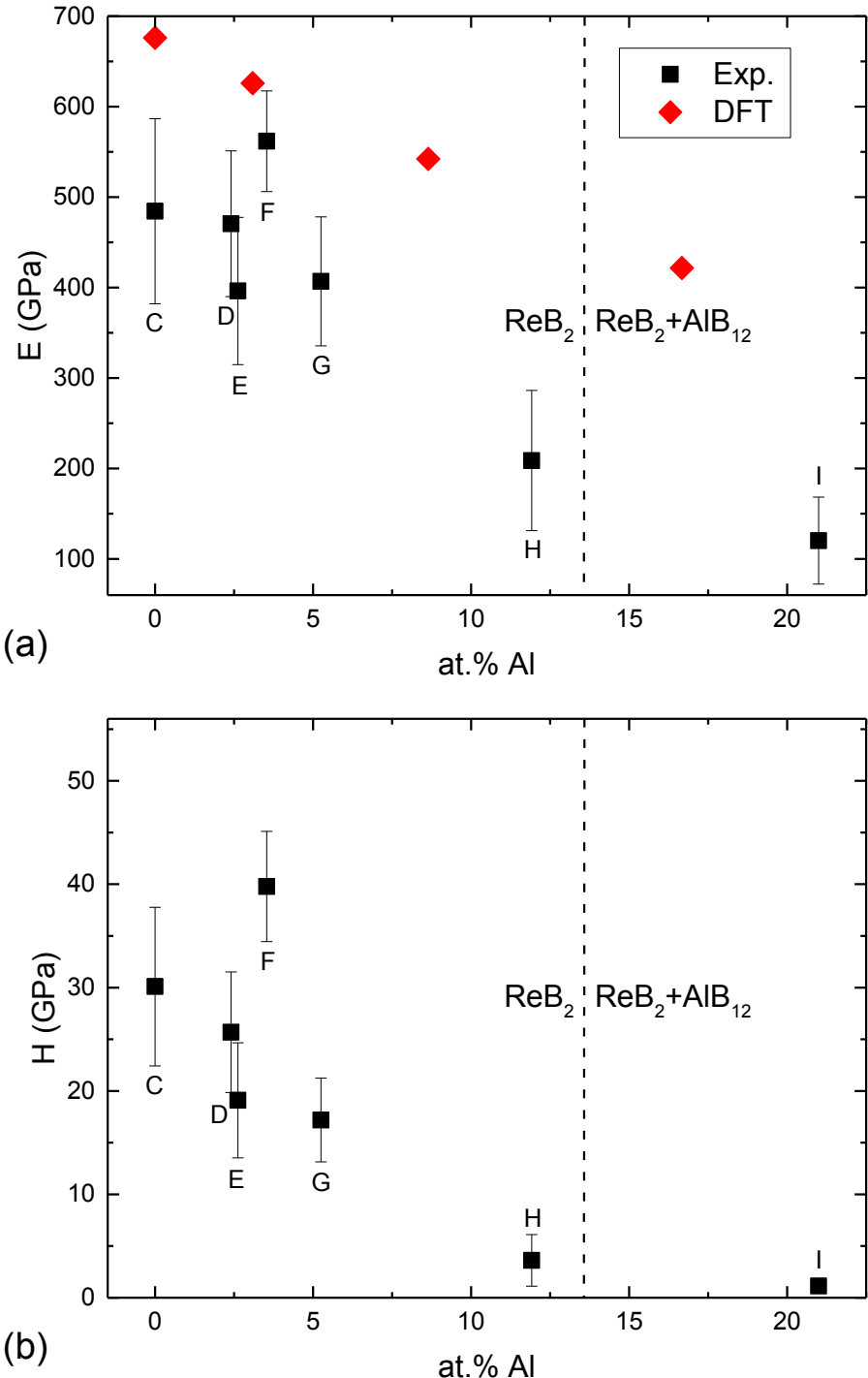


Figure 3.8: a) Measured and calculated elastic modulus, E , and b) measured hardness, H , of Al-alloyed samples as a function of Al concentration. The dashed line indicates the concentration at which secondary phases were detected by XRD.

cannot be considered accurate due to the high indentation depth). Sample F, on the contrary, stands out as its E (562 GPa) is only 9% lower than the predicted value and its H (40 GPa) is extraordinarily high. For this sample, the measurement was performed twice (200 indents in total) and the results were reproducible. A closer look on the samples' microstructure, again, reveals why

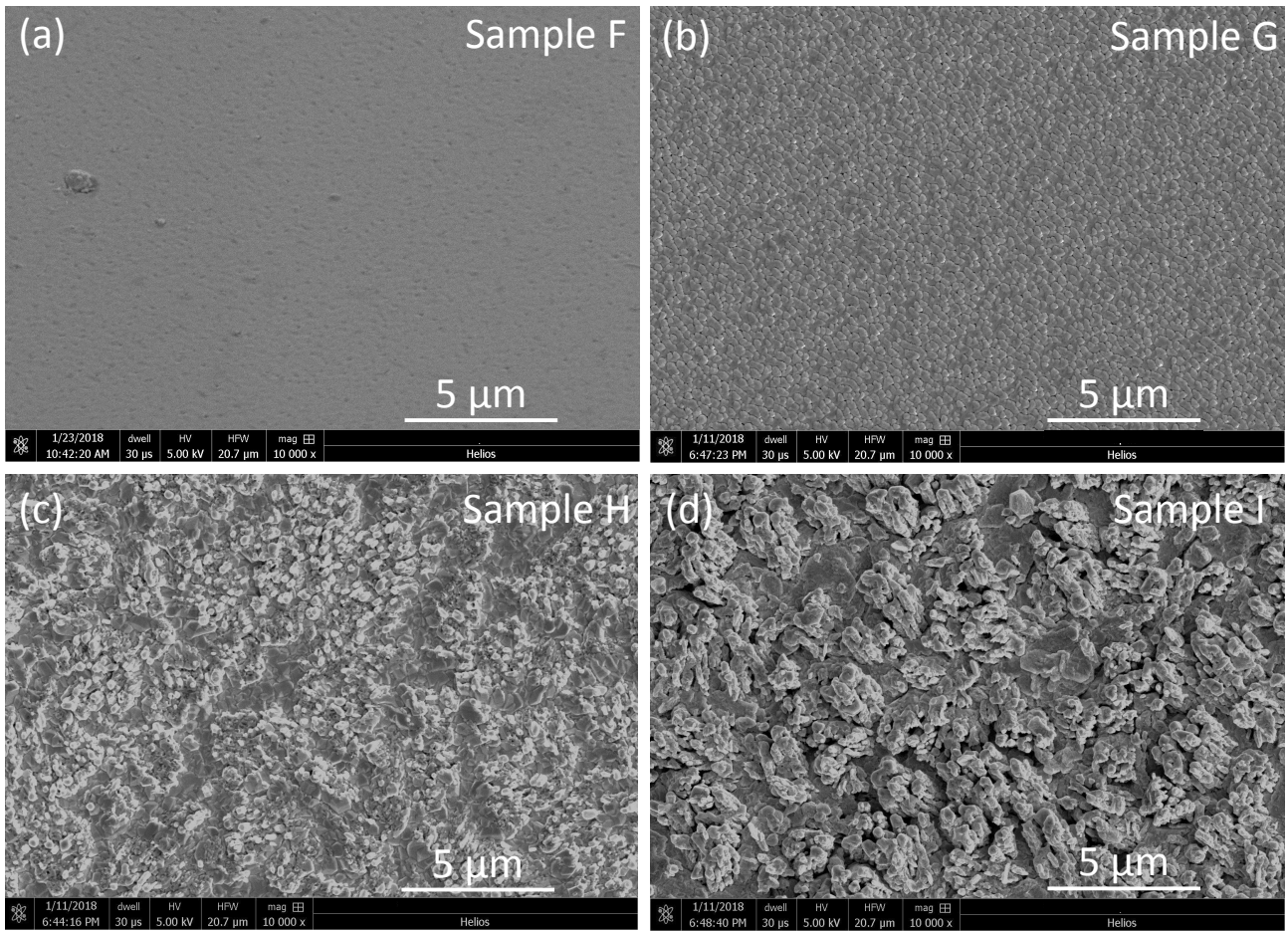


Figure 3.9: SEM overview images of the Al-alloyed Re-B samples (a) F, (b) G, (c) H, and (d) I, deposited on MgO (001) at 900°C.

stiffness and hardness decrease so rapidly with increasing Al concentration and why sample F exhibits outstanding properties. SEM overview images of samples F, G, H, and I are depicted in Figure 3.9 (a), (b), (c) and (d), respectively. Sample F has a smooth and dense surface with only isolated larger asperities. Sample G (and also D and E, not shown here) shows a rougher structure with features with the size of about 200 to 400 nm. With increasing Al concentration, the roughness is strongly enhanced, as can be seen in Figure 3.9 (c) and (d). The surface roughness measured by confocal laser microscopy (see Table 3.2) supports the qualitative SEM observations and almost all load-displacement curves of samples H and I showed pop-in events (so for these samples they were not excluded), which indicate high porosity. As discussed before for the unalloyed ReB_2 samples, high roughness and porosity are most likely the reason for lower than expected measured stiffness and hardness. The deposition temperature of 900°C is already far above the melting point of Al (660°C). It is reasonable to assume that eruptive Al evaporation causes roughening of the films

in the sputter process. It remains unclear why sample F is much smoother and denser than other samples with a similar Al concentration (D, E, G). As it is desirable to grow coatings with such a microstructure, a strategy for future depositions could be to reduce the deposition temperature and increase the degree of ionization of sputtered species. This could, for example, be achieved by utilizing high power pulsed magnetron sputtering (HPPMS), which is known to produce dense and smooth coatings [68].

Ti-alloyed Re-B films

Measured and calculated elastic modulus as well as measured hardness of Ti-alloyed Re-B films (3.9 to 12.7 at.% Ti) as a function of Ti concentration are shown in Figure 3.10 (a) and (b), respectively. Supplementary data on the samples can be found in Table 3.3 (J to N). While calculated E decreases with increasing Ti concentration, the measured values scatter around 500 GPa without showing a notable dependence on the Ti concentration. This can be reasoned by the increasing amount of secondary Ti-boride phases which have high calculated elastic moduli themselves (569, 486, and 454 GPa for TiB_2 , Ti_3B_4 , and Ti_2ReB_2 , respectively [65]). H even increases with increasing Ti concentration from 30 GPa at 0 at.% Ti up to 40 GPa at 12.7 at.% Ti. Furthermore, the standard deviations are smaller and compressive residual stresses are higher (cf. Table 3.3) than those of the unalloyed or Al-alloyed Re-B films. SEM overview images of samples K and N, displayed in Figure 3.11 (a) and (b), respectively, show that the Ti-alloyed samples are comparably smooth and show no sign of porosity. The sample with the highest Ti

Sam.	H (GPa)	E (GPa)	h (nm)	D (μm)	Rq (nm)	$\sigma_{ }$ (GPa)	R^2	%B
J	38(3)	510(30)	70(4)	1.67(5)	11.0(0)*	-6.1(4)	0.99	69.5
K	39(2)	498(20)	68(3)	1.80(4)	11.0(0)*	-6.7(4)	0.99	74.3
L	35(3)	465(26)	74(4)	1.38(5)	16(1)*	-6.4(4)	0.99	73.5
M	37(3)	485(26)	71(4)	1.54(4)	14(2)*	-5.8(9)	0.88	73.1
N	40(2)	519(14)	67(2)	1.87(3)	15(2)*	-6.2(3)	0.98	64.3**

Table 3.3: Supplemental data for the Ti-alloyed ReB_2 (J to N) films deposited on MgO (001) at 900°C used in Figure 3.10. The columns show hardness, H , elastic modulus, E , indentation depth, h , film thickness, D , root mean square surface roughness, R_q , in-plane residual stress measured by XRD, $\sigma_{||}$, coefficient of determination of the linear strain-fit, R^2 , and the B concentration in at.%.

*Resolution of the microscope is assumed to be 20 nm so these values might not be accurate.

**Measured by TOF-ERDA.

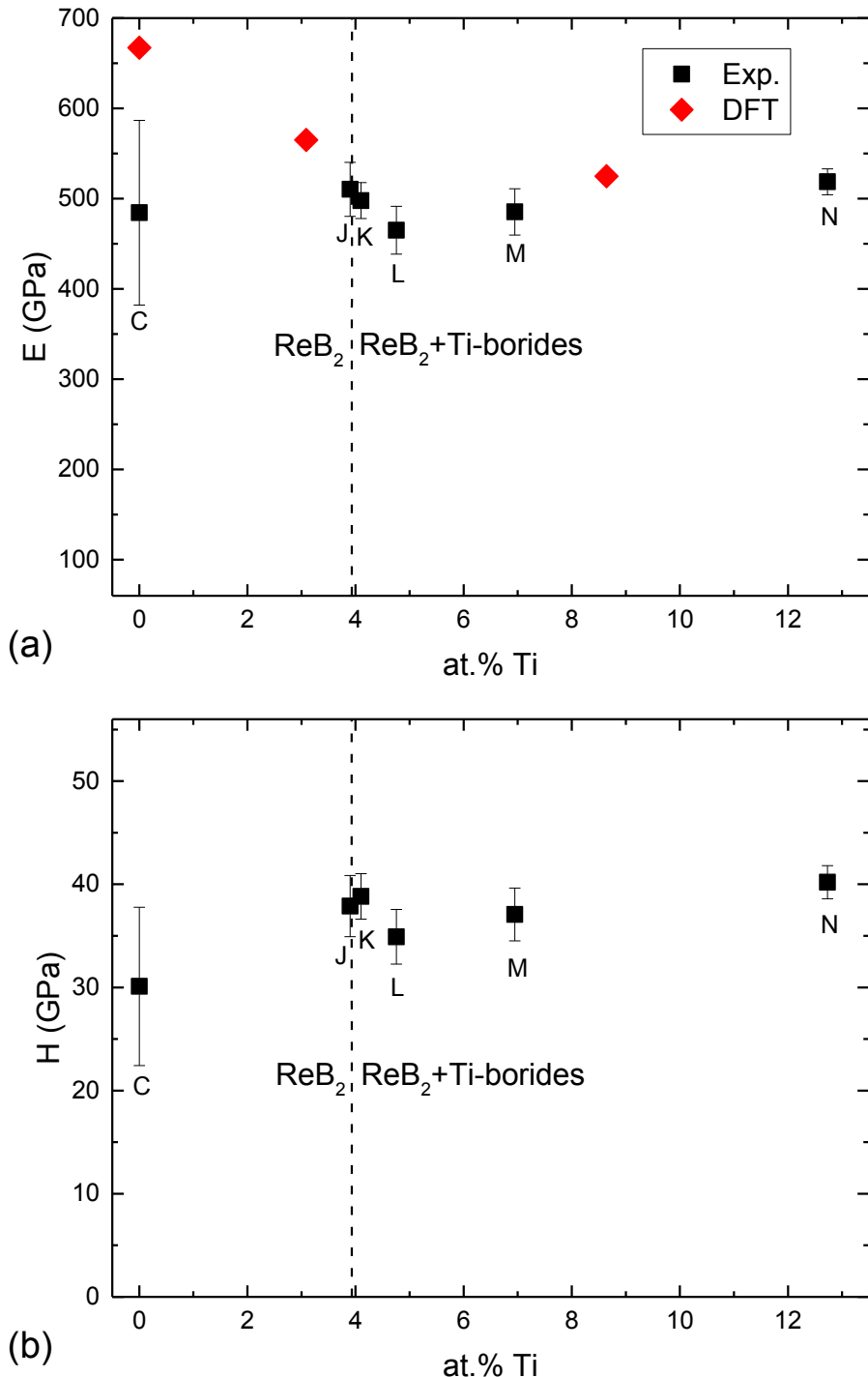


Figure 3.10: a) Measured and calculated elastic modulus, E , and b) measured hardness, H , of Ti-alloyed samples as a function of Ti concentration. The dashed line indicates the concentration at which secondary phases were detected by XRD.

concentration, N, exhibits almost no visible surface asperities (at the given magnification). Accordingly, the high hardness and low standard errors in both E and H can be attributed to the smooth and presumably dense microstructure of the Ti-alloyed films.

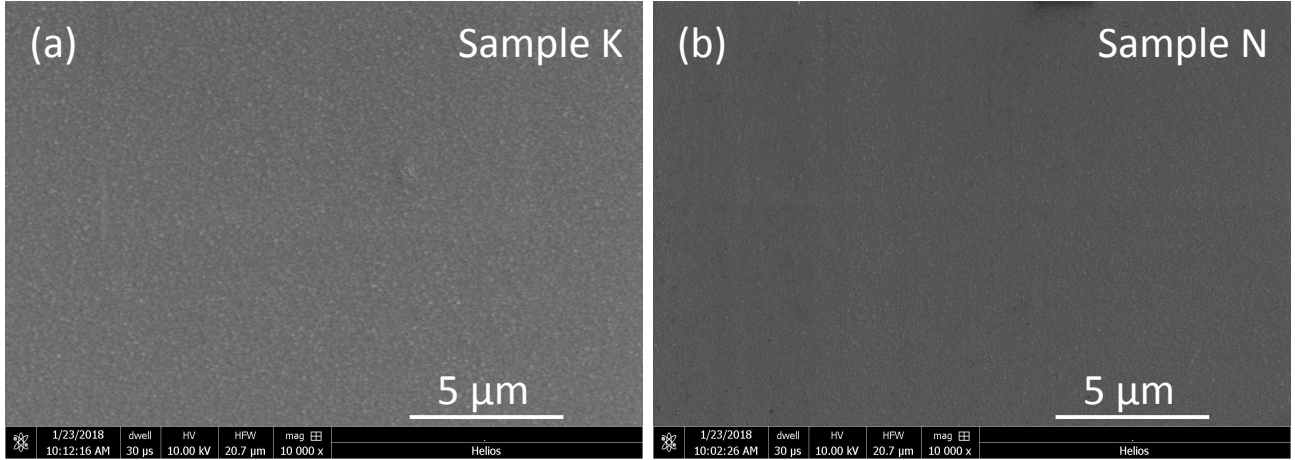


Figure 3.11: SEM overview images of the Ti-alloyed Re-B films (a) K and (b) N, deposited on MgO (001) at 900°C.

Nanoindentation data shows that unalloyed ReB_2 samples synthesized in this study exhibit an elastic modulus of about 500 GPa and a hardness of about 30 GPa. Both quantities are lower than values predicted by DFT ($E=667$ GPa) or some other studies discussed in Section 1.1, which can be attributed to the rough, inhomogeneous, and apparently porous microstructure of the films, as observed by SEM. Upon alloying of Al, the films become even rougher and, thereby, less stiff and hard. However, one exceptionally smooth Al-alloyed sample exhibits superhardness. Ti-alloyed samples show much lower surface roughness than unalloyed or Al-alloyed ones and no indication of porosity which is likely to be the reason for the high measured hardness. Consequently, both alloying strategies can yield in superhard coatings with potentially improved chemical stability compared to unalloyed ReB_2 coatings.

3.4 Chemical stability of Re-B and Al/Ti-alloyed Re-B films

Re-B films

Formation of a liquid layer on ReB_2 samples within a few months was previously reported [33, 42] (cf. Section 1.1). Orlovskaya et al. suggested that hygroscopic perrhenic acid and boric acid are formed, which further absorb water from air, thereby corroding the bulk material. However, they did not provide experimental data to support this hypothesis. The catalytic activity of perrhenic acid [69, 70] possibly speeds up the corrosive reaction. Hunold's samples (reviewed in Section 1.2)

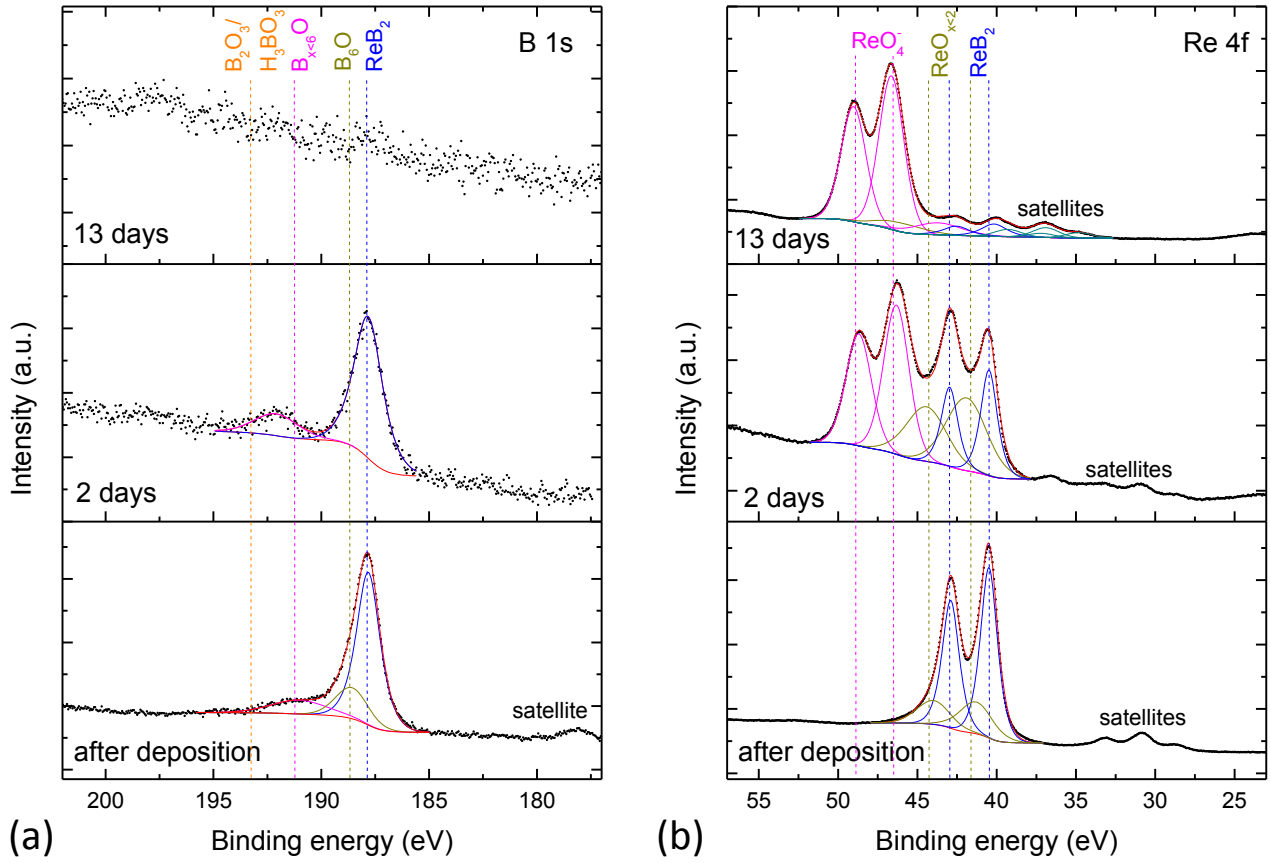


Figure 3.12: XPS scans of the (a) B 1s and (b) Re 4f transitions after different air exposure durations of a ReB_2 film. The position of the components fitted to the spectra is indicated by drop-lines.

became less reflective after a few days in air and showed formation of a liquid layer after several weeks as well. An attempt to wash off this layer on one of Hunold's samples with deionized water resulted in the entire thin film being washed off the substrate (no Re or B were detected by TOF-ERDA), probably due to the corrosive reaction having proceeded along grain boundaries throughout the entire film.

In the following, the chemical stability of ReB_2 in air will be discussed based on XPS data. The investigated sample's composition was not measured by EDX because it was mounted into the XPS system immediately after the deposition; however, a sample on a symmetry-equivalent position in the same homogenous (rotating) deposition exhibits a B concentration of 70.1 at.% and the ReB_2 crystal structure. High resolution XPS scans of the B 1s and Re 4f transitions after different air exposure durations are shown in Figure 3.12 (a) and (b), respectively. The bottom panels show the scans acquired right after the deposition (exposed to air for one to two minutes). The humps that

can be seen at lower binding energies next to the main signals are satellite peaks originating from the non-monochromatic AlK_α radiation. Beside the B 1s signal stemming from ReB₂ at 187.9 eV, two more components can be fitted to the scan; one that can be attributed to B₆O [71] at 188.7 eV and to a higher oxidation state (labeled as B_{x<6}O here), which is, however, not high enough in binding energy to be assigned to B₂O₃ or H₃BO₃ [71].

Beside the strong Re 4f doublet at 40.5 eV, another doublet component at higher binding energies (41.4 eV, labeled as ReO_{x<2} here) can be fitted to the Re 4f peak. It is too low in binding energy to be matched even to the lowest Re oxide (ReO₂ at 43.0(5) eV [71]). So it is unclear whether it really stems from the onset of oxidation, originates from bonds with Fe or C impurities, frequent lattice defects, or even phase impurities that were not detectable by XRD. Several of these options may simultaneously contribute to the component considering the relatively large peak broadness.

After two days in air, the intensity of the B 1s signal strongly decreased, as can be seen from the lower peak-to-background ratio. The B_{x<6}O component moved to higher binding energies, indicating its increased oxidation state, yet can still not be assigned to B₂O₃ or H₃BO₃. In the Re 4f scan, a strong new component emerges at 46.5 eV, which can be attributed to the perrhenate ion (ReO₄⁻) [70]. This ion is present in Re₂O₇, which solves in water and forms perrhenic acid [72]. After 13 days in air, the B 1s signal is completely vanished and the Re 4f signal consists almost entirely of the ReO₄⁻ component. After not even two weeks, the surface of ReB₂ is covered by several nanometers of perrhenic acid, considering that XPS depth resolution is in the order of a few nanometers and the B 1s signal is not detectable. Orlovskaya et al.'s [42] hypothesis about the formation of perrhenic acid is confirmed, while there is no evidence for the formation of boric acid. Moreover, the sample reacts with N from the air. While there is no N detected immediately after the deposition, the N concentration increases with increasing air exposure. The ability to break up molecular N₂ bonds (and possibly reduce N₂ to hydrazine, ammonia, or other N-compounds) can be seen as an indicator for an increased catalytic activity of the film surface [73].

Al-alloyed Re-B films

High resolution XPS scans of the B 1s, Re 4f, and Al 2s transitions of an Al-alloyed ReB_2 film with 3.7 at.% Al after different air exposure durations are shown in Figure 3.13 (a), (b), and (c), respectively. The Al 2s transition was used instead of the more commonly used 2p transition because the latter is convoluted with the Re 4f energy loss background. The only component in the Al 2s signal at 119.0 eV can be clearly attributed to Al_2O_3 [71]. After approximately six hours in air, only the B 1s component of $(\text{Re},\text{Al})\text{B}_2$ at 187.4 eV can be observed. Similar to the unalloyed sample, the Re 4f signal consists of the main $(\text{Re},\text{Al})\text{B}_2$ component at 40.2 eV and a smaller component at 41.0 eV that may stem from an onset of oxidation or impurity bonds, as discussed before. After three days in air, Al and B signals do not change. A small component at higher binding energy (46.0 eV, labeled as $\text{ReO}_{3<\text{x}<4}$ here) appears in the Re 4f scan, which exhibits an oxidation state between ReO_3 and ReO_4^- . After 16 days in air, this component increases only minimally from 4.2 to 5.1% of the total integrated intensity, while Al and B spectra do not change. No N is detected in this film. Initially, Re oxidizes a little while the Al_2O_3 layer is not fully evolved; nonetheless, Al_2O_3 seems to passivate the film in the long term. A sample with a higher Al concentration of 5.3 at.% (not shown here) did not display any oxidation of Re and only formation of Al_2O_3 .

Ti-alloyed Re-B films

High resolution XPS scans of the B 1s, Re 4f, and Ti 2p transitions of an Ti-alloyed Re-B film with 8.5 at.% Ti after different air exposure durations are shown in Figure 3.14 (a), (b), and (c), respectively. In this sample, secondary Ti-boride phases are already present. After approximately six hours in air, beside the main $(\text{Re},\text{Ti})\text{B}_2$ /Ti-boride component at 188.0 eV, the B 1s spectrum shows another oxidized component at 191.8 eV (again labeled as $\text{B}_{\text{x}<6}\text{O}$). The Ti 2p spectrum contains doublet components from $(\text{Re},\text{Ti})\text{B}_2$ /Ti-boride at 454.5 eV and TiO_2 at 458.8 eV [71] with similar intensities. The Re 4p $3/2$ transition is also visible at lower energies in the Ti scan but not of interest here. The Re 4f signal consists of the main $(\text{Re},\text{Ti})\text{B}_2$ /Ti-boride component at 40.7 eV, as well as of the previously described smaller component at 41.8 eV and the $\text{ReO}_{3<\text{x}<4}$ oxidized state at 46.1 eV. All three spectra show continued oxidation over the course

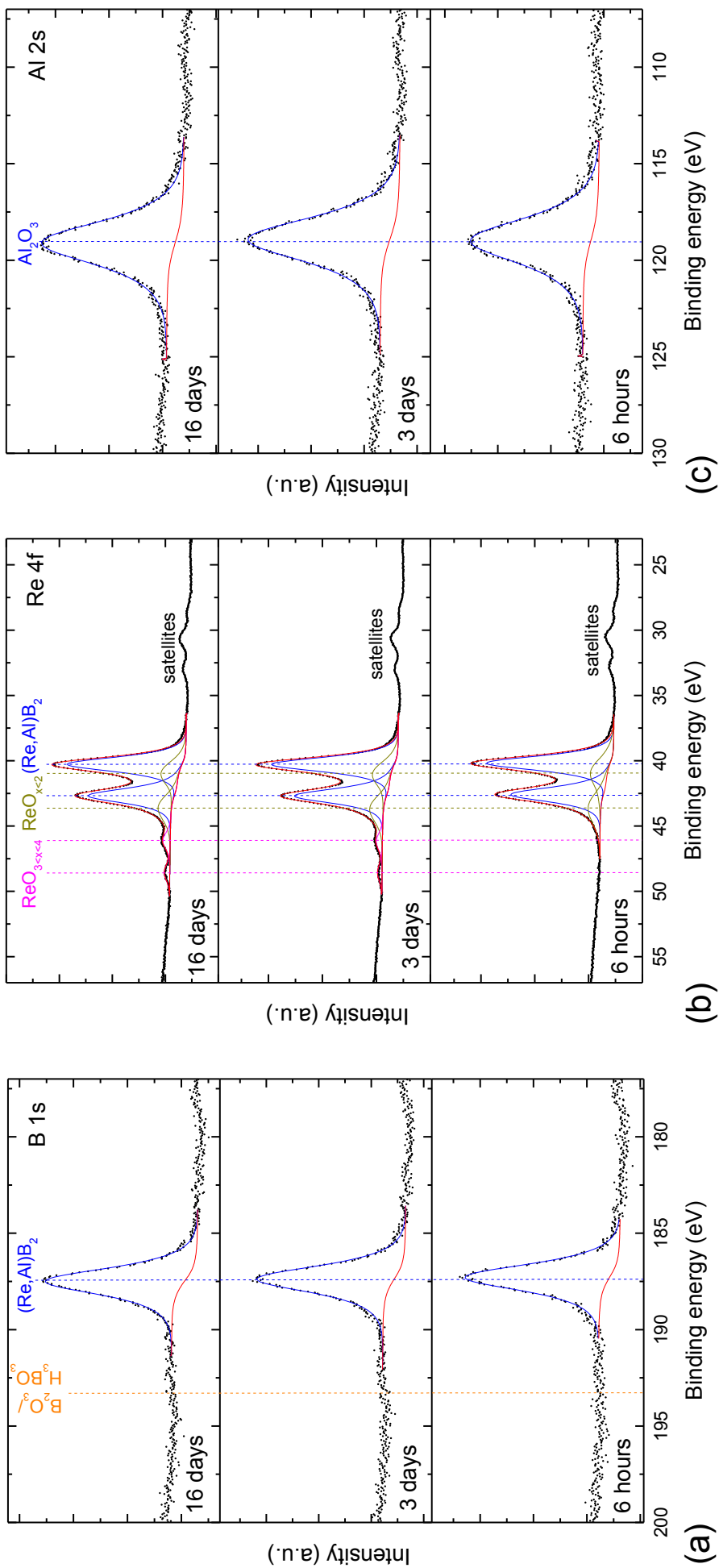


Figure 3.13: XPS scans of the (a) B 1s, (b) Re 4f, and (c) Al 2s transitions after different air exposure durations of an Al-alloyed ReB_2 sample with 3.7 at.-% Al. The position of the components fitted to the spectra is indicated by drop-lines.

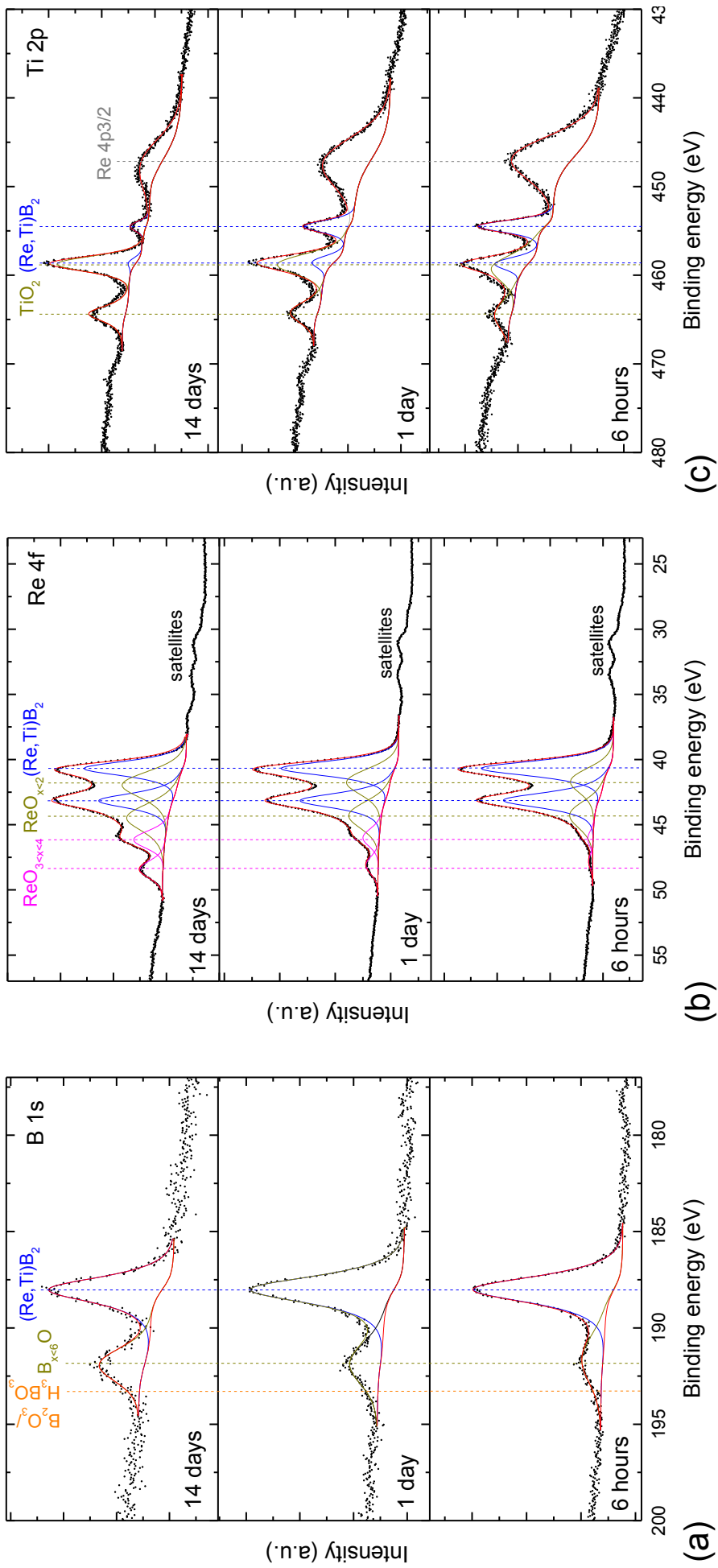


Figure 3.14: XPS scans of the (a) B 1s, (b) Re 4f, and (c) Ti 2p transitions after different air exposure durations of a Ti-alloyed ReB_2 sample with 8.5 at.% Ti. The position of the components fitted to the spectra is indicated by drop-lines.

of 14 days. Moreover, there is an increasing amount of N detected with increasing air exposure duration, as for the unalloyed sample. For samples with lower Ti concentration (not shown), the oxidation proceeds more rapidly. Alloying of Ti slows down the oxidation of Re, compared to the unalloyed sample, yet it does not seem to ensure the primary formation of a passivating TiO_2 layer at the largest considered Ti concentration of 8.5 at.%. Hence, the film may fully corrode eventually.

Analysis of surface chemical states via XPS reveals how unalloyed and alloyed ReB_2 films react in humid air. Unalloyed ReB_2 quickly forms perrhenic acid, which apparently infiltrates grain boundaries and, thereby, corrodes the entire coating within a few months. Ti-alloyed samples show formation of TiO_2 which slows down the corrosive reaction, but does not seem to achieve full passivation. Alloying of Al, on the contrary, results in the formation of a passivating Al_2O_3 layer that prevents a corrosive reaction already at an Al concentration of 3.7 at.%. This is very close to the composition of the superhard Al-alloyed sample (F, 3.5 at.% Al) discussed in Section 3.3. In conclusion, it is possible to synthesize a superhard and chemically stable $(\text{Re},\text{Al})\text{B}_2$ by magnetron sputtering.

4. Conclusions

A hybrid RF-DC magnetron sputtering process (RF on B targets and DC on metal targets) was utilized to synthesize unalloyed as well as Al/Ti-alloyed Re-B films. It was shown that it is possible to grow (X-ray) phase-pure ReB_2 films in the as-deposited state between 500 and 900°C over a wide composition range of about 55 to 75 at.% B. The successful deposition of ReB_2 in the RF-DC process, in contrast to the pulsed DC process, can be rationalized by the higher ion energy flux-to-deposition flux ratio, enabling formation of the equilibrium phase. It was shown that C impurities (8 at.%) do not favor the formation of other Re-B phases (Re_7B_3 , Re_4B_4) over ReB_2 , based on calculated energies of formation.

The mechanical properties of the films were measured by nanoindentation. ReB_2 samples exhibit an elastic modulus of about 500 GPa and a hardness of about 30 GPa, which is lower than

values predicted by DFT ($E=667$ GPa) and from other studies (literature experimental average $H=38$ GPa). These lower values can be rationalized by the rough, inhomogeneous, and apparently porous microstructure of the films, as observed by SEM and confocal laser microscopy. The chemical reactions of the films in air were investigated by XPS. ReB_2 films form perrhenic acid, which apparently infiltrates grain boundaries and corrodes the entire coating within a few months.

It is suggested that alloying Ti and Al to ReB_2 may result in phase mixtures (ReB_2 and Ti-borides) or solid solutions (Re substituted by up to 14 at.% Al), respectively, based on calculated energies of formation. Experimental results show that alloying of Ti results in the formation of Ti-borides above a concentration of 3.9 at.% Ti, whereas Al can be alloyed into ReB_2 films without formation of other phases up to a concentration of 13.6 at.% Al, which agrees excellently with predictions.

The films show much lower surface roughness than the unalloyed films and no indication of porosity upon Ti-alloying, which yields E and H up to 519 and 40 GPa (12.7 at.% Ti), respectively. The films become rougher and, hence, less stiff and hard upon Al-alloying. However, one exceptionally smooth Al-alloyed sample (3.5 at.% Al) exhibits high stiffness and superhardness ($E=562$ GPa, $H=40$ GPa). Ti-alloyed films form TiO_2 which slows down the corrosive reaction, but does not seem to achieve full passivation. Al-alloying, on the contrary, results in the formation of a passivating Al_2O_3 layer which prevents a corrosive reaction already at an Al concentration of 3.7 at.%.

In conclusion, this work has contributed to the understanding of phase formation and microstructural evolution in unalloyed and Al/Ti-alloyed ReB_2 films and of the effect of alloying on the films' mechanical properties and chemical stability. Thus, it was shown that superhard and chemically stable $(\text{Re},\text{Al})\text{B}_2$ coatings can be synthesized by magnetron sputtering.

5. Outlook

It would be interesting to identify the mechanism responsible for the exceptionally smooth and (presumably) dense microstructure, compared to films with similar Al concentration, of the most promising coating in this study; superhard and chemically stable $(\text{Re},\text{Al})\text{B}_2$ (sample F). A

procedure for the synthesis of dense, smooth, and homogenous coatings has to be developed towards application, as it has been shown that these microstructural properties strongly correlate with the mechanical properties of the coatings. Reduction of the deposition temperature and utilization of high plasma density techniques, such as HPPMS or RF supply on all targets, could be measures to achieve the desired microstructure. Furthermore, it is desirable to investigate such coatings on the atomic level to find out if they actually consist of a $(\text{Re},\text{Al})\text{B}_2$ solid solution, or if segregation of tissue phases at grain boundaries or other chemical modulations can be observed, e.g. by combining techniques such as transmission electron microscopy (TEM) and atom probe tomography (APT). Such investigations can also be carried out under the aspects of thermal stability and age hardening, which could further increase hardness similarly to the $\text{Ti}_{1-x}\text{Al}_x\text{N}$ system by spinodal decomposition [74] or the $(\text{Ti}_{1-x}\text{Al}_x)\text{B}_{2+\Delta}$ system by segregation of an amorphous B tissue phase [75]. It is also interesting to study how Al-alloying and the resulting formation of Al_2O_3 improves the oxidation resistance of the coatings, as it also reduces the oxidation rate of Al-alloyed TiB_2 thin films [76].

Despite the promising properties of $(\text{Re},\text{Al})\text{B}_2$ coatings, their economic viability has to be considered as well. The high cost of Re represents an obstacle towards widespread establishment in industry. Moreover, there are other superhard materials with even higher hardness, such as diamond (up to 150 GPa), cubic BN (up to 80 GPa) [77], B_6O (up to 45 GPa) [78], and cubic BC_2N (up to 75 GPa) [79], which are well known. The outstanding property of ReB_2 (or $(\text{Re},\text{Al})\text{B}_2$) is its electrical conductivity, which the afore mentioned materials do not exhibit. There are, however, reports about over-stoichiometric $\text{TiB}_{2.4}$ coatings with columnar TiB_2 grains surrounded by an amorphous B tissue phase that display superhardness (ca. 60 GPa) [80] and are most likely electrically conductive at a lower cost. Further research on ReB_2 -based coatings will have to show if this interesting material system has a chance to become rooted in industrial niche applications.

6. Acknowledgments

Special thanks goes to the Chair of Materials Chemistry, Prof. Dr. Jochen M. Schneider, and Dr. Stanislav Mráz for the excellent supervision of this work. I also thank Sandipan Sen for his help

in operating the FIB and acquiring the SEM images, Dr. Marcus Hans and Dr. Daniel Primetzhofer for performing the TOF-ERDA measurements, as well as Dr. Oliver Hunold for communicating his preliminary work to me in detail. For help with experiments, I want to thank Anna Lena Ravensburg, Simon Evertz, Markus Momma, and Damian Holzapfel and for fruitful discussions, I want to thank Dr. An-Ni Wang, Dr. Denis Music, Dr. Oliver Hunold, Philipp Keuter, Maciej Kaplan, and Bastian Stelzer. Computational resources provided by the RWTH Aachen University IT Centre (grant thes0334) and the Jülich-Aachen Research Alliance (JARA) (grant jara0151) are acknowledged.

As this work represents the end of my B.Sc. and M.Sc. studies, I want to thank the people who have supervised, guided, and supported me during my work as a student research assistant or in research internships during the past five years and who have, thereby, contributed to my love and dedication for science: Prof. Dr. Jochen M. Schneider, Dr. Denis Music, Dr. Oliver Hunold, Prof. Dr. Björgvin Hjörvarsson, Dr. Heikki Palonen, Bastian Stelzer, Philipp Keuter, Dr. Stanislav Mráz, and all the other amazing people from the RWTH Aachen Materials Chemistry and Uppsala University Materials Physics groups. I had a great time with all of you. Finally, I want to thank my friends, Anni, Lukas, Saaqib, Maciej, Suna, Úschi, Lana, Miranda, Jinyun, and others for their support during these rather stressful six months of my thesis, for reminding me that there is a life outside of the lab, that I should get some sleep occasionally, and that frozen pizza is not a real meal.

7. Declaration of originality

I, Pascal Bliem, confirm that unless stated otherwise, this work is the result of my own efforts. These efforts include the originality of written works as well as diagrams or similar pictorial material and results. Where material is drawn from elsewhere, references are included.

(Pascal Bliem)

8. References

- [1] Chung, H.-Y., Weinberger, M. B., Levine, J. B., Kavner, A., Yang, J.-M., Tolbert, S. H., and Kaner, R. B. *Science* **316**(5823), 436–439 (2007).
- [2] Portnoi, K. I. and Romashov, V. M. *Soviet Powder Metallurgy and Metal Ceramics* **7**(2), 112–114 Feb (1968).
- [3] Zavalij, P., Mykhalenko, S., and Kuz'ma, Y. *Journal of Alloys and Compounds* **203**(Supplement C), 55 – 59 (1994).
- [4] Lue, C. S., Tao, Y. F., and Su, T. H. *Physical Review B* **78**, 033107 Jul (2008).
- [5] Levine, J. B., Nguyen, S. L., Rasool, H. I., Wright, J. A., Brown, S. E., and Kaner, R. B. *Journal of the American Chemical Society* **130**(50), 16953–16958 (2008). PMID: 19053446.
- [6] La Placa, S. J. and Post, B. *Acta Crystallographica* **15**(2), 97–99 Feb (1962).
- [7] Otani, S., Aizawa, T., and Ishizawa, Y. *Journal of Alloys and Compounds* **252**(1), L19 – L21 (1997).
- [8] Wang, Y., Zhang, J., Daemen, L. L., Lin, Z., Zhao, Y., and Wang, L. *Physical Review B* **78**, 224106 Dec (2008).
- [9] Latini, A., Rau, J. V., Ferro, D., Teghil, R., Albertini, V. R., and Barinov, S. M. *Chemistry of Materials* **20**(13), 4507–4511 (2008).
- [10] Koehler, M. R., Keppens, V., Sales, B. C., Jin, R., and Mandrus, D. *Journal of Physics D: Applied Physics* **42**(9), 095414 (2009).
- [11] Żogał, O. J., Fojud, Z., Herzig, P., Pietraszko, A., Lyashchenko, A. B., Jurga, S., and Paderno, V. N. *Journal of Applied Physics* **106**(3), 033514 (2009).
- [12] Pellicer-Porres, J., Segura, A., Muñoz, A., Polian, A., and Congeduti, A. *Journal of Physics: Condensed Matter* **22**(4), 045701 (2010).
- [13] Liu, X., Liu, W., He, Q., Deng, L.-W., Wang, H.-J., He, D.-W., and Li, B.-S. *Chinese Physics Letters* **28**(3), 036401 (2011).
- [14] Chrzanowska, J., Hoffman, J., Denis, P., Giżyński, M., and Mościcki, T. *Surface and Coatings Technology* **277**(Supplement C), 15 – 22 (2015).
- [15] Hao, X., Xu, Y., Wu, Z., Zhou, D., Liu, X., Cao, X., and Meng, J. *Physical Review B* **74**, 224112 Dec (2006).
- [16] Zhou, W., Wu, H., and Yildirim, T. *Physical Review B* **76**, 184113 Nov (2007).
- [17] Liang, Y. and Zhang, B. *Physical Review B* **76**, 132101 Oct (2007).
- [18] Zhang, R. F., Veprek, S., and Argon, A. S. *Applied Physics Letters* **91**(20), 201914 (2007).
- [19] Zhu, X., Li, D., and Cheng, X. *Solid State Communications* **147**(7), 301 – 304 (2008).
- [20] Peng, F., Liu, Q., Fu, H., and Yang, X. *Solid State Communications* **149**(1), 56 – 59 (2009).
- [21] Aydin, S. and Simsek, M. *Physical Review B* **80**, 134107 Oct (2009).
- [22] Liang, Y., Li, A., Zhao, J., and Zhang, W. *Modern Physics Letters B* **23**(10), 1281–1290 (2009).
- [23] Li, Y.-L., Zhong, G.-H., and Zeng, Z. *Chinese Physics B* **18**(10), 4437 (2009).
- [24] Deligoz, E., Colakoglu, K., and Ciftci, Y. O. *Chinese Physics B* **21**(10), 106301 (2012).
- [25] Li, X., Wang, Y. X., and Lo, V. *Thin Solid Films* **520**(15), 4951 – 4955 (2012).

- [26] Pan, Y., Zheng, W., Guan, W., Zhang, K., Yu, S., and Hu, X. *Computational Materials Science* **82**(Supplement C), 12 – 16 (2014).
- [27] Zhang, R. F., Legut, D., Niewa, R., Argon, A. S., and Veprek, S. *Physical Review B* **82**, 104104 Sep (2010).
- [28] Levine, J., Betts, J., Garrett, J., Guo, S., Eng, J., Migliori, A., and Kaner, R. *Acta Materialia* **58**(5), 1530 – 1535 (2010).
- [29] Chen, X.-Q., Fu, C. L., Krčmar, M., and Painter, G. S. *Physical Review Letters* **100**, 196403 May (2008).
- [30] Qin, J., He, D., Wang, J., Fang, L., Lei, L., Li, Y., Hu, J., Kou, Z., and Bi, Y. *Advanced Materials* **20**(24), 4780–4783 (2008).
- [31] Kavner, A., Armentrout, M. M., Rainey, E. S. G., Xie, M., Weaver, B. E., Tolbert, S. H., and Kaner, R. B. *Journal of Applied Physics* **110**(9), 093518 (2011).
- [32] Tkachev, S. N., Levine, J. B., Kisliuk, A., Sokolov, A. P., Guo, S., Eng, J. T., and Kaner, R. B. *Advanced Materials* **21**(42), 4284–4286 (2009).
- [33] Otani, S., Korsukova, M., and Aizawa, T. *Journal of Alloys and Compounds* **477**(1), L28 – L29 (2009).
- [34] Šimůnek, A. *Physical Review B* **80**, 060103 Aug (2009).
- [35] Lazar, P., Chen, X.-Q., and Podloucky, R. *Physical Review B* **80**, 012103 Jul (2009).
- [36] Born, M. *Nature* **157**, 582 May (1946).
- [37] Chung, H.-Y., Weinberger, M. B., Levine, J. B., Cumberland, R. W., Kavner, A., Yang, J.-M., Tolbert, S. H., and Kaner, R. B. *Science* **318** December (2007).
- [38] Dubrovinskaia, N., Dubrovinsky, L., and Solozhenko, V. L. . *Science* **318** December (2007).
- [39] Locci, A. M., Licheri, R., Orrù, R., and Cao, G. *Ceramics International* **35**(1), 397 – 400 (2009).
- [40] Meschel, S. V. and Kleppa, O. J. *Metallurgical Transactions A* **24**(4), 947–950 Apr (1993).
- [41] Gao, H., Huang, Y., and Nix, W. D. *Naturwissenschaften* **86**(11), 507–515 Nov (1999).
- [42] Orlovskaya, N., Xie, Z., Klimov, M., Heinrich, H., Restrepo, D., Blair, R., and Suryanarayana, C. *Journal of Materials Research* **26**(21), 2772–2779 (2011).
- [43] Ivanov, B. L., Wellons, M. S., and Lukehart, C. M. *Journal of the American Chemical Society* **131**(33), 11744–11750 (2009). PMID: 19642682.
- [44] Saha, R. and Nix, W. D. *Acta Materialia* **50**(1), 23 – 38 (2002).
- [45] Tian, Y., Constant, A., Lo, C. C. H., Anderegg, J. W., Russell, A. M., Snyder, J. E., and Molian, P. *Journal of Vacuum Science & Technology A: Vacuum, Surfaces, and Films* **21**(4), 1055–1063 (2003).
- [46] Ohring, M. *Materials science of thin films*. Academic press, (2001).
- [47] Mráz, S. and Schneider, J. M. *Journal of Applied Physics* **109**(2), 023512 (2011).
- [48] Amosov, A. P., Latukhin, E. I., Petrov, P. A., Amosov, E. A., Novikov, V. A., and Illarionov, A. Y. *Key Engineering Materials* **746**, 207–213 (2017).
- [49] Kresse, G. and Furthmüller, J. *Physical Review B* **54**, 11169–11186 Oct (1996).
- [50] Perdew, J. P., Burke, K., and Ernzerhof, M. *Physical Review Letters* **77**, 3865–3868 Oct (1996).

- [51] Blöchl, P. E., Jepsen, O., and Andersen, O. K. *Physical Review B* **49**, 16223–16233 Jun (1994).
- [52] Music, D., Hensling, F., Pazur, T., Bednarcik, J., Hans, M., Schnabel, V., Hostert, C., and Schneider, J. M. *Solid State Communications* **169**, 6 – 9 (2013).
- [53] Birch, F. *Phys. Rev.* **71**, 809–824 Jun (1947).
- [54] Murnaghan, F. *Proceedings of the National Academy of Sciences* **30**(9), 244–247 (1944).
- [55] Monkhorst, H. J. and Pack, J. D. *Phys. Rev. B* **13**, 5188–5192 Jun (1976).
- [56] Music, D., Takahashi, T., Vitos, L., Asker, C., Abrikosov, I. A., and Schneider, J. M. *Applied Physics Letters* **91**(19), 191904 (2007).
- [57] Fast, L., Wills, J. M., Johansson, B., and Eriksson, O. *Physical Review B* **51**, 17431–17438 Jun (1995).
- [58] Hill, R. *Journal of the Mechanics and Physics of Solids* **11**(5), 357 – 372 (1963).
- [59] Birkholz, M. *Thin film analysis by X-ray scattering*. John Wiley & Sons, (2006).
- [60] Peng, J., Ji, V., Zhang, J. M., and Seiler, W. In *Residual Stresses VII, ECRS7*, volume 524 of *Materials Science Forum*, 595–600. Trans Tech Publications, 9 (2006).
- [61] Ma, C.-H., Huang, J.-H., and Chen, H. *Thin Solid Films* **418**(2), 73 – 78 (2002).
- [62] Oliver, W. and Pharr, G. *Journal of Materials Research* **7**(6), 1564–1583 (1992).
- [63] Zhang, Y., Whitlow, H. J., Winzell, T., Bubb, I. F., Sajavaara, T., Arstila, K., and Keinonen, J. *Nuclear Instruments and Methods in Physics Research Section B: Beam Interactions with Materials and Atoms* **149**(4), 477 – 489 (1999).
- [64] Meschel, S. and Kleppa, O. *Journal of Alloys and Compounds* **227**(1), 93 – 96 (1995).
- [65] Jain, A., Ong, S. P., Hautier, G., Chen, W., Richards, W. D., Dacek, S., Cholia, S., Gunter, D., Skinner, D., Ceder, G., and Persson, K. a. *APL Materials* **1**(1), 011002 (2013).
- [66] Tsui, T. Y., Oliver, W. C., and Pharr, G. M. *Journal of Materials Research* **11**(3), 752–759 (1996).
- [67] Sebastiani, M., Bemporad, E., Carassiti, F., and Schwarzer, N. *Philosophical Magazine* **91**(7-9), 1121–1136 (2011).
- [68] Sarakinos, K., Alami, J., and Konstantinidis, S. *Surface and Coatings Technology* **204**(11), 1661 – 1684 (2010).
- [69] Nikanova, O. A., Capron, M., Fang, G., Faye, J., Mamede, A.-S., Jalowiecki-Duhamel, L., Dumeignil, F., and Seisenbaeva, G. A. *Journal of Catalysis* **279**(2), 310 – 318 (2011).
- [70] Naor, A., Eliaz, N., Burstein, L., and Gileadi, E. *Electrochemical and Solid-State Letters* **13**(12), D91–D93 (2010).
- [71] National Institute of Standards and Technology. *NIST X-ray Photoelectron Spectroscopy Database, Version 4.1*. Gaithersburg, (2012).
- [72] Beyer, H., Glemser, O., and Krebs, B. *Angewandte Chemie International Edition in English* **7**(4), 295–296 4 (1968).
- [73] Shilov, A. E. *Russian Chemical Bulletin* **52**(12), 2555–2562 Dec (2003).
- [74] Mayrhofer, P. H., Hörling, A., Karlsson, L., Sjölén, J., Larsson, T., Mitterer, C., and Hultman, L. *Applied Physics Letters* **83**(10), 2049–2051 (2003).
- [75] Mockute, A., Palisaitis, J., Alling, B., Berastegui, P., Broitman, E., Näslund, L.-., Nedfors, N., Lu, J., Jensen, J., Hultman, L., Patscheider, J., Jansson, U., Persson, P., and Rosen, J. *Scripta Materialia* **127**, 122 – 126 (2017).

- [76] Mollica, S., Sood, D., Evans, P., Noorman, J., Dytlewski, N., Brack, N., Pigram, P., and Latham, K. *Surface and Coatings Technology* **177-178**, 185 – 197 (2004). Proceedings of the 30th International Conference on Metallurgical Coatings and Thin Films.
- [77] McMillan, P. F. *Nature Materials* **1**, 19 September (2002).
- [78] He, D., Zhao, Y., Daemen, L., Qian, J., Shen, T. D., and Zerda, T. W. *Applied Physics Letters* **81**(4), 643–645 (2002).
- [79] Solozhenko, V. L., Andrault, D., Fiquet, G., Mezouar, M., and Rubie, D. C. *Applied Physics Letters* **78**(10), 1385–1387 (2001).
- [80] Mayrhofer, P. H., Mitterer, C., Wen, J. G., Greene, J. E., and Petrov, I. *Applied Physics Letters* **86**(13), 131909 (2005).

A. Appendix

A.1 DFT computational cells

This section displays images (Figures A.1, A.2, and A.3) of the supercells used for calculating energies of formation in Section 3.1 and elastic moduli in Section 3.3.

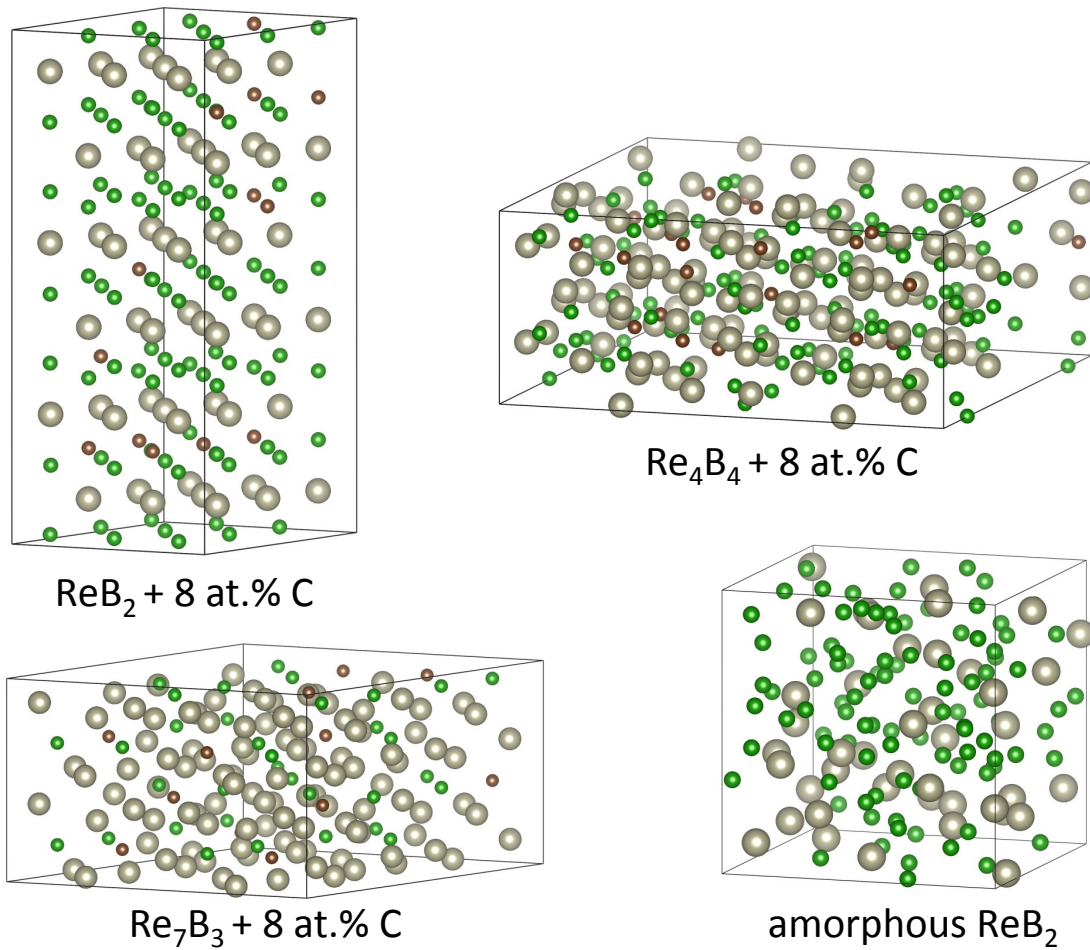
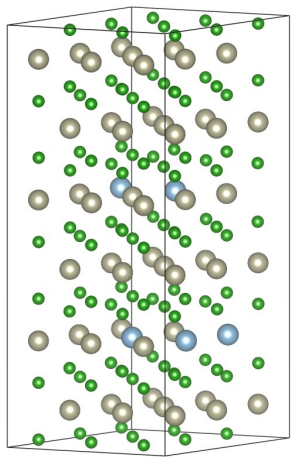
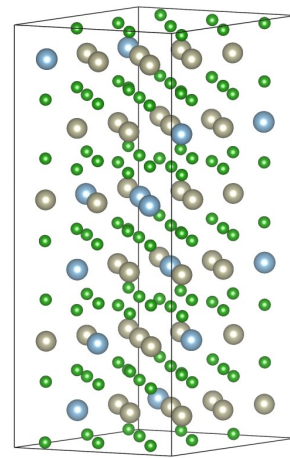


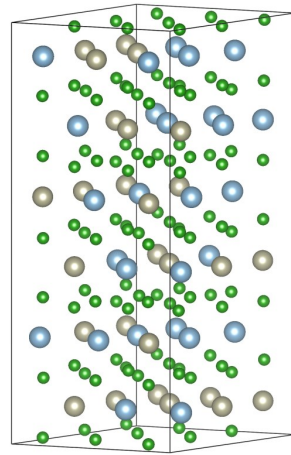
Figure A.1: Computational supercells of ReB_2 , Re_4B_4 , Re_7B_3 , each with 8 at.% B substituted by C, and amorphous ReB_2 . Re is colored gray, B green, C brown.



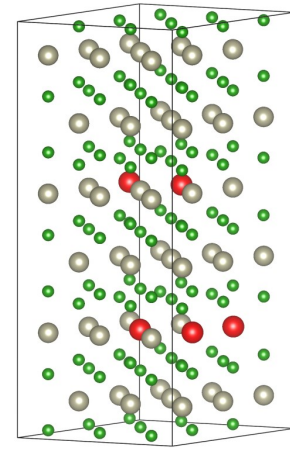
$\text{ReB}_2 + 3.1 \text{ at.\% Al}$



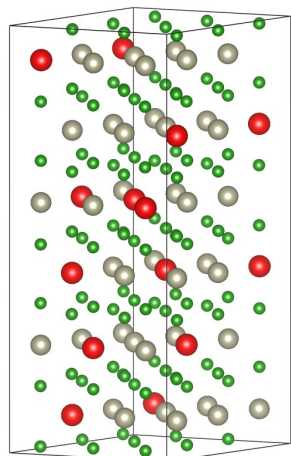
$\text{ReB}_2 + 8.3 \text{ at.\% Al}$



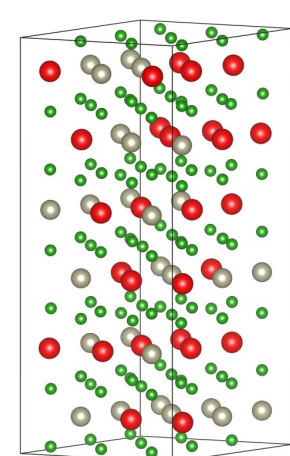
$\text{ReB}_2 + 16.7 \text{ at.\% Al}$



$\text{ReB}_2 + 3.1 \text{ at.\% Ti}$

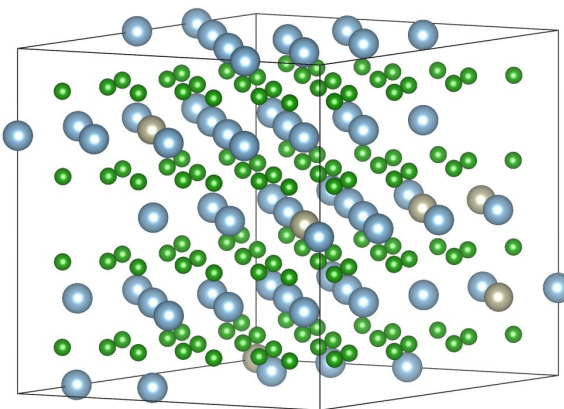


$\text{ReB}_2 + 8.3 \text{ at.\% Ti}$

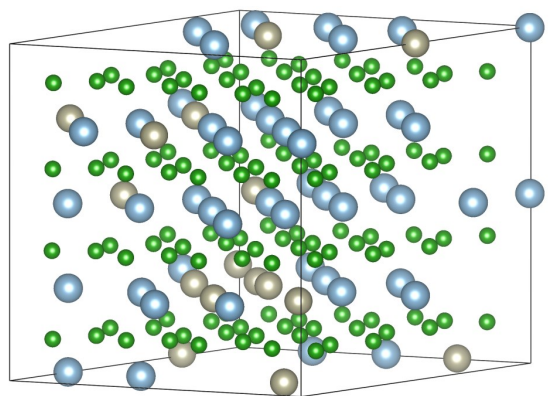


$\text{ReB}_2 + 16.7 \text{ at.\% Ti}$

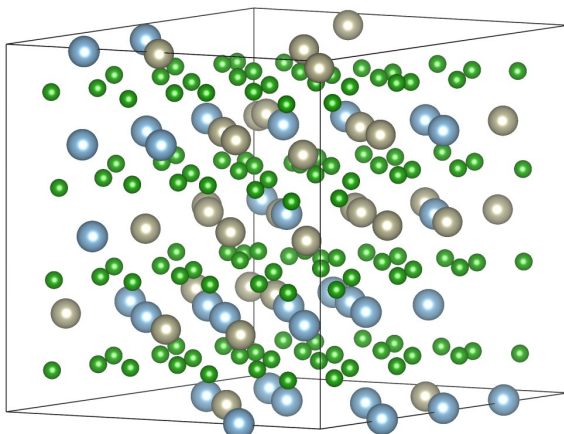
Figure A.2: Computational supercells of ReB_2 with varying concentration of Re substituted by Al or Ti. Re is colored gray, Al blue, Ti red, B green.



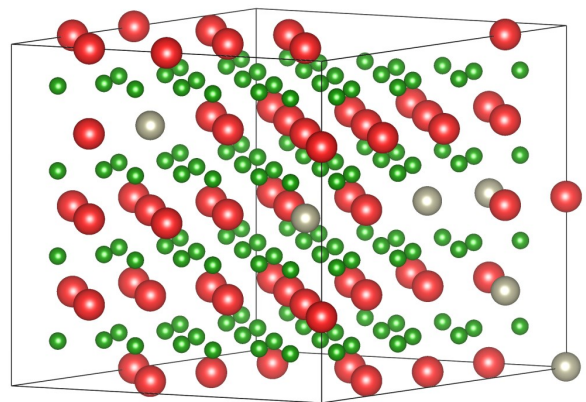
$\text{AlB}_2 + 3.1 \text{ at.\% Re}$



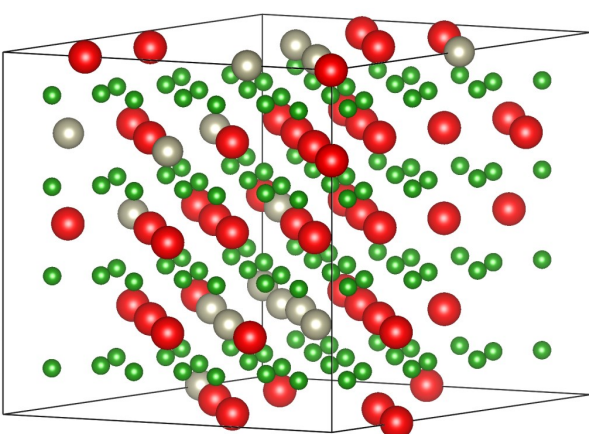
$\text{AlB}_2 + 8.3 \text{ at.\% Re}$



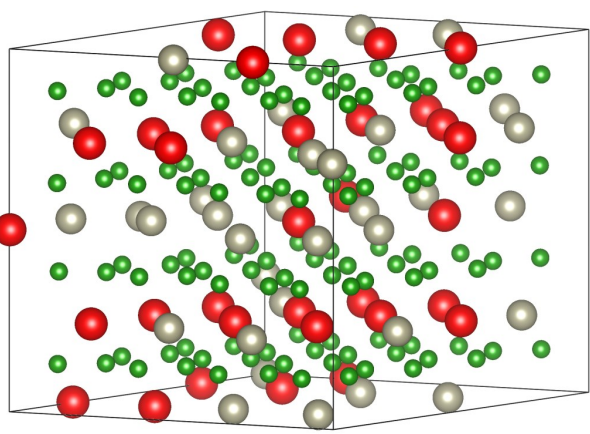
$\text{AlB}_2 + 16.7 \text{ at.\% Re}$



$\text{TiB}_2 + 3.1 \text{ at.\% Re}$



$\text{TiB}_2 + 8.3 \text{ at.\% Re}$



$\text{TiB}_2 + 16.7 \text{ at.\% Re}$

Figure A.3: Computational supercells of AlB_2 and TiB_2 with varying concentration of Al and Ti, respectively, substituted by Re. Re is colored gray, Al blue, Ti red, B green.

A.2 Phase formation raw data

This section shows the raw data (Figures A.4, A.5, A.6, A.7, A.8, A.9, A.10, A.11, A.12, A.13, A.14, A.15, A.16, A.17, A.18, and A.19) of structural (XRD) and chemical (EDX/TOF-ERDA) characterization of Re-B and Al/Ti-alloyed Re-B films which was used to compile Figures 3.3, 3.4, and 3.5 in Section 3.2.

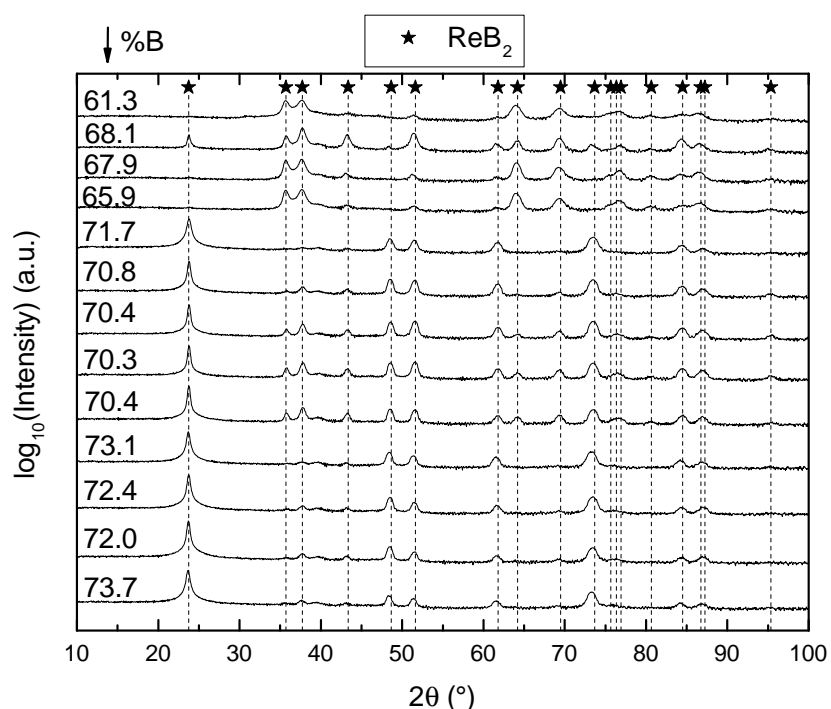


Figure A.4: Diffractograms of different areas on a Re-B combinatorial film deposited on sapphire (0001) at 900°C (Re 20 W, 2x B 149 W). The B concentration is given on the left of the diffractograms and ReB_2 peak positions are indicated by drop-lines.

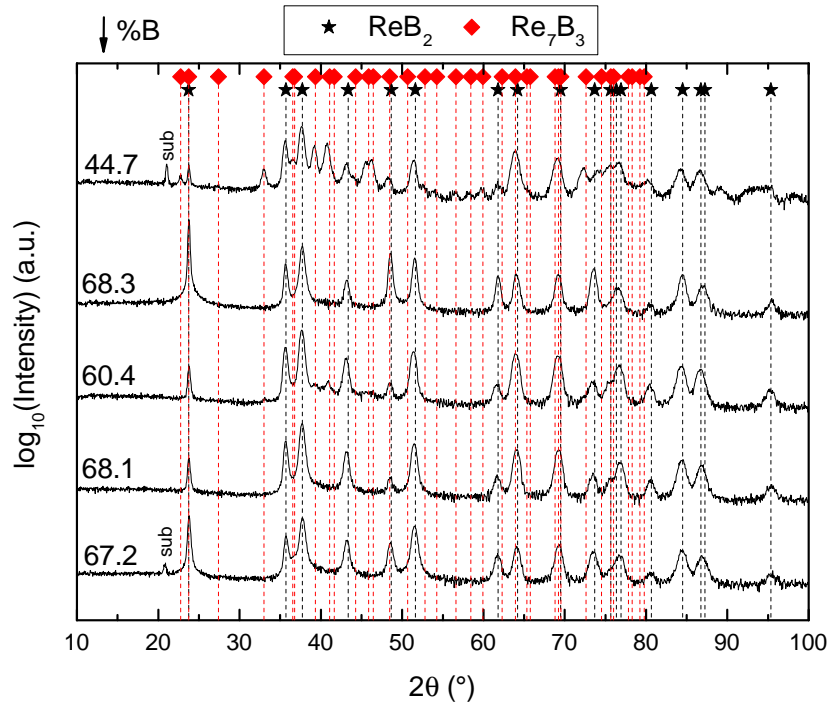


Figure A.5: Diffractograms of different areas on a Re-B combinatorial film deposited on MgO (001) at 900°C (Re 20 W, 2x B 149 W). The B concentration is given on the left of the diffractograms and ReB_2 peak positions are indicated by drop-lines.

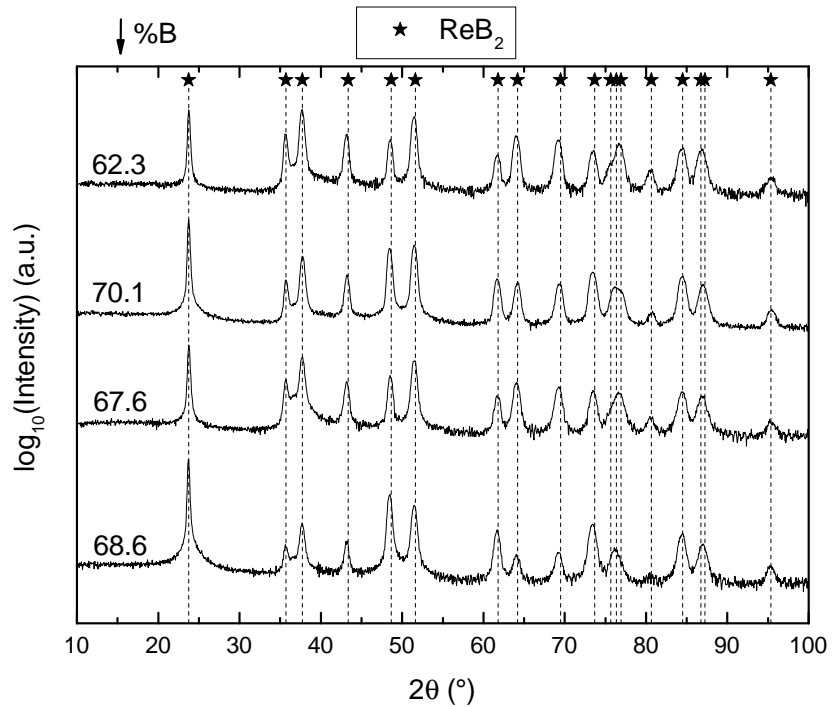


Figure A.6: Diffractograms of Re-B films from different positions on a rotating substrate holder deposited on MgO (001) at 900°C (Re 20 W, 2x B 149 W). The B concentration is given on the left of the diffractograms and ReB_2 peak positions are indicated by drop-lines.

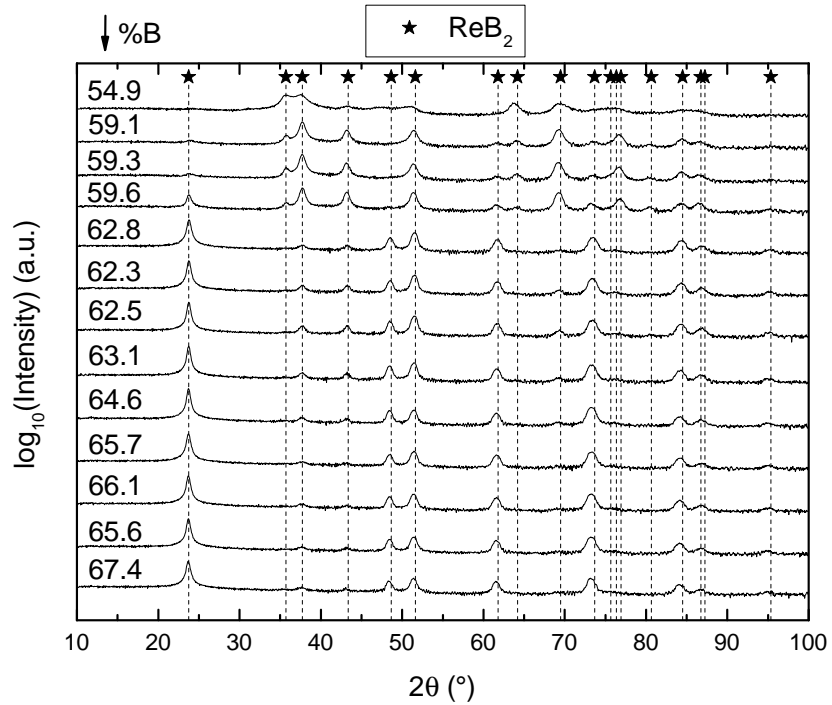


Figure A.7: Diffractograms of different areas on a Re-B combinatorial film deposited on sapphire (0001) at 700°C (Re 20 W, 2x B 149 W). The B concentration is given on the left of the diffractograms and ReB₂ peak positions are indicated by drop-lines.

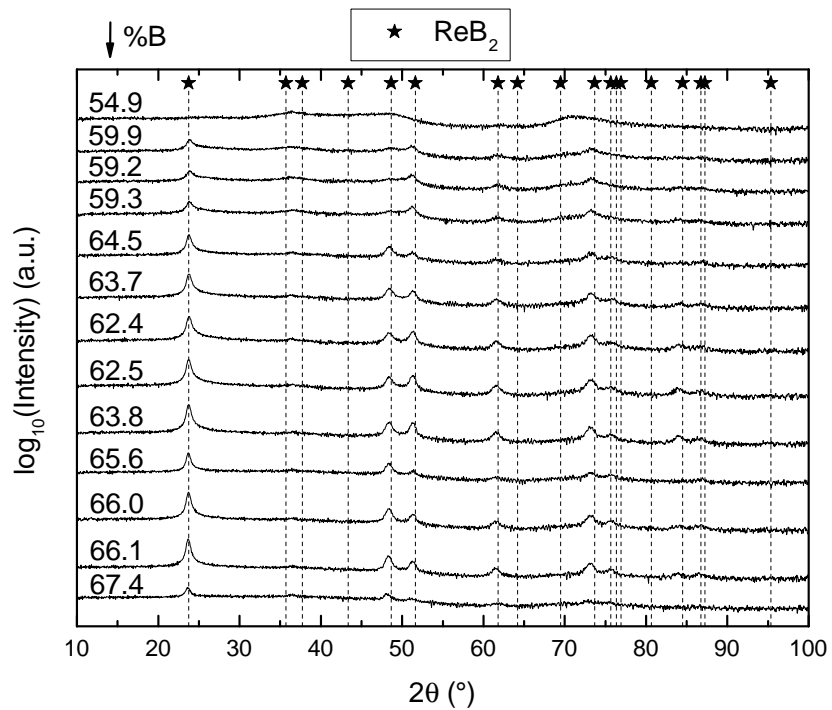


Figure A.8: Diffractograms of different areas on a Re-B combinatorial film deposited on sapphire (0001) at 500°C (Re 20 W, 2x B 149 W). The B concentration is given on the left of the diffractograms and ReB₂ peak positions are indicated by drop-lines.

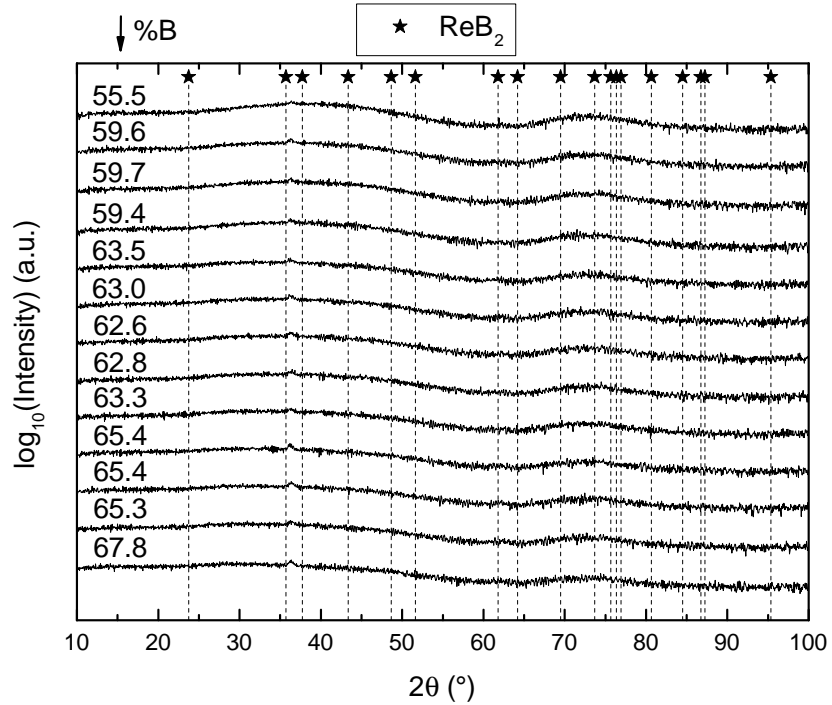


Figure A.9: Diffractograms of different areas on a Re-B combinatorial film deposited on sapphire (0001) at 300°C (Re 20 W, 2x B 149 W). The B concentration is given on the left of the diffractograms and ReB₂ peak positions are indicated by drop-lines.

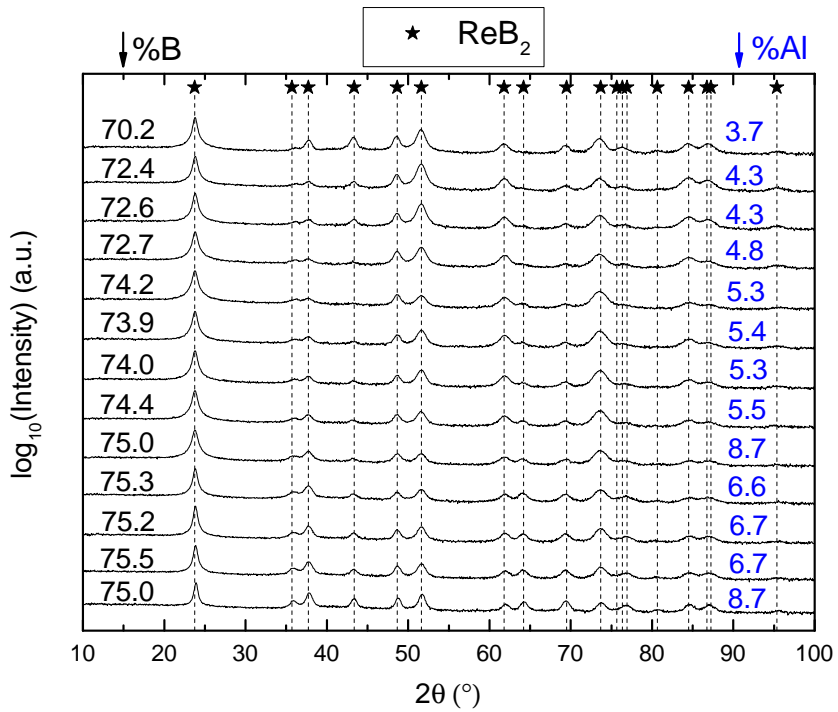


Figure A.10: Diffractograms of different areas on a Al-alloyed Re-B combinatorial film deposited on sapphire (0001) at 900°C (Re 15 W, Al 5 W, 2x B 149 W). The Al and B concentrations are given on the right and left hand side of the diffractograms, respectively, and ReB₂ peak positions are indicated by drop-lines.

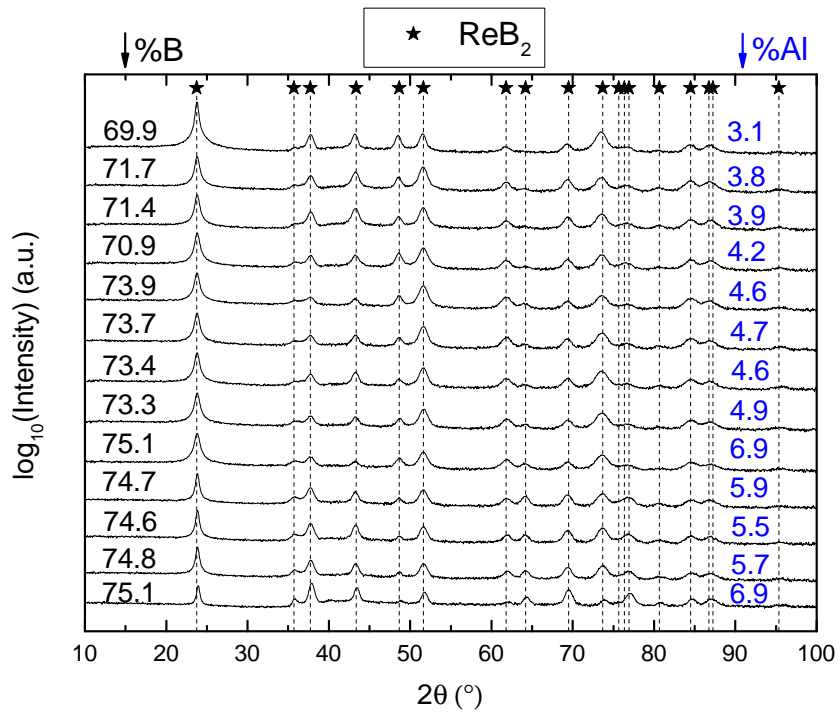


Figure A.11: Diffractograms of different areas on a Al-alloyed Re-B combinatorial film deposited on sapphire (0001) at 900°C (Re 15 W, Al 5 W, 2x B 139 W). The Al and B concentrations are given on the right and left hand side of the diffractograms, respectively, and ReB₂ peak positions are indicated by drop-lines.

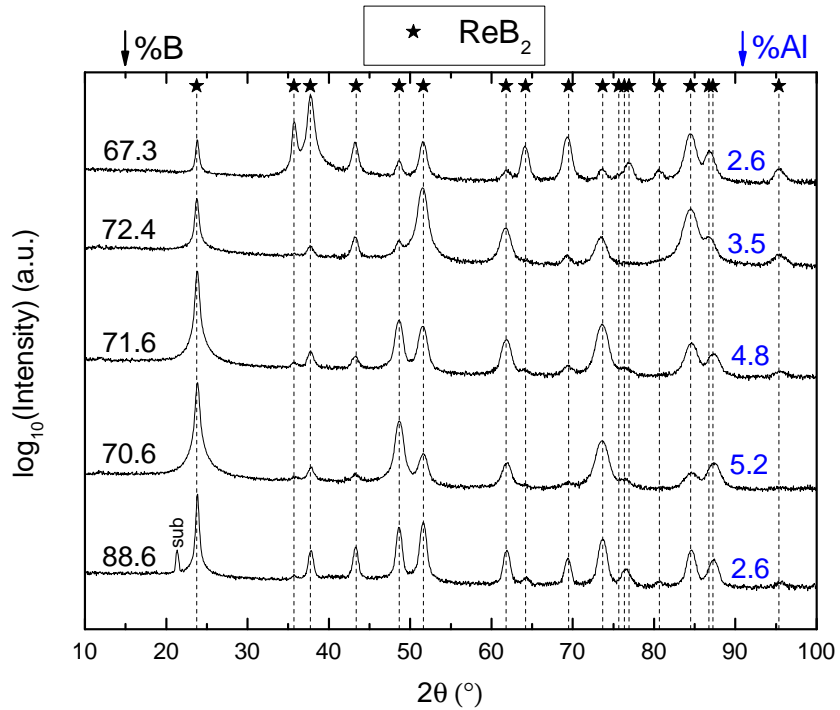


Figure A.12: Diffractograms of different areas on a Al-alloyed Re-B combinatorial film deposited on MgO (001) at 900°C (Re 20 W, Al 7 W, 2x B 149 W). The Al and B concentrations are given on the right and left hand side of the diffractograms, respectively, and ReB₂ peak positions are indicated by drop-lines.

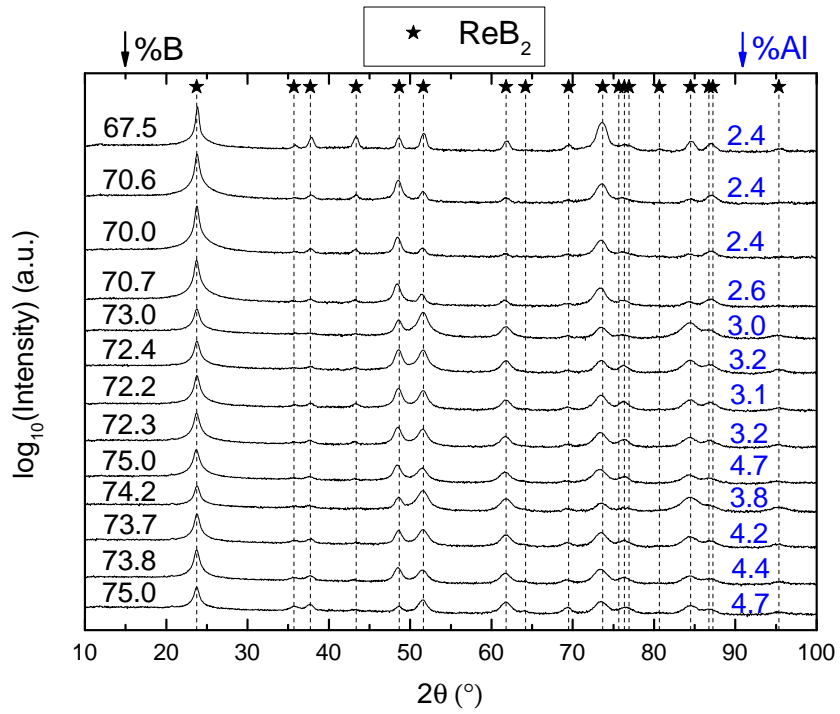


Figure A.13: Diffractograms of different areas on a Al-alloyed Re-B combinatorial film deposited on sapphire (0001) at 900°C (Re 30 W, Al 5 W, 2x B 223 W). The Al and B concentrations are given on the right and left hand side of the diffractograms, respectively, and ReB_2 peak positions are indicated by drop-lines.

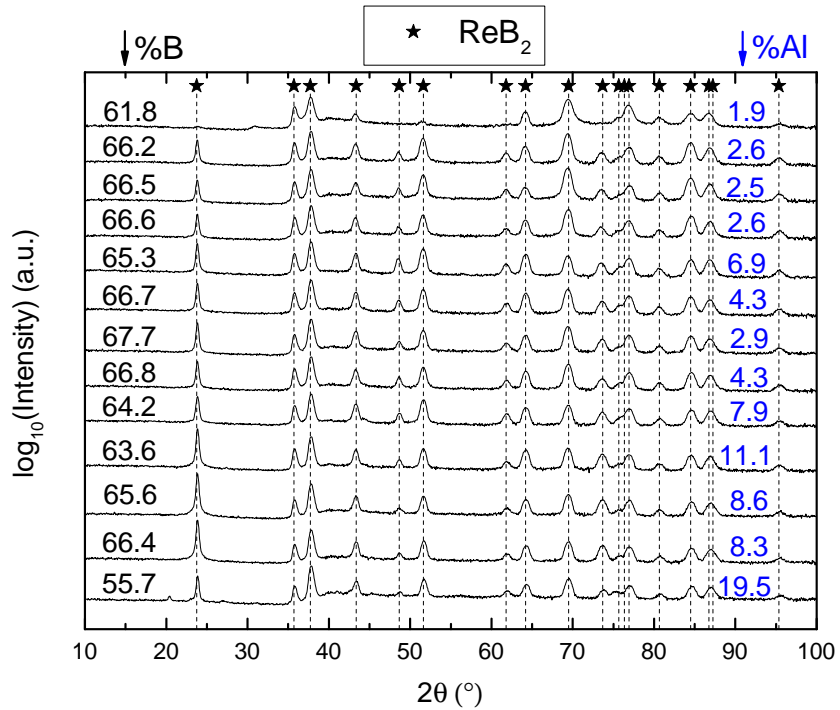


Figure A.14: Diffractograms of different areas on a Al-alloyed Re-B combinatorial film deposited on sapphire (0001) at 900°C (Re 25 W, Al 15 W, 2x B 149 W). The Al and B concentrations are given on the right and left hand side of the diffractograms, respectively, and ReB_2 peak positions are indicated by drop-lines.

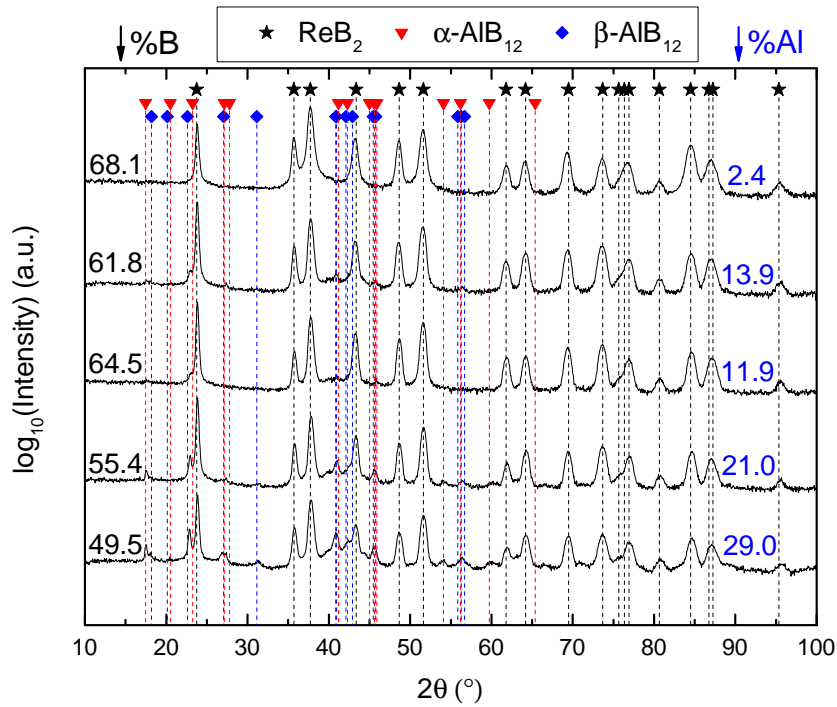


Figure A.15: Diffractograms of different areas on a Al-alloyed Re-B combinatorial film deposited on MgO (001) at 900°C (Re 20 W, Al 15 W, 2x B 148 W). The Al and B concentrations are given on the right and left hand side of the diffractograms, respectively, and ReB_2 and AlB_{12} peak positions are indicated by drop-lines.

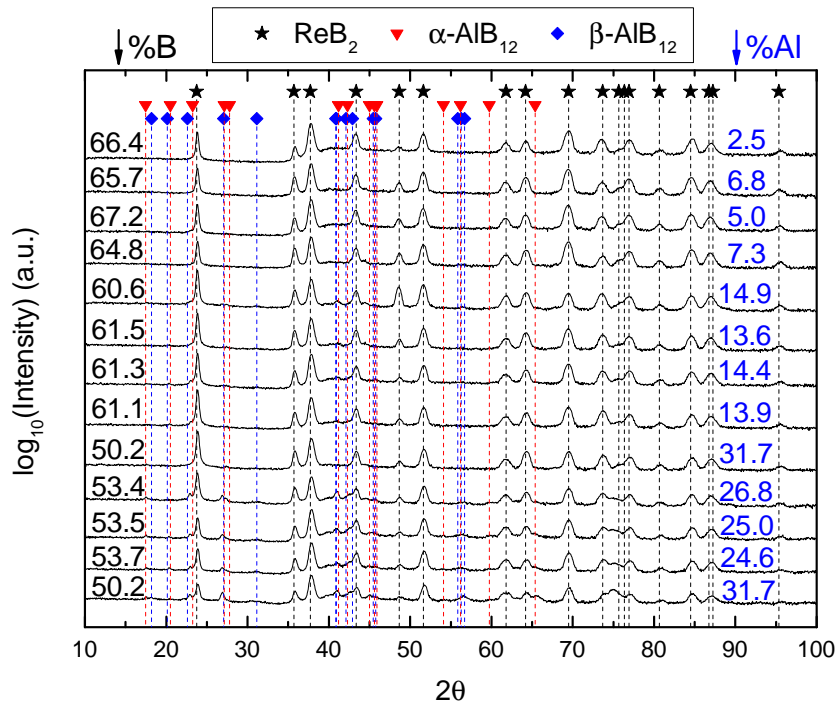


Figure A.16: Diffractograms of different areas on a Al-alloyed Re-B combinatorial film deposited on sapphire (0001) at 900°C (Re 20 W, Al 20 W, 2x B 148 W). The Al and B concentrations are given on the right and left hand side of the diffractograms, respectively, and ReB_2 and AlB_{12} peak positions are indicated by drop-lines.

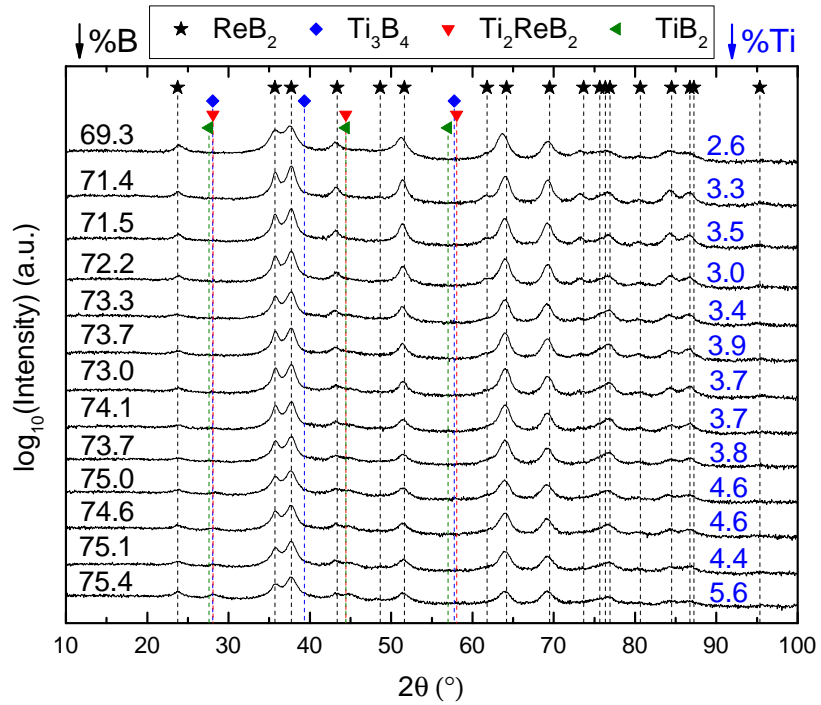


Figure A.17: Diffractograms of different areas on a Ti-alloyed Re-B combinatorial film deposited on sapphire (0001) at 900°C (Re 20 W, Ti 7 W, 2x B 149 W). The Ti and B concentrations are given on the right and left hand side of the diffractograms, respectively, and ReB_2 , Ti_3B_4 , Ti_2ReB_2 , and TiB_2 peak positions are indicated by drop-lines.

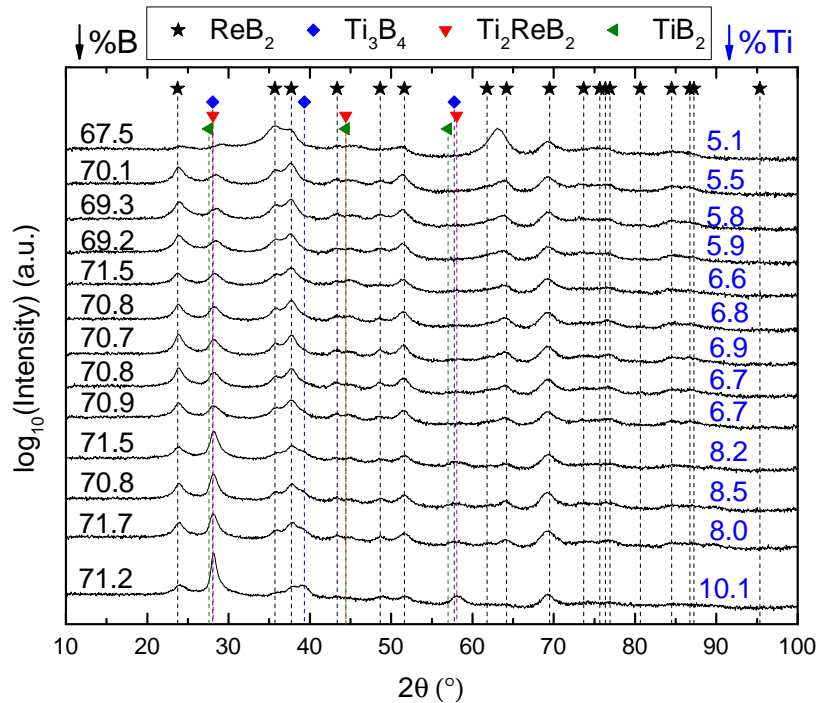


Figure A.18: Diffractograms of different areas on a Ti-alloyed Re-B combinatorial film deposited on sapphire (0001) at 900°C (Re 20 W, Ti 15 W, 2x B 149 W). The Ti and B concentrations are given on the right and left hand side of the diffractograms, respectively, and ReB_2 , Ti_3B_4 , Ti_2ReB_2 , and TiB_2 peak positions are indicated by drop-lines.

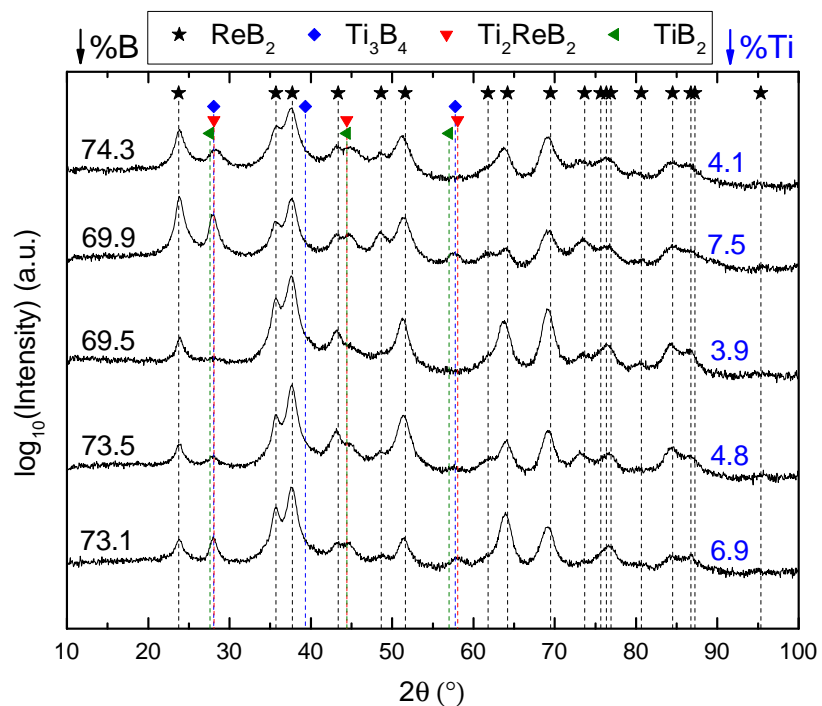


Figure A.19: Diffractograms of different areas on Ti-alloyed Re-B combinatorial films deposited on MgO (001) at 900°C (lower 3 curves: Re 20 W, Ti 10 W, 2x B 149 W; upper two curves: Re 24 W, Ti 12 W, 2x B 149 W). The Ti and B concentrations are given on the right and left hand side of the diffractograms, respectively, and ReB_2 , Ti_3B_4 , Ti_2ReB_2 , and TiB_2 peak positions are indicated by drop-lines.

A.3 XRD stress measurement raw data

This section shows the raw data (Figures A.20, A.21, A.22, A.23, A.24, A.25, A.26, A.27, A.28, A.29, A.30, A.31, and A.32) which was used to determine residual stresses in the samples utilized for mechanical characterization in Section 3.3 (cf. Tables 3.1, 3.2, and 3.3).

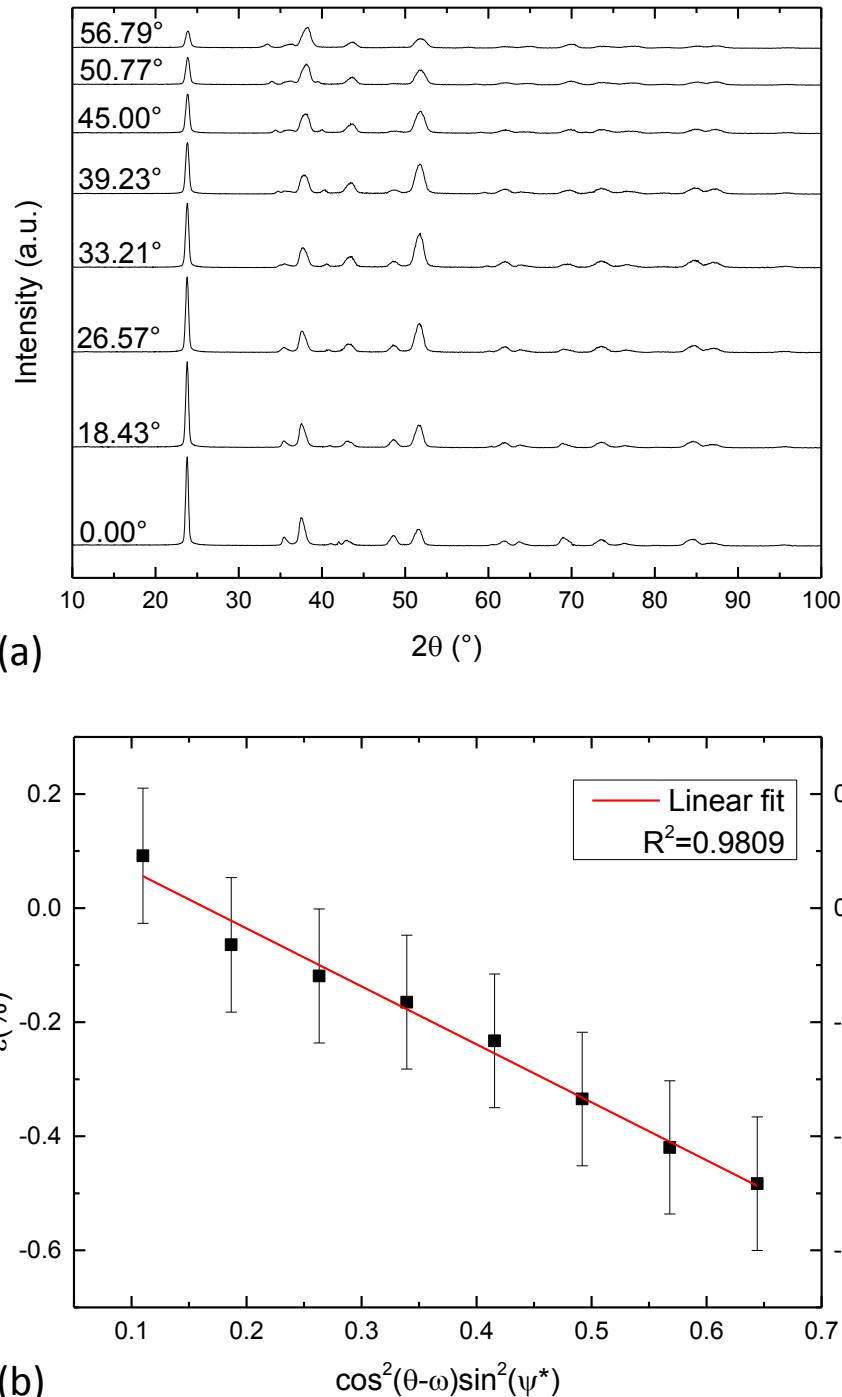
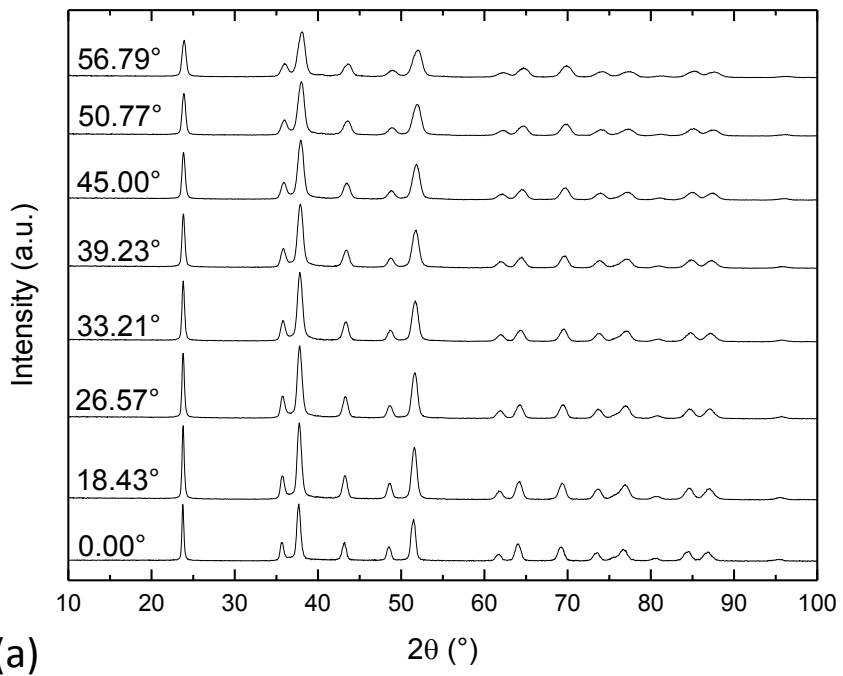
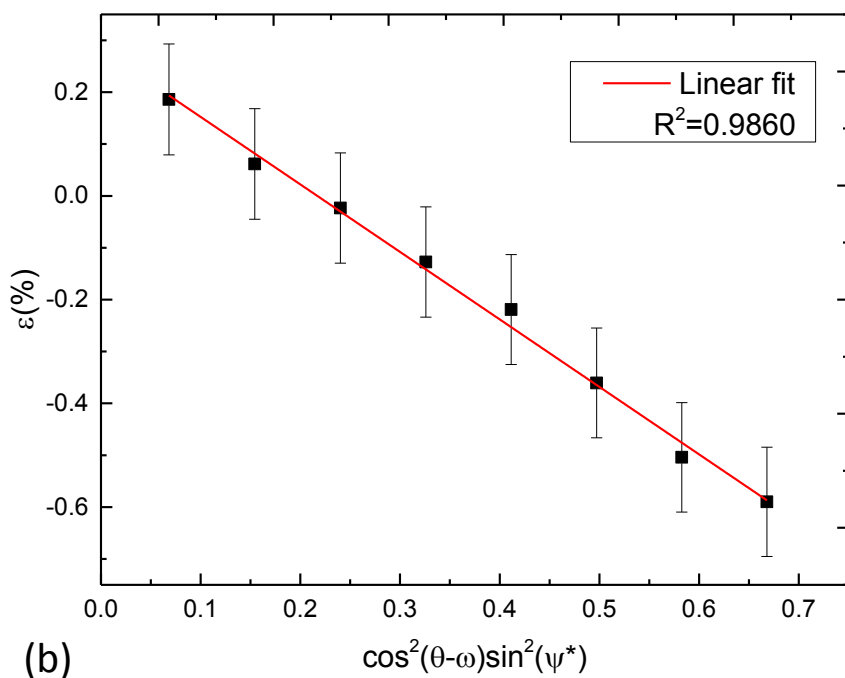


Figure A.20: (a): Diffractograms of Re-B sample B at different ψ angles (given on the left hand side of the diffractograms). (b): XRD-measured strain, ϵ , vs. $\cos^2(\theta - \omega) \sin^2 \psi^*$ plot and linear fit.

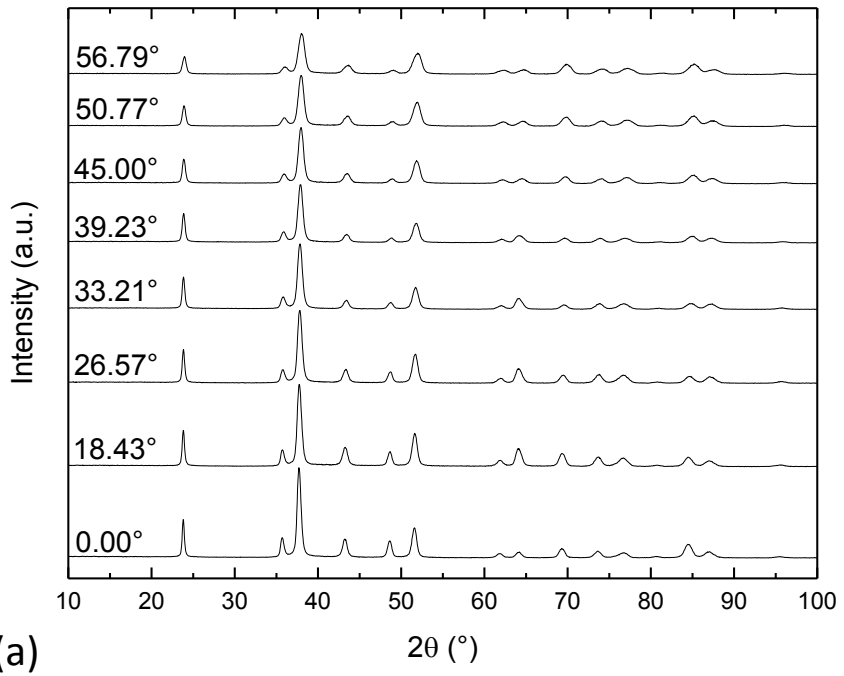


(a)

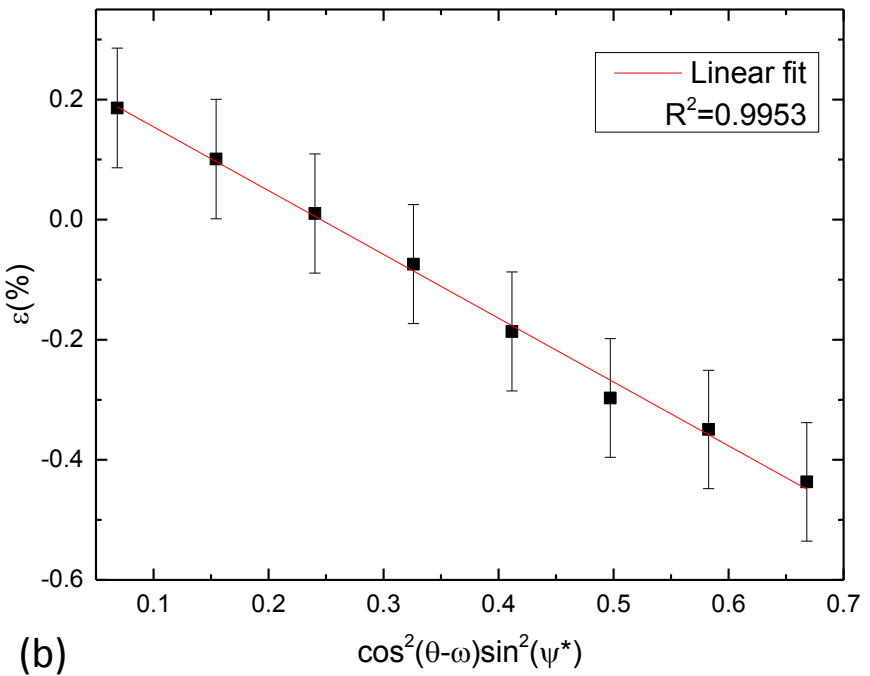


(b)

Figure A.21: (a): Diffractograms of Re-B sample C at different ψ angles (given on the left hand side of the diffractograms). (b): XRD-measured strain, ϵ , vs. $\cos^2(\theta - \omega) \sin^2 \psi^*$ plot and linear fit.



(a)



(b)

Figure A.22: (a): Diffractograms of Al-alloyed Re-B sample D at different ψ angles (given on the left hand side of the diffractograms). (b): XRD-measured strain, ϵ , vs. $\cos^2(\theta - \omega) \sin^2(\psi^*)$ plot and linear fit.

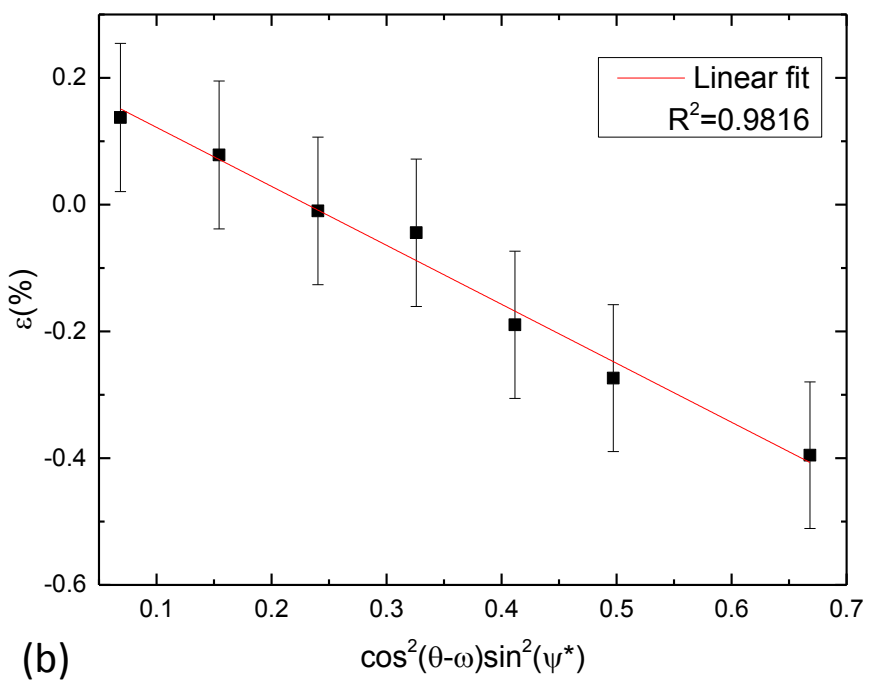
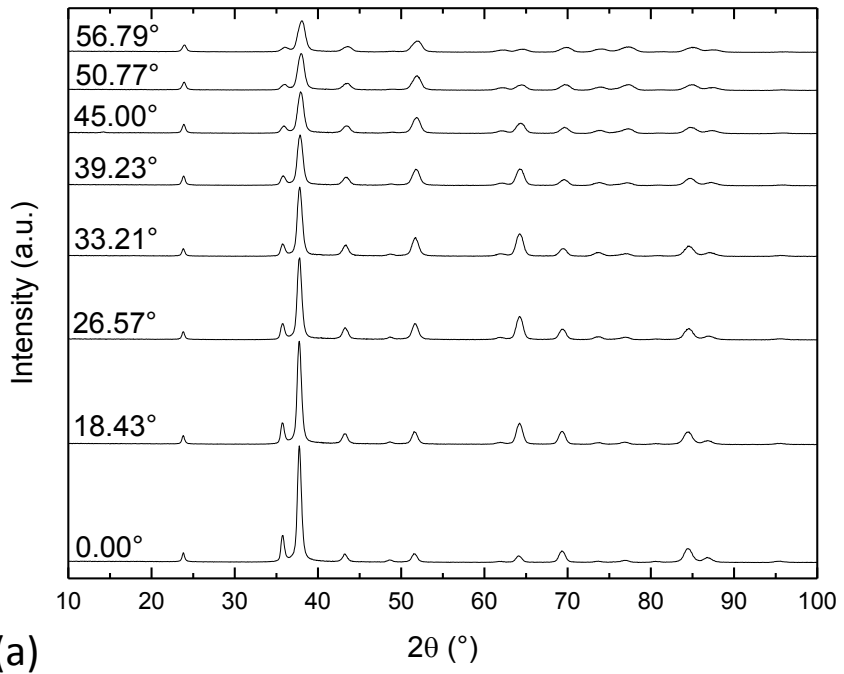
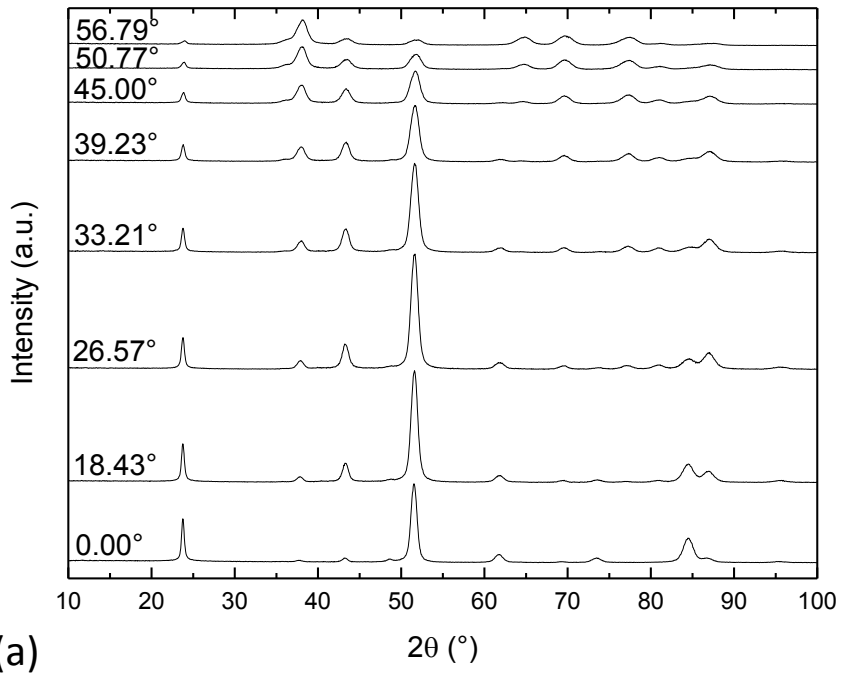


Figure A.23: (a): Diffractograms of Al-alloyed Re-B sample E at different ψ angles (given on the left hand side of the diffractograms). (b): XRD-measured strain, ϵ , vs. $\cos^2(\theta - \omega) \sin^2(\psi^*)$ plot and linear fit.



(a)

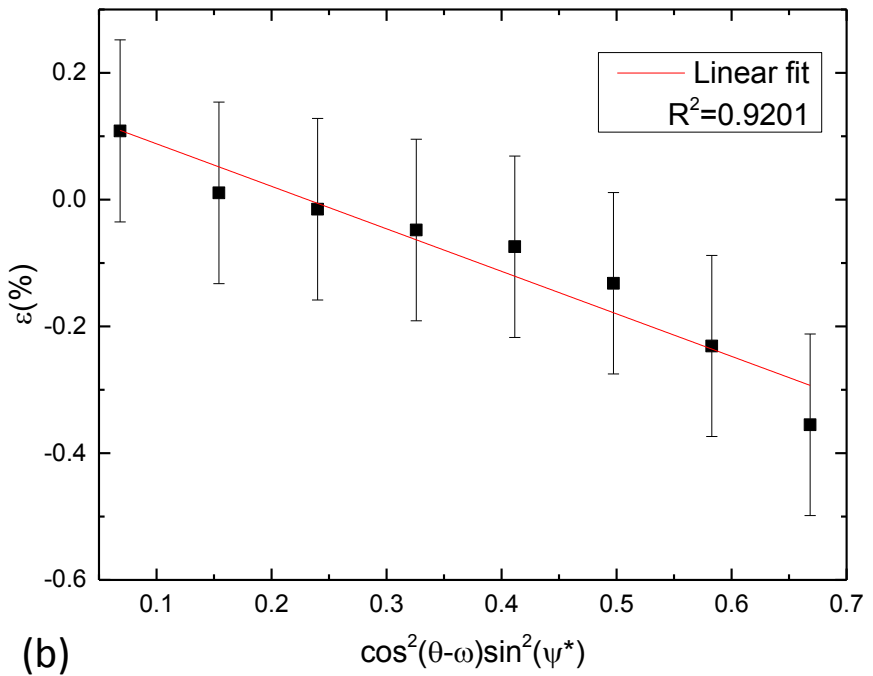


Figure A.24: (a): Diffractograms of Al-alloyed Re-B sample F at different ψ angles (given on the left hand side of the diffractograms). (b): XRD-measured strain, ϵ , vs. $\cos^2(\theta - \omega) \sin^2(\psi^*)$ plot and linear fit.

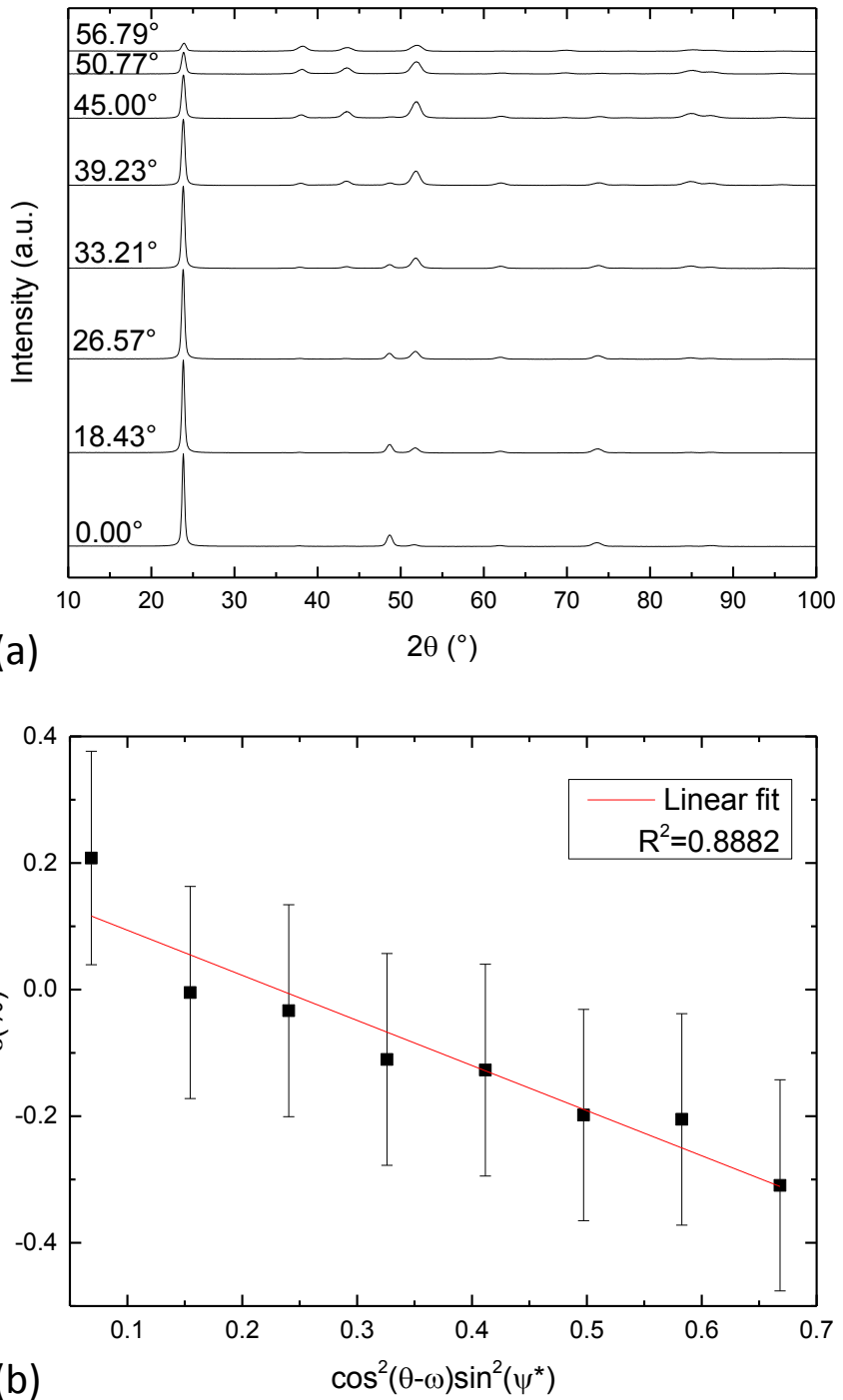
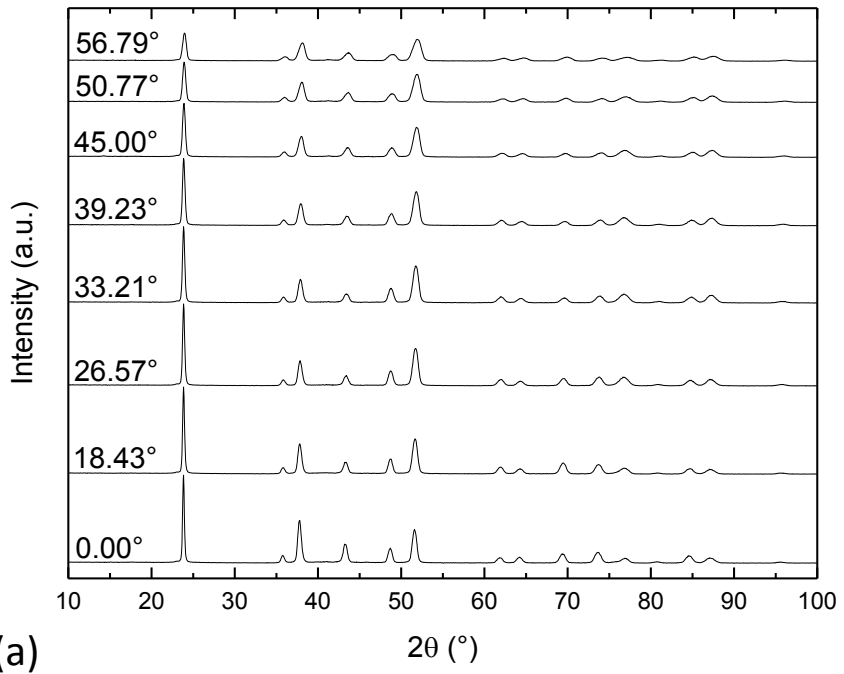
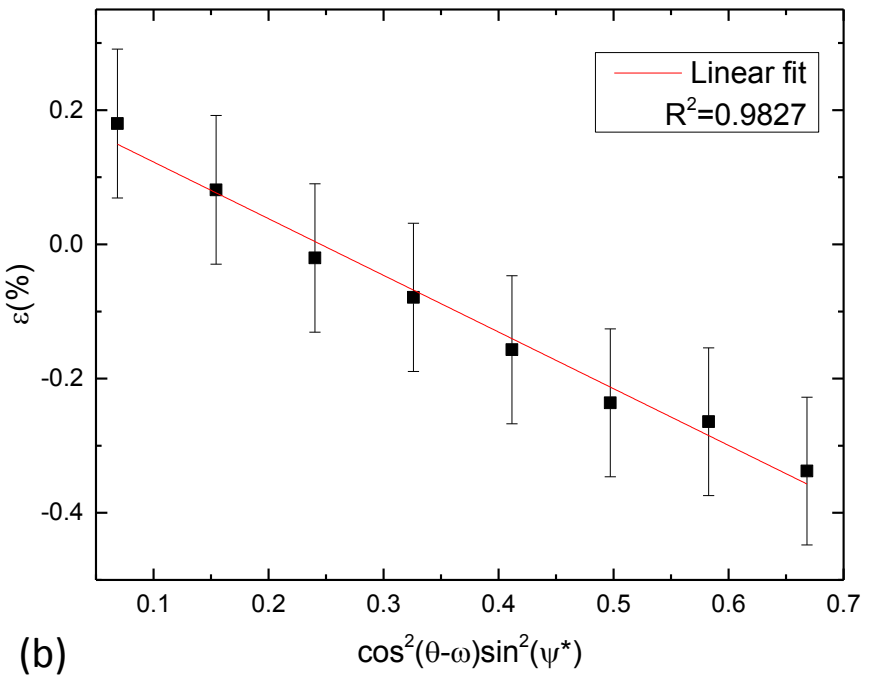


Figure A.25: (a): Diffractograms of Al-alloyed Re-B sample G at different ψ angles (given on the left hand side of the diffractograms). (b): XRD-measured strain, ϵ , vs. $\cos^2(\theta - \omega) \sin^2(\psi^*)$ plot and linear fit.

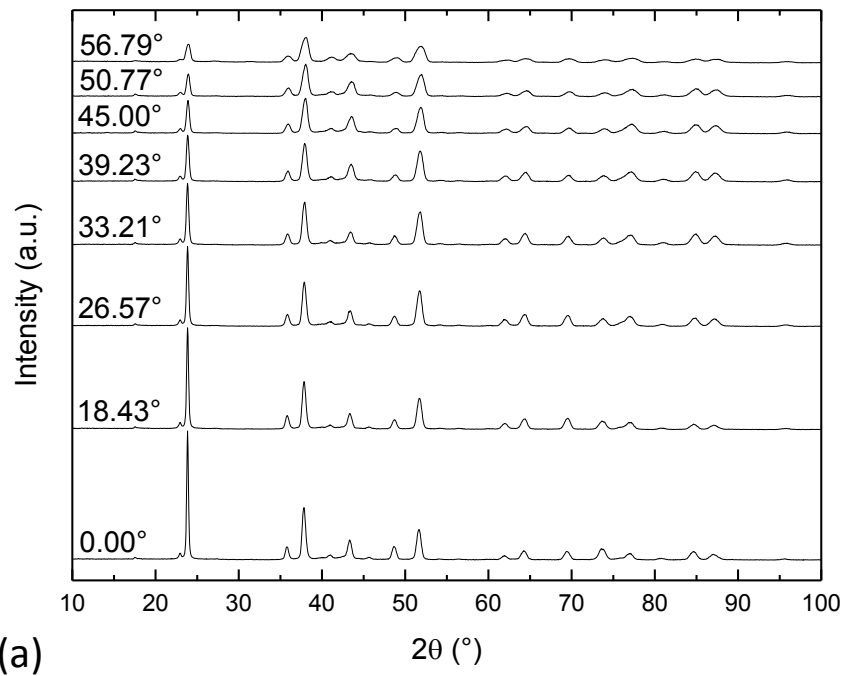


(a)

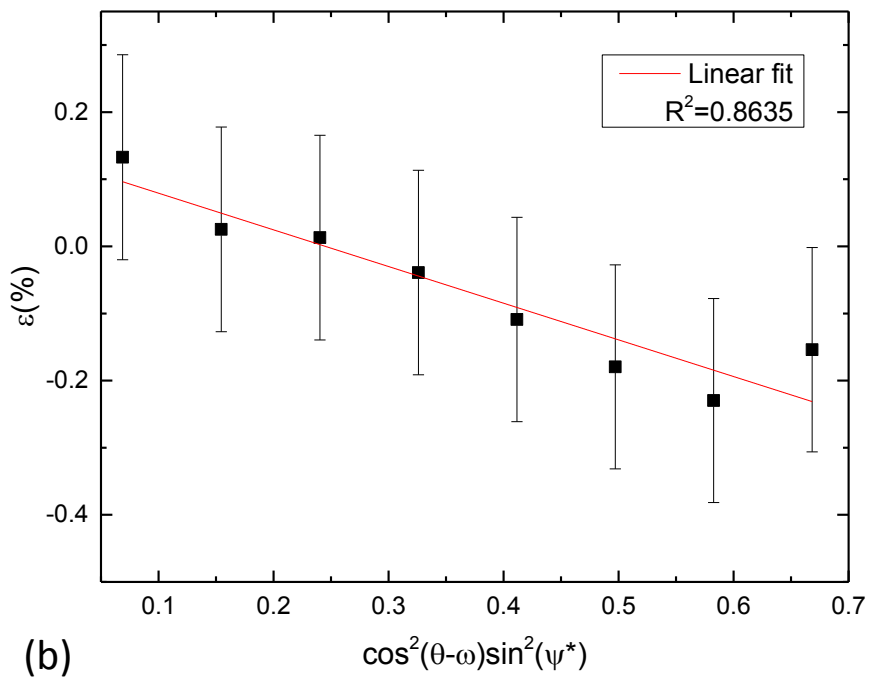


(b)

Figure A.26: (a): Diffractograms of Al-alloyed Re-B sample H at different ψ angles (given on the left hand side of the diffractograms). (b): XRD-measured strain, ϵ , vs. $\cos^2(\theta - \omega) \sin^2(\psi^*)$ plot and linear fit.

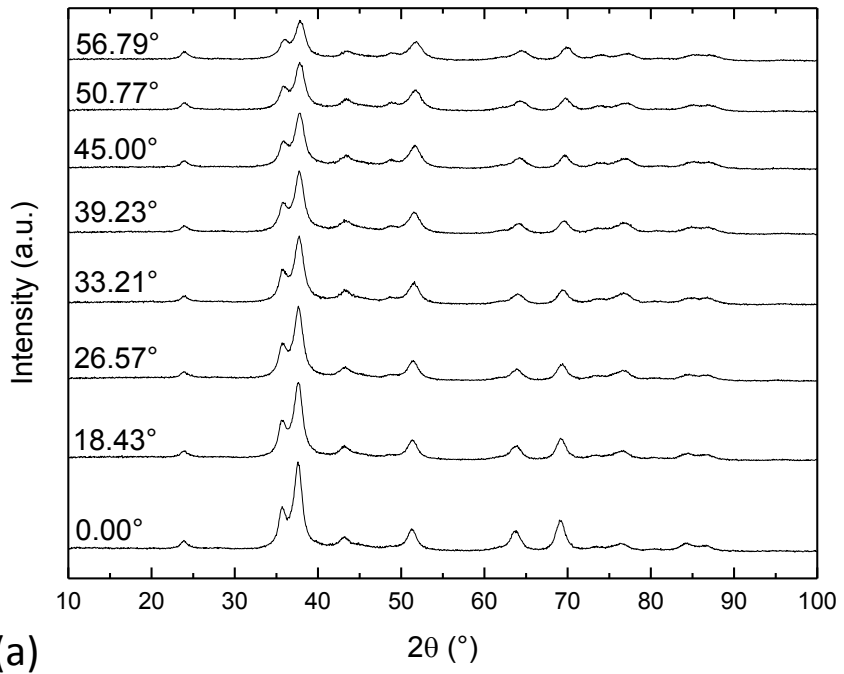


(a)

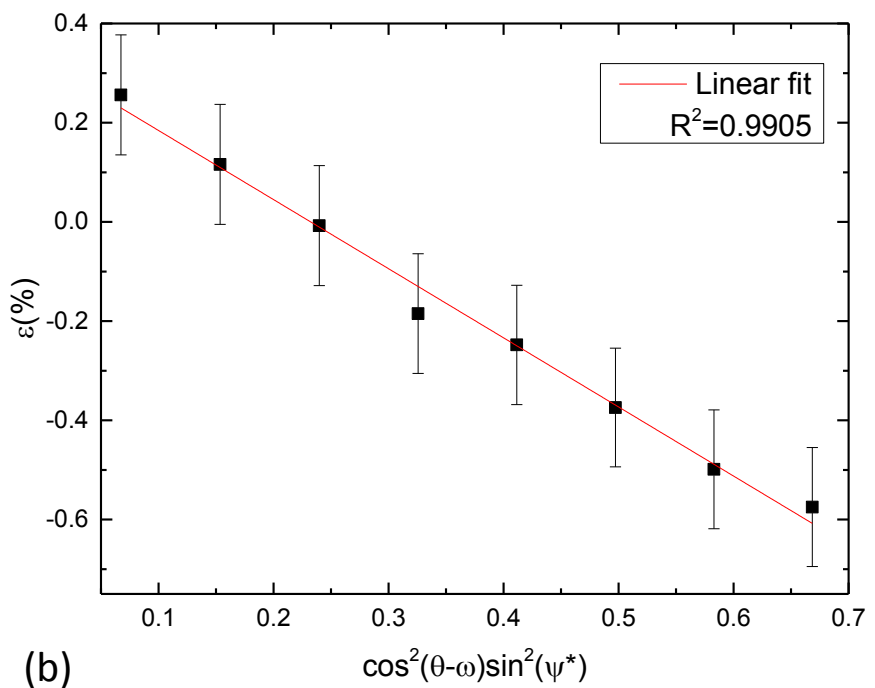


(b)

Figure A.27: (a): Diffractograms of Al-alloyed Re-B sample I at different ψ angles (given on the left hand side of the diffractograms). (b): XRD-measured strain, ϵ , vs. $\cos^2(\theta - \omega)\sin^2(\psi^*)$ plot and linear fit.

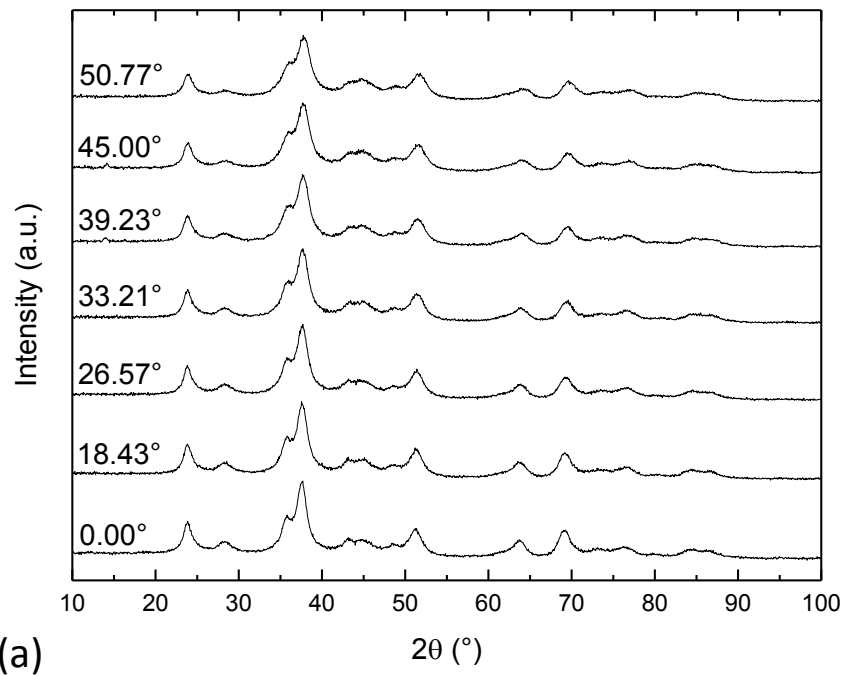


(a)



(b)

Figure A.28: (a): Diffractograms of Ti-alloyed Re-B sample J at different ψ angles (given on the left hand side of the diffractograms). (b): XRD-measured strain, ϵ , vs. $\cos^2(\theta - \omega) \sin^2(\psi^*)$ plot and linear fit.



(a)

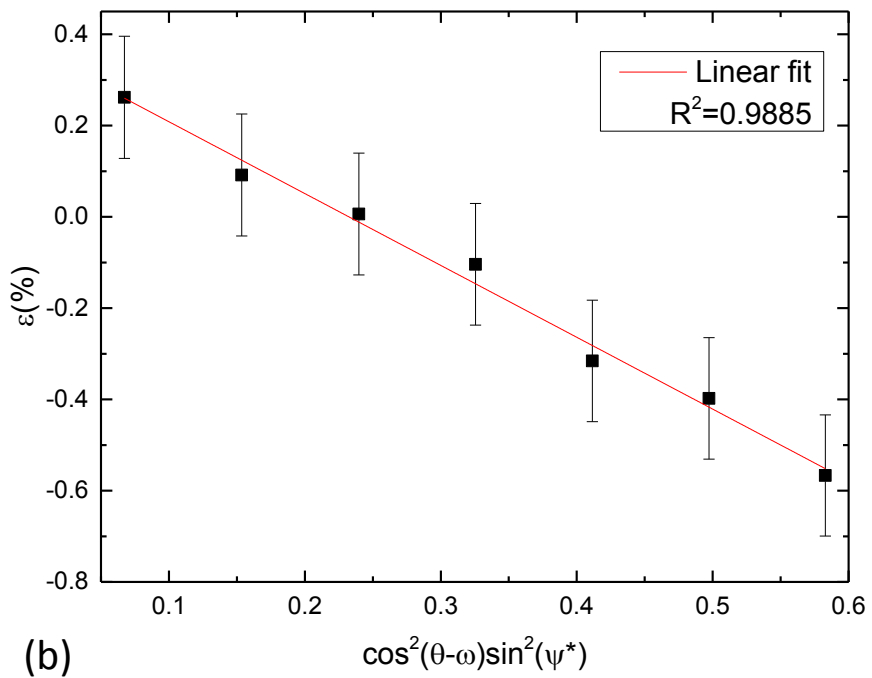
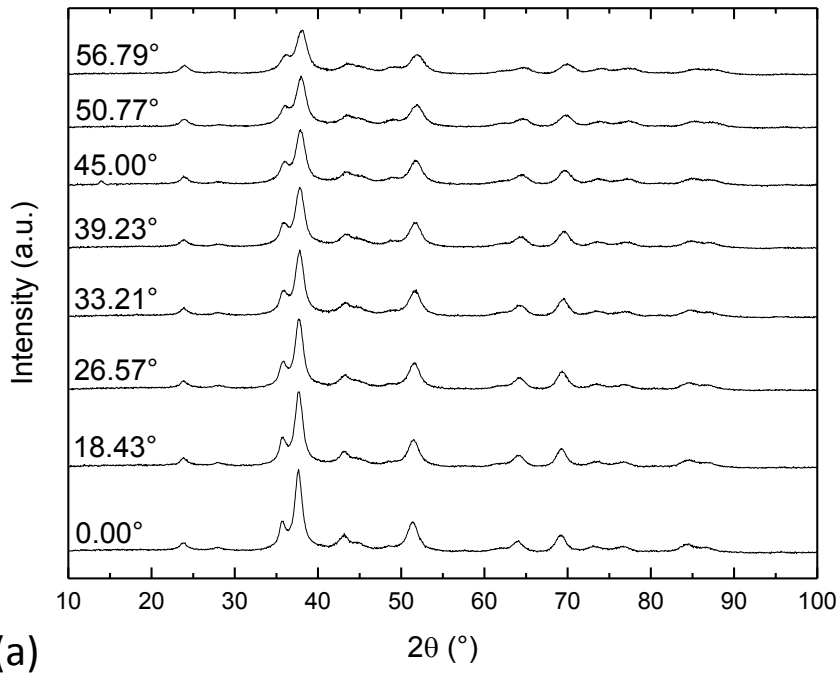
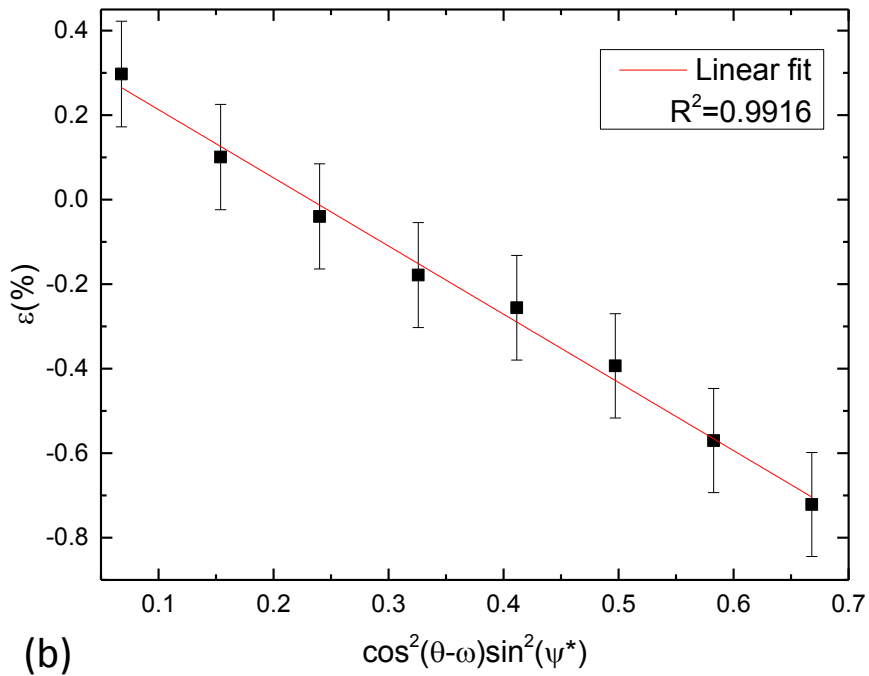


Figure A.29: (a): Diffractograms of Ti-alloyed Re-B sample K at different ψ angles (given on the left hand side of the diffractograms). (b): XRD-measured strain, ϵ , vs. $\cos^2(\theta - \omega) \sin^2(\psi^*)$ plot and linear fit.

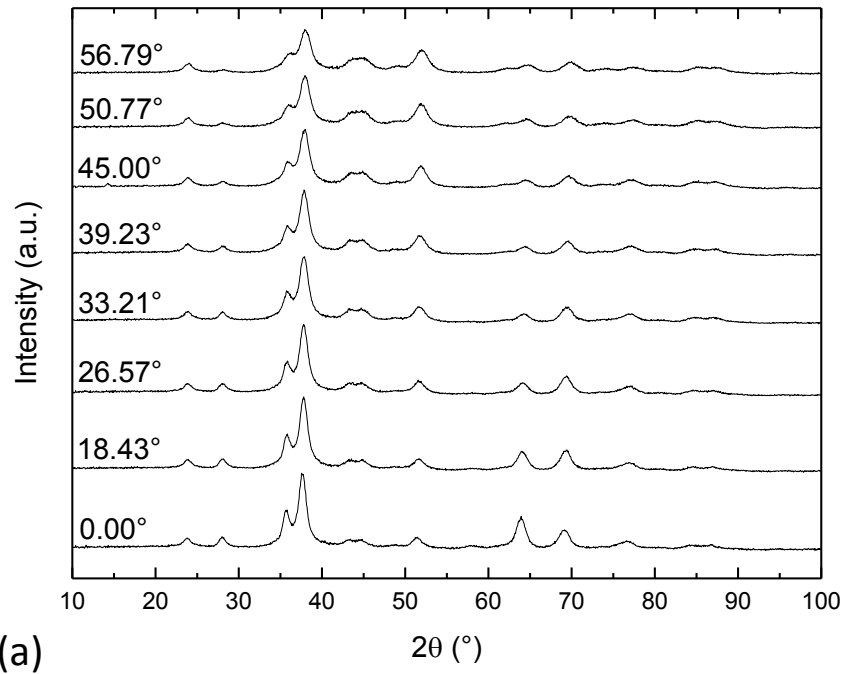


(a)



(b)

Figure A.30: (a): Diffractograms of Ti-alloyed Re-B sample L at different ψ angles (given on the left hand side of the diffractograms). (b): XRD-measured strain, ϵ , vs. $\cos^2(\theta - \omega) \sin^2(\psi^*)$ plot and linear fit.



(a)

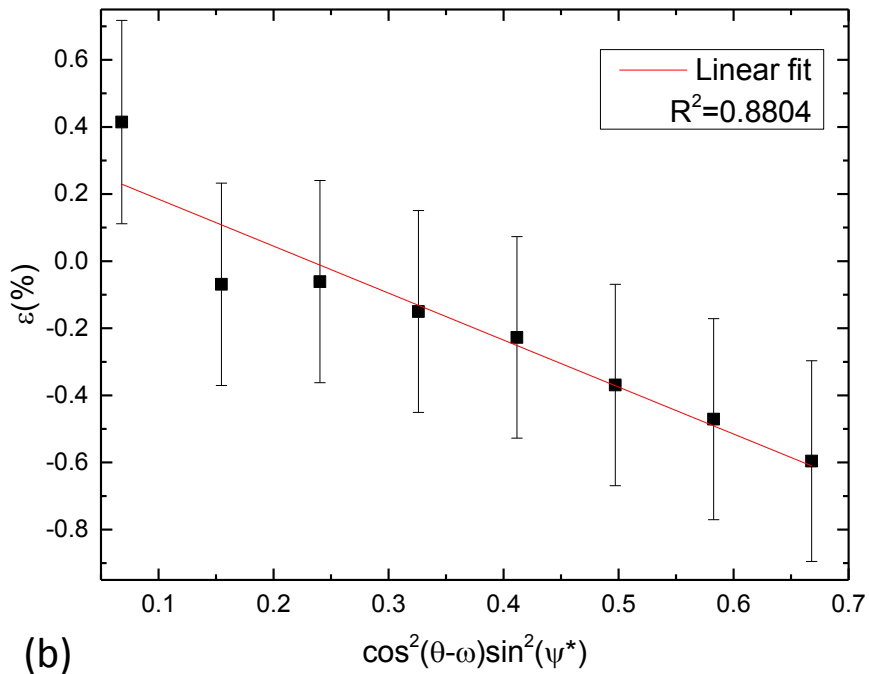


Figure A.31: (a): Diffractograms of Ti-alloyed Re-B sample M at different ψ angles (given on the left hand side of the diffractograms). (b): XRD-measured strain, ϵ , vs. $\cos^2(\theta - \omega) \sin^2(\psi^*)$ plot and linear fit.

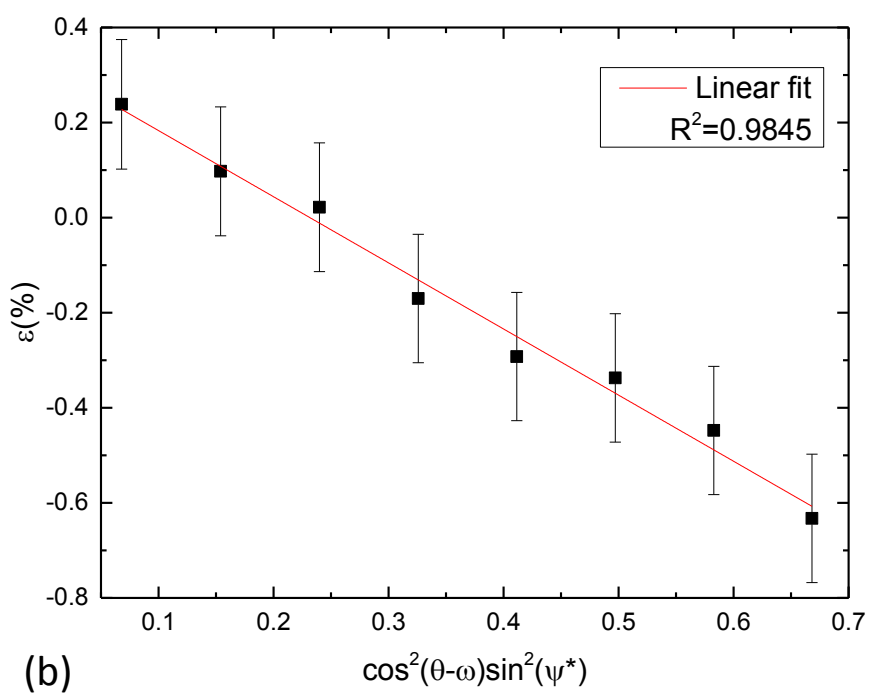
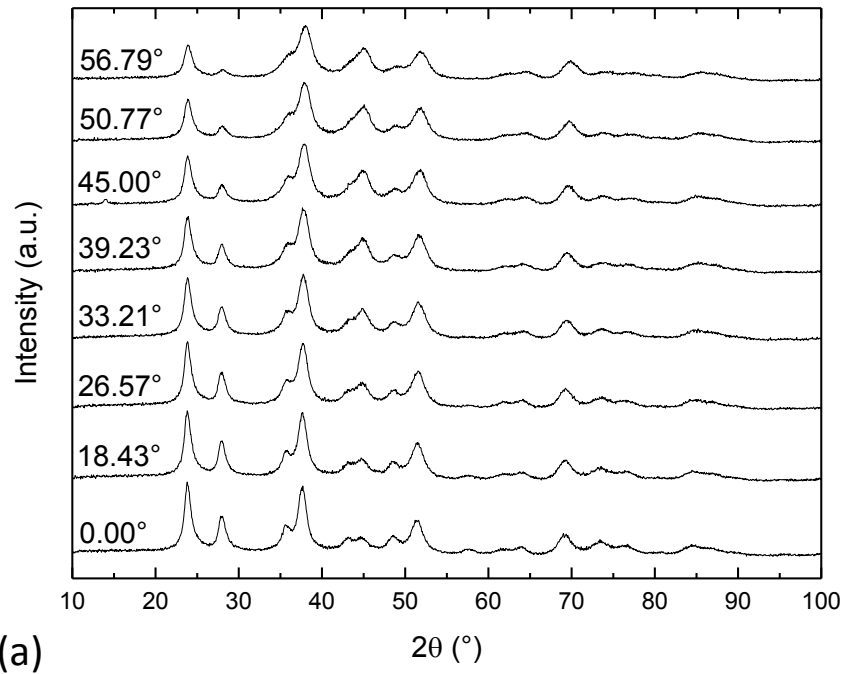


Figure A.32: (a): Diffractograms of Ti-alloyed Re-B sample N at different ψ angles (given on the left hand side of the diffractograms). (b): XRD-measured strain, ϵ , vs. $\cos^2(\theta - \omega) \sin^2(\psi^*)$ plot and linear fit.